

Towards an Understanding of the Correlations in Jet Substructure

Report of BOOST2013, hosted by the University of Arizona, 12th-16th of August 2013.

D. Adams¹, A. Arce², L. Asquith³, M. Backovic⁴, T. Barillari⁵, P. Berta⁶,
D. Bertolini², A. Buckley⁸, J. Butterworth⁹, R. C. Camacho Toro¹⁰, J. Caudron⁹,
Y.-T. Chien¹¹, J. Cogan¹², B. Cooper⁹, D. Curtin¹⁷, C. Debenedetti¹⁸, J. Dolen⁹,
M. Eklund²², S. El Hedri²², S. D. Ellis²², T. Embry²², D. Ferencsek²³, J. Ferrando²⁴,
S. Fleischmann¹⁶, M. Freytsis²⁵, M. Giulini²¹, Z. Han²⁷, D. Hare⁴, P. Harris⁴,
A. Hinzmann⁴, R. Hoing⁴, A. Hornig²², M. Jankowiak⁴, K. Johns²⁸, G. Kasieczka²³,
T. Knight²⁴, G. Kasieczka²⁹, R. Kogler³⁰, W. Lampl⁴, A. J. Larkoski⁴,
C. Lee³¹, R. Leone³¹, P. Loch³¹, D. Lopez Mateos²⁷, H. K. Lou²⁷, M. Low²⁷,
P. Maksimovic³², I. Marchesini³², S. Marzani³², L. Masetti³³, R. McCarthy³²,
S. Menke³², D. W. Miller³⁵, K. Mishra³⁶, B. Nachman³², P. Nef⁴, F. T. O'Grady²⁴,
A. Ovcharova²³, A. Picazio³⁷, C. Pollard³⁸, B. Potter Landua²⁹, C. Potter²⁹,
S. Rappoccio³⁹, J. Rojo⁴⁸, J. Rutherford⁴⁰, G. P. Salam^{10,11}, J. Schabinger²³,
A. Schwartzman⁴, M. D. Schwartz²⁷, B. Shuve⁴³, P. Sinervo⁴⁴, D. Soper⁴⁵,
D. E. Sosa Corral⁴⁵, M. Spannowsky³², E. Strauss³⁴, M. Swiatlowski⁴, J. Thaler³⁴,
C. Thomas³⁴, E. Thompson¹, N. V. Tran³⁶, J. Tseng³⁶, E. Usai³⁶, L. Valery³⁶,
J. Veatch²³, M. Vos²³, W. Waalewijn⁴, and C. Young⁴⁷

¹ Columbia University, Nevis Laboratory, Irvington, NY 10533, USA

² Duke University, Durham, NC 27708, USA

³ Argonne National Laboratory, Lemont, IL 60439, USA

⁴ SLAC National Accelerator Laboratory, Menlo Park, CA 94025, USA

⁵ Deutsches Elektronen-Synchrotron, DESY, D-15738 Zeuthen, Germany

⁶ Cornell University, Ithaca, NY 14853, USA

⁷ Lund University, Lund, SE 22100, Sweden

⁸ University of Edinburgh, EH9 3JZ, UK

⁹ University College London, WC1E 6BT, UK

¹⁰ LPTHE, UPMC Univ. Paris 6 and CNRS UMR 7589, Paris, France

¹¹ CERN, CH-1211 Geneva 23, Switzerland

¹² CAFPE and U. of Granada, Granada, E-18071, Spain

¹³ McGill University, Montreal, Quebec H3A 2T8, Canada

¹⁴ Iowa State University, Ames, Iowa 50011, USA

¹⁵ Rutgers University, Piscataway, NJ 08854, USA

¹⁶ Bergische Universitaet Wuppertal, Wuppertal, D-42097, Germany

¹⁷ YITP, Stony Brook University, Stony Brook, NY 11794-3840, USA

¹⁸ University of Manchester, Manchester, M13 9PL, UK

¹⁹ UNESP - Universidade Estadual Paulista, Sao Paulo, 01140-070, Brazil

²⁰ INFN and University of Naples, IT80216, Italy

²¹ University of Geneva, CH-1211 Geneva 4, Switzerland

²² University of Washington, Seattle, WA 98195, USA

²³ Instituto de Fisica Corpuscular, IFIC/CSIC-UVEG, E-46071 Valencia, Spain

²⁴ University of Glasgow, Glasgow, G12 8QQ, UK

²⁵ Berkeley National Laboratory, University of California, Berkeley, CA 94720, USA

²⁶ Universidad de Buenos Aires, AR-1428, Argentina

²⁷ Harvard University, Cambridge, MA 02138, USA

²⁸ Weizmann Institute, 76100 Rehovot, Israel

²⁹ Universitaet Hamburg, DE-22761, Germany

³⁰ Universitaet Heidelberg, DE-69117, Germany

³¹ University of Arizona, Tucson, AZ 85719, USA

³² IPPP, University of Durham, Durham, DH1 3LE, UK

³³ Universitaet Mainz, DE 55099, Germany

³⁴ MIT, Cambridge, MA 02139, USA

³⁵ University of Chicago, IL 60637, USA

³⁶ Fermi National Accelerator Laboratory, Batavia, IL 60510, USA

³⁷ Indiana University, Bloomington, IN 47405, USA

³⁸ University of California, Davis, CA 95616, USA

³⁹ Johns Hopkins University, Baltimore, MD 21218, USA

⁴⁰ INFN and University of Pisa, Pisa, IT-56127, Italy

⁴¹ Texas A & M University, College Station, TX 77843, USA

⁴² INFN and University of Calabria, Rende, IT-87036, Italy

⁴³ Brown University, Richmond, RI 02912, USA

⁴⁴ Yale University, New Haven, CT 06511, USA

⁴⁵ CEA Saclay, Gif-sur-Yvette, FR-91191, France

⁴⁶ University of Illinois, Chicago, IL 60607, USA

⁴⁷ University of California, Berkeley, CA 94720, USA

Abstract Abstract for BOOST2013 report

Keywords boosted objects · jet substructure · beyond-the-Standard-Model physics searches · Large Hadron Collider

1 Introduction

The characteristic feature of collisions at the LHC is a center-of-mass energy, 7 TeV in 2010 and 2011, of 8 TeV in 2012, and near 14 TeV with the start of the second phase of operation in 2015, that is large compared to even the heaviest of the known particles. Thus these particles (and also previously unknown ones) will often be produced at the LHC with substantial boosts. As a result, when decaying hadronically, these particles will not be observed as multiple jets in the detector, but rather as a single hadronic jet with distinctive internal substructure. This realization has led to a new era of sophistication in our understanding of both standard QCD jets and jets containing the decay of a heavy particle, with an array of new jet observables and detection techniques introduced and studied. To allow the efficient sharing of results from these jet substructure studies a series of BOOST Workshops have been held on a yearly basis: SLAC (2009, [?]), Oxford University (2010, [?]), Princeton University (2011, [?]), IFIC Valencia (2012 [?]), University of Arizona (2013 [?]), and, most recently, University College London (2014 [?]). After each of these meetings Working Groups have functioned during the following year to generate reports highlighting the most interesting new results, including studies of ever maturing details. Previous BOOST reports can be found at [?, ?, ?].

The following report from BOOST 2013 thus views the study and implementation of jet substructure techniques as a fairly mature field. The report attempts to focus on the question of the correlations between the plethora of observables that have been developed and employed, and their dependence on the underlying jet parameters, especially the jet radius R and jet p_T . The report is organized as follows: NEED TO GENERATE AN OUTLINE OF THE REPORT - ESPECIALLY AS I UNDERSTAND IT MYSELF.

2 Monte Carlo Samples and Event Selection

2.1 Quark/gluon and W tagging

Samples were generated at $\sqrt{s} = 8$ TeV for QCD dijets, and for W^+W^- pairs produced in the decay of

a (pseudo) scalar resonance and decaying hadronically. The QCD events were split into subsamples of gg and $q\bar{q}$ events, allowing for tests of discrimination of hadronic W bosons, quarks, and gluons.

Individual gg and $q\bar{q}$ samples were produced at leading order (LO) using MADGRAPH5, while W^+W^- samples were generated using the JHU GENERATOR to allow for separation of longitudinal and transverse polarizations. Both were generated using CTEQ6L1 PDFs[REF]. The samples were produced in exclusive p_T bins of width 100 GeV, with the slicing parameter chosen to be the p_T of any final state parton or W at LO. At the parton-level the p_T bins investigated were 300-400 GeV, 500-600 GeV and 1.0-1.1 TeV. Since no matching was performed, a cut on any parton was equivalent. The samples were then all showered through PYTHIA8 (version 8.176) using the default tune 4C.

2.2 Top tagging

Samples were generated at $\sqrt{s} = 14$ TeV. Standard Model dijet and top pair samples were produced with SHERPA 2.0.0[REF], with matrix elements of up to two extra partons matched to the shower. The top samples included only hadronic decays and were generated in exclusive p_T bins of width 100 GeV, taking as slicing parameter the maximum of the top/anti-top p_T . The QCD samples were generated with a cut on the leading parton-level jet p_T , where parton-level jets are clustered with the anti- k_t algorithm and jet radii of $R = 0.4, 0.8, 1.2$. The matching scale is selected to be $Q_{\text{cut}} = 40, 60, 80$ GeV for the $p_{T\text{min}} = 600, 1000,$ and 1500 GeV bins, respectively.

The analysis again relies on FASTJET 3.0.3 for jet clustering and calculation of jet substructure observables, and an upper and lower p_T cut are applied to each sample to ensure similar p_T spectra in each bin. The bins in leading jet p_T that are investigated for top tagging are 600-700 GeV, 1-1.1 TeV, and 1.5-1.6 TeV. **ED: What jet algorithm is used to define the p_T bins?**

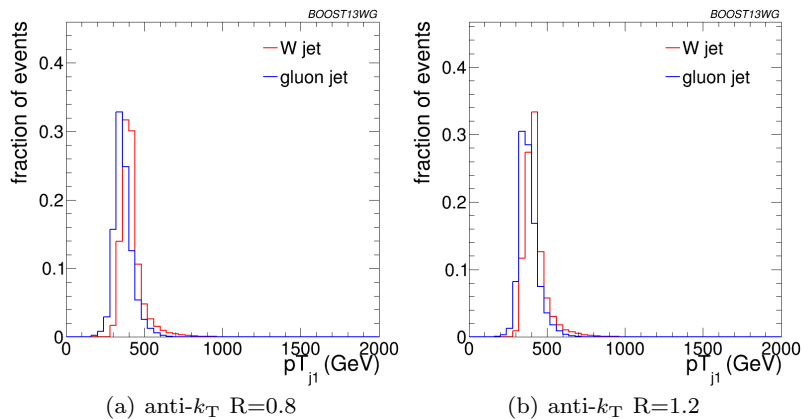


Fig. 1 Comparisons of the leading jet p_T spectrum of the gg background to the WW signal in the p_T 300-400 GeV parton p_T slice using the different anti- k_T jet distance parameters explored in this p_T bin. These distributions are formed prior to the 300-400 GeV leading jet p_T requirement.

3 Jet Algorithms and Substructure Observables

In this section, we define the jet algorithms and observables used in our analysis. Over the course of our study, we considered a larger set of observables, but for the final analysis, we eliminated redundant observables for presentation purposes. In Sections 3.1, 3.2, 3.3 and 3.4 we first describe the various jet algorithms, groomers, taggers and other substructure variables used in these studies, and then in Section 3.5 list which observables are considered in each section of this report, and the exact settings of the parameters used.

3.1 Jet Clustering Algorithms

Jet clustering: Jets were clustered using sequential jet clustering algorithms [REF]. Final state particles i, j are assigned a mutual distance d_{ij} and a distance to the beam, d_{iB} . The particle pair with smallest d_{ij} are recombined and the algorithm repeated until the smallest distance is instead the distance to the beam, d_{iB} , in which case i is set aside and labelled as a jet. The distance metrics are defined as

$$d_{ij} = \min(p_{Ti}^{2\gamma}, p_{Tj}^{2\gamma}) \frac{\Delta R_{ij}^2}{R^2}, \quad (1)$$

$$d_{iB} = p_{Ti}^{2\gamma}, \quad (2)$$

where $\Delta R_{ij}^2 = (\Delta\eta)^2 + (\Delta\phi)^2$. In this analysis, we use the anti- k_t algorithm ($\gamma = -1$), the Cambridge/Aachen (C/A) algorithm ($\gamma = 0$) [REF], and the k_t algorithm ($\gamma = 1$) [REF], each of which has varying sensitivity to soft radiation in defining the jet.

Qjets: We also perform non-deterministic jet clustering [REF]. Instead of always clustering the particle pair

with smallest distance d_{ij} , the pair selected for combination is chosen probabilistically according to a measure

$$P_{ij} \propto e^{-\alpha(d_{ij}-d_{\min})/d_{\min}}, \quad (3)$$

where d_{\min} is the minimum distance for the usual jet clustering algorithm at a particular step. This leads to a different cluster sequence for the jet each time the Qjet algorithm is used, and consequently different substructure properties. The parameter α is called the rigidity and is used to control how sharply peaked the probability distribution is around the usual, deterministic value. The Qjets method uses statistical analysis of the resulting distributions to extract more information from the jet than can be found in the usual cluster sequence. We use $\alpha = 0.1$ and 25 trees per event for all the studies presented here.

3.2 Jet Grooming Algorithms

Pruning: Given a jet, re-cluster the constituents using the C/A algorithm. At each step, proceed with the merger as usual unless both

$$\frac{\min(p_{Ti}, p_{Tj})}{p_{Tij}} < z_{\text{cut}} \quad \text{and} \quad \Delta R_{ij} > \frac{2m_j}{p_{Tj}} R_{\text{cut}}, \quad (4)$$

in which case the merger is vetoed and the softer branch discarded. The default parameters used for pruning [REF] in this study are $z_{\text{cut}} = 0.1$ and $R_{\text{cut}} = 0.5$. One advantage of pruning is that the thresholds used to veto soft, wide-angle radiation scale with the jet kinematics, and so the algorithm is expected to perform comparably over a wide range of momenta.

Trimming: Given a jet, re-cluster the constituents into subjects of radius R_{trim} with the k_t algorithm. Discard all subjects i with

$$p_{Ti} < f_{\text{cut}} p_{TJ}. \quad (5)$$

The default parameters used for trimming in this study are $R_{\text{trim}} = 0.2$ and $f_{\text{cut}} = 0.03$.

Filtering: Given a jet, re-cluster the constituents into subjects of radius R_{filt} with the C/A algorithm. Define the jet to consist of only the hardest N subjects, where N is determined by the final state topology and is typically one more than the number of hard prongs in the resonance decay (to include the leading final-state gluon emission). **ED: Do we actually use filtering as described here anywhere?**

Soft drop: Given a jet, re-cluster all of the constituents using the C/A algorithm. Iteratively undo the last stage of the C/A clustering from j into subjects j_1, j_2 . If

$$\frac{\min(p_{T1}, p_{T2})}{p_{T1} + p_{T2}} < z_{\text{cut}} \left(\frac{\Delta R_{12}}{R} \right)^\beta, \quad (6)$$

discard the softer subject and repeat. Otherwise, take j to be the final soft-drop jet. Soft drop has two input parameters, the angular exponent β and the soft-drop scale z_{cut} , with default value $z_{\text{cut}} = 0.1$. **ED: Soft-drop actually functions as a tagger when $\beta = -1$**

3.3 Jet Tagging Algorithms

Modified Mass Drop Tagger: Given a jet, re-cluster all of the constituents using the C/A algorithm. Iteratively undo the last stage of the C/A clustering from j into subjects j_1, j_2 with $m_{j_1} > m_{j_2}$. If either

$$m_{j_1} > \mu m_j \text{ or } \frac{\min(p_{T1}^2, p_{T2}^2)}{m_j^2} \Delta R_{12}^2 < y_{\text{cut}}, \quad (7)$$

then discard the branch with the smaller transverse mass $m_T = \sqrt{m_i^2 + p_{Ti}^2}$, and re-define j as the branch with the larger transverse mass. Otherwise, the jet is tagged. If de-clustering continues until only one branch remains, the jet is untagged. In this study we use by default $\mu = 1.0$ and $y_{\text{cut}} = 0.1$.

Johns Hopkins Tagger: Re-cluster the jet using the C/A algorithm. The jet is iteratively de-clustered, and at each step the softer prong is discarded if its p_T is less than $\delta_p p_{T\text{jet}}$. This continues until both prongs are harder than the p_T threshold, both prongs are softer than the p_T threshold, or if they are too close ($|\Delta\eta_{ij}| + |\Delta\phi_{ij}| < \delta_R$); the jet is rejected if either of the latter

conditions apply. If both are harder than the p_T threshold, the same procedure is applied to each: this results in 2, 3, or 4 subjects. If there exist 3 or 4 subjects, then the jet is accepted: the top candidate is the sum of the subjects, and W candidate is the pair of subjects closest to the W mass. The output of the tagger is m_t, m_W , and θ_h , a helicity angle defined as the angle, measured in the rest frame of the W candidate, between the top direction and one of the W decay products. The two free input parameters of the Johns Hopkins tagger in this study are δ_p and δ_R , defined above.

HEP Top Tagger: Re-cluster the jet using the C/A algorithm. The jet is iteratively de-clustered, and at each step the softer prong is discarded if $m_1/m_{12} > \mu$ (there is not a significant mass drop). Otherwise, both prongs are kept. This continues until a prong has a mass $m_i < m$, at which point it is added to the list of subjects. Filter the jet using $R_{\text{filt}} = \min(0.3, \Delta R_{ij})$, keeping the five hardest subjects (where ΔR_{ij} is the distance between the two hardest subjects). Select the three subjects whose invariant mass is closest to m_t . The output of the tagger is m_t, m_W , and θ_h , a helicity angle defined as the angle, measured in the rest frame of the W candidate, between the top direction and one of the W decay products. The two free input parameters of the HEP-TopTagger in this study are m and μ , defined above.

Top Tagging with Pruning: For comparison with the other top taggers, we add a W reconstruction step to the trimming algorithm described above. A W candidate is found as follows: if there are two subjects, the highest-mass subject is the W candidate (because the W prongs end up clustered in the same subject); if there are three subjects, the two subjects with the smallest invariant mass comprise the W candidate. In the case of only one subject, no W is reconstructed.

Top Tagging with Trimming: For comparison with the other top taggers, we add a W reconstruction step to the trimming algorithm described above. A W candidate is found as follows: if there are two subjects, the highest-mass subject is the W candidate (because the W prongs end up clustered in the same subject); if there are three subjects, the two subjects with the smallest invariant mass comprise the W candidate. In the case of only one subject, no W is reconstructed.

3.4 Other Jet Substructure Observables

Qjet mass volatility: As described above, Qjet algorithms re-cluster the same jet non-deterministically to obtain a collection of interpretations of the jet. For

each jet interpretation, the pruned jet mass is computed with the default pruning parameters. The mass volatility, Γ_{Qjet} , is defined as

$$\Gamma_{\text{Qjet}} = \frac{\sqrt{\langle m_J^2 \rangle - \langle m_J \rangle^2}}{\langle m_J \rangle}, \quad (8)$$

where averages are computed over the Qjet interpretations.

N -subjettiness: N -subjettiness[REF] quantifies how well the radiation in the jet is aligned along N directions. To compute N -subjettiness, $\tau_N^{(\beta)}$, one must first identify N axes within the jet. Then,

$$\tau_N = \frac{1}{d_0} \sum_i p_{Ti} \min(\Delta R_{1i}^\beta, \dots, \Delta R_{Ni}^\beta), \quad (9)$$

where distances are between particles i in the jet and the axes,

$$d_0 = \sum_i p_{Ti} R^\beta \quad (10)$$

and R is the jet clustering radius. The exponent β is a free parameter. There is also some choice in how the axes used to compute N -subjettiness are determined. The optimal configuration of axes is the one that minimizes N -subjettiness; recently, it was shown that the ‘‘winner-takes-all’’ axes can be easily computed

and have superior performance compared to other minimization techniques[REF]. **ED: Do we use WTA?**

Otherwise why do we mention this?

A more powerful discriminant is often the ratio,

$$\tau_{N,N-1} \equiv \frac{\tau_N}{\tau_{N-1}}. \quad (11)$$

While this is not an infrared-collinear (IRC) safe observable, it is calculable[REF] and can be made IRC safe with a loose lower cut on τ_{N-1} .

Energy correlation functions: The transverse momentum version of the energy correlation functions are defined as[REF]:

$$\text{ECF}(N, \beta) = \sum_{i_1 < i_2 < \dots < i_N \in j} \left(\prod_{a=1}^N p_{Ti_a} \right) \left(\prod_{b=1}^{N-1} \prod_{c=b+1}^N \Delta R_{i_b i_c}^\beta \right) \quad (12)$$

where i is a particle inside the jet. It is preferable to work in terms of dimensionless quantities, particularly the energy correlation function double ratio:

$$C_N^{(\beta)} = \frac{\text{ECF}(N+1, \beta) \text{ECF}(N-1, \beta)}{\text{ECF}(N, \beta)^2}. \quad (13)$$

This observable measures higher-order radiation from leading-order substructure.

3.5 Observables for Each Analysis

Quark/gluon discrimination:

- The ungroomed jet mass, m .
- 1-subjettiness, τ_1^β with $\beta = 1, 2$. The N -subjettiness axes are computed using one-pass k_t axis optimization.
- 1-point energy correlation functions, $C_1^{(\beta)}$ with $\beta = 1, 2$.
- The pruned Qjet mass volatility, Γ_{Qjet} .
- The number of constituents (N_{constits}).

W vs. gluon discrimination:

- The ungroomed, trimmed (m_{trim}), and pruned (m_{prun}) jet masses.
- The mass output from the modified mass drop tagger (m_{mmdt}).
- The soft drop mass with $\beta = -1, 2$ (m_{sd}).
- 2-point energy correlation function ratio $C_2^{\beta=1}$ (we also studied $\beta = 2$ but did not show its results because it showed poor discrimination power).
- N -subjettiness ratio τ_2/τ_1 with $\beta = 1$ ($\tau_{21}^{\beta=1}$) and with axes computed using one-pass k_t axis optimization (we also studied $\beta = 2$ but did not show its results because it showed poor discrimination power).
- The pruned Qjet mass volatility.

Top vs. QCD discrimination:

- The ungroomed jet mass.
- The HEPTopTagger and the Johns Hopkins tagger.
- Trimming and grooming supplemented with W candidate identification.
- N -subjettiness ratios τ_2/τ_1 and τ_3/τ_2 with $\beta = 1$ and the ‘‘winner-takes-all’’ axes.
- 2-point energy correlation function ratios $C_2^{\beta=1}$ and $C_3^{\beta=1}$.
- The pruned Qjet mass volatility, Γ_{Qjet} .

4 Multivariate Analysis Techniques

β Multivariate techniques are used to combine variables into an optimal discriminant. In all cases variables are combined using a boosted decision tree (BDT) as implemented in the TMVA package [?]. We use the BDT implementation including gradient boost. An example of the BDT settings are as follows:

- NTrees=1000
- BoostType=Grad
- Shrinkage=0.1
- UseBaggedGrad=F
- nCuts=10000
- MaxDepth=3

277 – UseYesNoLeaf=F
 278 – nEventsMin=200

279 Exact parameter values are chosen to best reduce the
 280 effect of overtraining.

281 5 Quark-Gluon Discrimination

282 In this section, we examine the differences between quark-³³²
 283 and gluon-initiated jets in terms of substructure vari-³³³
 284 ables, and to determine to what extent these variables³³⁴
 285 are correlated. Along the way, we provide some theoret-
 286 ical understanding of these observables and their per-³³⁵
 287 formance. The motivation for these studies comes not
 288 only from the desire to “tag” a jet as originating from³³⁶
 289 a quark or gluon, but also to improve our understand-³³⁷
 290 ing of the quark and gluon components of the QCD³³⁸
 291 backgrounds relative to boosted resonances. While re-³³⁹
 292 cent studies have suggested that quark/gluon tagging³⁴⁰
 293 efficiencies depend highly on the Monte Carlo generator³⁴¹
 294 used, we are more interested in understanding the scal-³⁴²
 295 ing performance with p_T and R , and the correlations³⁴³
 296 between observables, which are expected to be treated³⁴⁴
 297 consistently within a single shower scheme. ³⁴⁵

298 5.1 Methodology

299 These studies use the qq and gg MC samples, described³⁵⁰
 300 previously in Section 2. The showered events were clus-³⁵¹
 301 tered with FASTJET 3.03[REF]using the anti- k_T algo-³⁵²
 302 rithm[REF]with jet radii of $R = 0.4, 0.8, 1.2$. In both³⁵³
 303 signal and background, an upper and lower cut on the³⁵⁴
 304 leading jet p_T is applied after showering/clustering, to³⁵⁵
 305 ensure similar p_T spectra for signal and background in³⁵⁶
 306 each p_T bin. The bins in leading jet p_T that are inves-³⁵⁷
 307 tigated in the W-tagging and q/g tagging studies are³⁵⁸
 308 300-400 GeV, 500-600 GeV, 1.0-1.1 TeV. The distribu-³⁵⁹
 309 tion of the leading jet p_T for the gg and WW samples³⁶⁰
 310 in the 300-400 GeV parton p_T slice prior to the require-³⁶¹
 311 ment on the leading jet p_T is shown in Figure 1, for the³⁶²
 312 $R=0.8$ and $R=1.2$ anti- k_T jet radii considered in this³⁶³
 313 p_T slice. Figures 2 and 3 show the equivalent leading³⁶⁴
 314 jet p_T distributions for the jet radii considered in the³⁶⁵
 315 500-600 GeV and 1.0 - 1.1 TeV slices respectively. Var-³⁶⁶
 316 ious jet grooming approaches are applied to the jets, as³⁶⁷
 317 described in Section 3.4. Only leading and subleading³⁶⁸
 318 jets in each sample are used. ³⁶⁹

319 Figure 4 shows a comparison of the p_T and η dis-³⁷⁰
 320 tributions of the quark and gluon samples with $p_T =$ ³⁷¹
 321 500 – 600 GeV. The differences in the p_T distributions³⁷²
 322 can be attributed to different out-of-cone radiation pat-³⁷³
 323 terns for quark and gluons; these differences become³⁷⁴

324 smaller as the R parameter is increased. The different
 325 η distributions are related to the different parton distri-
 326 bution functions initiating qq and gg production. The
 327 qualitative features of the η distributions do not change
 328 as the R parameter is changed. As the p_T increases, the
 329 η distributions peak more strongly near zero, as the
 330 probability peaks for processes initiated by partons of
 331 comparable energy. In our analysis, we make a narrow
 332 window cut of 100 GeV in p_T after showering, and so
 333 the effects of the different q/g p_T spectra on our anal-
 334 ysis is suppressed. (**ED: check**)

5.2 Single Variable Discrimination

Figure 5 shows the mass of jets in the quark and gluon
 samples when using different groomers. Jets built with
 the anti- k_T algorithm with $R=0.8$ and with $p_T = 500 -$
 650 GeV are used (**BS:Check p_T bins in this sec-**
tion!). Qualitatively, the application of grooming shifts
 the mass distributions towards lower values as expected.
 No clear gain in discrimination can be seen, and for
 certain grooming parameters, such as the use of soft
 drop with $\beta = -1$ a clear loss in discrimination power
 is observed; this is because the soft-drop condition for
 $\beta = -1$ discards collinear radiation, and the differences
 between quarks and gluons are manifest in the collinear
 structure (spin, splitting functions, etc.).

The performance of different substructure variables
 is explored in Figure 6. Among those considered, n_{constits}
 provides the highest separation power, followed by $C_1^{\beta=0}$
 and $C_1^{\beta=1}$ as was also found by the CMS and ATLAS
 Collaborations[REF].

To more quantitatively study the power of each ob-
 servable as a discriminator for quark/gluon tagging, Re-
 ceiver Operating Characteristic (ROC) curves are built
 by scanning each distribution and plotting the back-
 ground efficiency (to select gluon jets) vs. the signal
 efficiency (to select quark jets). Figure 7 shows these
 ROC curves for all of the variables shown in Figure 6
 and the ungroomed mass, representing the best per-
 forming mass variable, for jets of $p_T = 300 - 400$ GeV.
 In addition, we show the ROC curve for the tagger built
 from a BDT combining all the variables. The details of
 how the BDT is constructed are explained in Section 4.
 Clearly, n_{constits} is the best performing variable for all
 R s, even though $C_1^{\beta=0}$ is close, particularly for $R=0.8$.
 Most other variables have similar performance, except
 the Q-jet volatility, which shows significantly worse dis-
 crimination (this may be due to our choice of rigid-
 ity $\alpha = 0.1$, while other studies suggest that a smaller
 value, such as $\alpha = 0.01$, produces better results). The
 combination of all variables shows somewhat better dis-
 crimination.

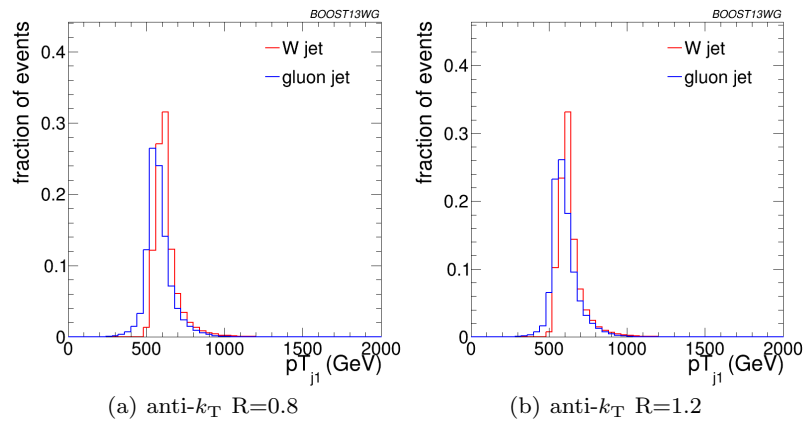


Fig. 2 Comparisons of the leading jet p_T spectrum of the gg background to the WW signal in the p_T 500-600 GeV parton p_T slice using the different anti- k_T jet distance parameters explored in this p_T bin. These distributions are formed prior to the 500-600 GeV leading jet p_T requirement.

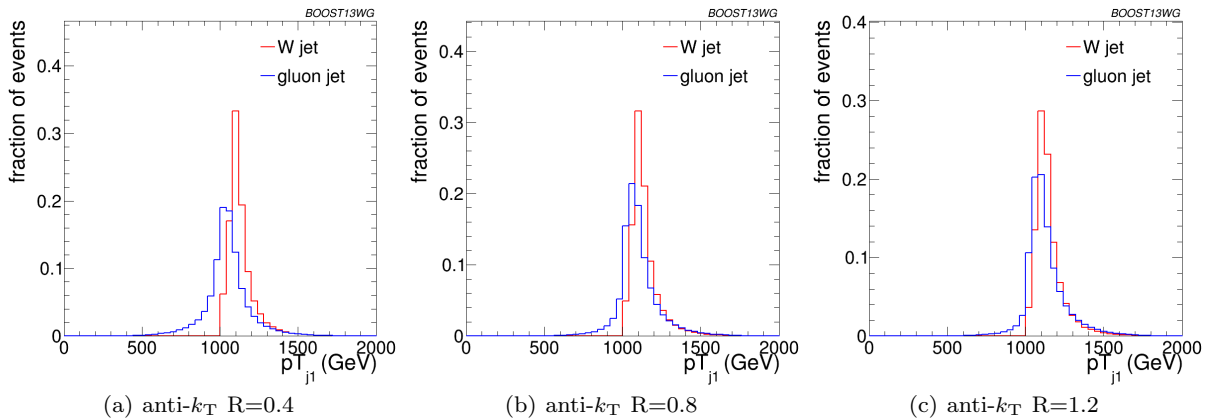


Fig. 3 Comparisons of the leading jet p_T spectrum of the gg background to the WW signal in the p_T 1.0-1.1 TeV parton p_T slice using the different anti- k_T jet distance parameters explored in this p_T bin. These distributions are formed prior to the 500-600 GeV leading jet p_T requirement.

375 We now examine how performance of masses and 392
 376 substructure observables changes with p_T and R . For 393
 377 jet masses, few variations are observed as the radius pa-394
 378 rameter of the jet reconstruction is increased in the two 395
 379 highest p_T bins; this is because the radiation is more 396
 380 collimated and the dependence on R is consequently 397
 381 smaller. However, for the 300 – 400 GeV bin, the use of 398
 382 small- R jets produces a shift in the mass distributions 399
 383 towards lower values, so that large- R jet masses are 400
 384 more stable with p_T and small- R jet masses are smaller 401
 385 at low- p_T as expected from the spatial constraints im- 402
 386 posed by the R parameter. These statements are ex- 403
 387 plored more quantitatively later in this section. (BS: 404
 388 **Do we have plots for this?**) 405

389 The evolution of some of the substructure variable 406
 390 distributions with p_T and R is less trivial than for the 407
 391 jet masses. In particular, changing the R parameter at 408

high p_T changes significantly the C_a^β for $\beta > 0$ and
 the n_{constits} distributions, while leaving all other distri-
 butions qualitatively unchanged. This is illustrated in
 Figure 8 for $\beta = 0$ and $\beta = 1$ using $a = 1$ in both cases
 for jets with $p_T = 1 - 1.2$ TeV.

The shift towards lower values with changing R is
 evident for the $C_1^{\beta=1}$ distributions, while the stability of
 $C_1^{\beta=0}$ can also be observed. These features are present
 in all p_T bins studied, but are even more pronounced for
 lower p_T bins. The shape of the Q-jet volatility distri-
 bution shows some non-trivial shape that deserves some
 explanation. Two peaks are observed, one at low volatili-
 ty values and one at mid-volatility. These peaks are
 generated by two somewhat distinct populations. The
 high volatility peak arises from jets that get their mass
 primarily from soft (and sometimes wide-angle) emis-
 sions. The removal of some of the constituents when

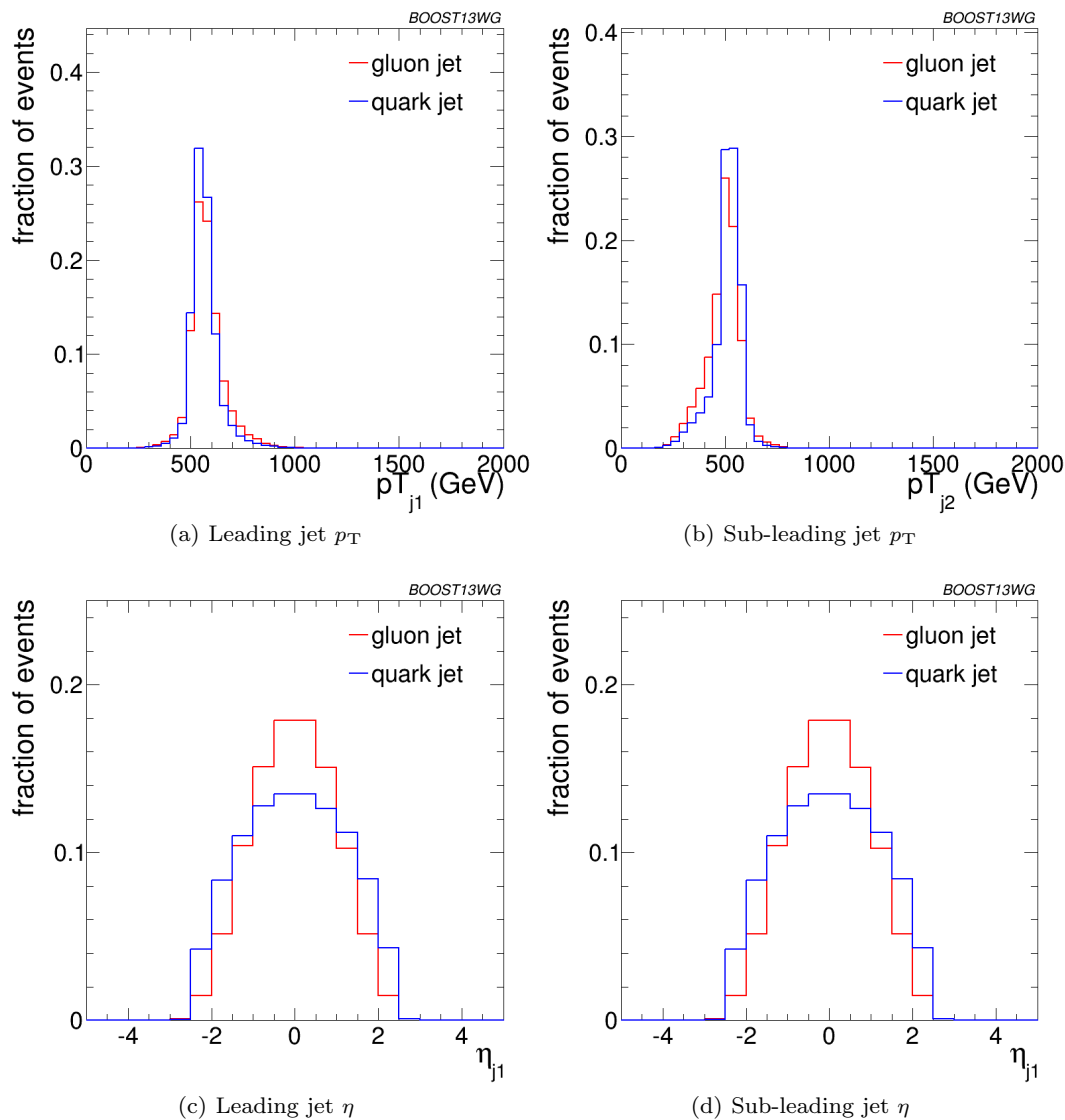


Fig. 4 Comparisons of quark and gluon p_T and η distributions in the sample used for the jets of $p_T = 500 - 600$ GeV bin using the anti- k_T $R=0.8$ algorithm.

409 building Q-jets thus changes the mass significantly, in-423
 410 creasing the volatility. The lower volatility peak cor-424
 411 responds to jets for which mass is generated by a hard
 412 emission, which makes the fraction of Q-jets that change
 413 the mass significantly to be smaller. Since the proba-425
 414 bility of a hard emission is proportional to the colour
 415 charge (squared), the volatility peak is higher for gluon426
 416 jets by about the colour factor C_A/C_F . 427

417 In summary, the overall discriminating power be-429
 418 tween quarks and gluons decreases with increasing R 430
 419 due to the reduction in the amount of out-of-cone radi-431
 420 ation differences and and increased contamination from432
 421 the underlying event (**BS: is this ok?**). The broad per-433
 422 formance features discussed for this p_T bin also apply434

to the higher p_T bins. These is further quantified in the next section.

5.3 Combined Performance and Correlations

The quark/gluon tagging performance can be further improved over cuts on single observables by combining multiple observables in a BDT; due to the challenging nature of q/g -tagging, any improvement in performance with multivariable techniques could be critical for certain analyses, and the improvement could be more substantial in data than the marginal benefit found in MC and shown in Fig. 7. Furthermore, insight can be gained into the features allowing for quark/gluon

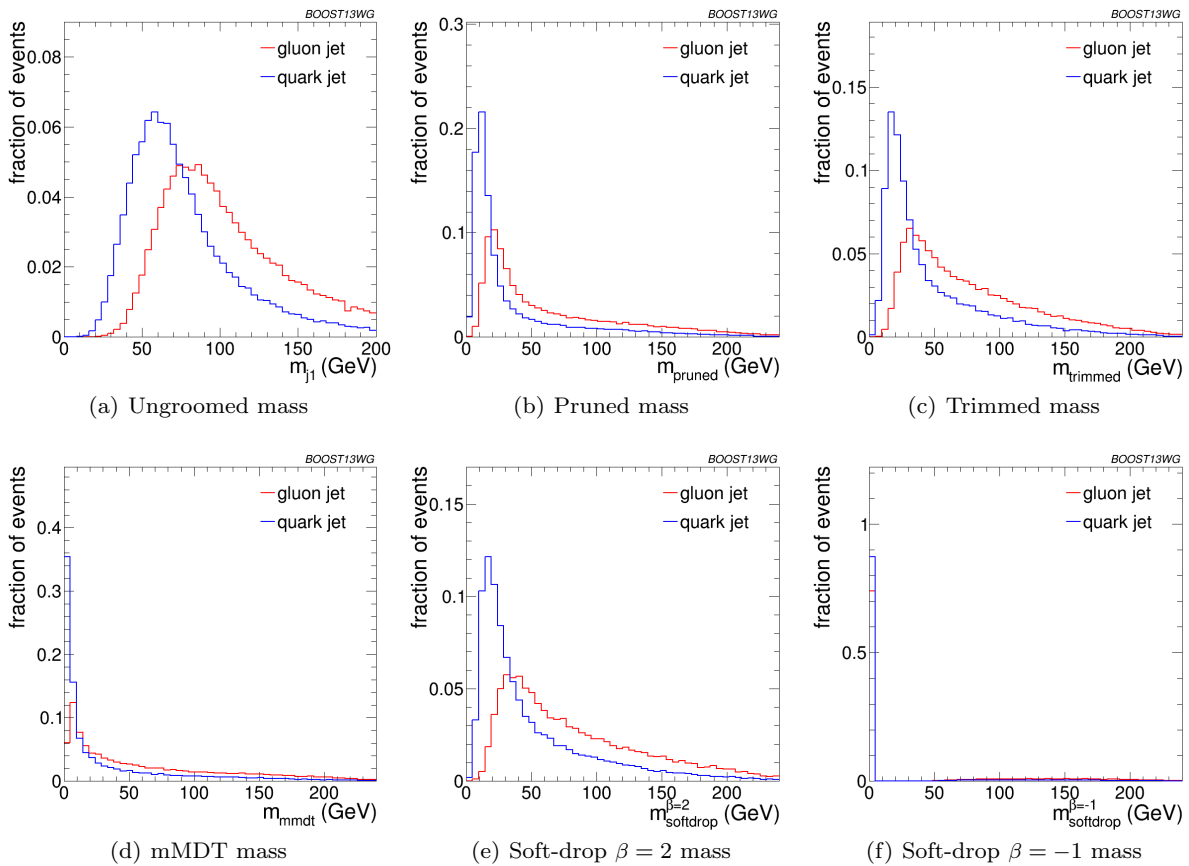


Fig. 5 Comparisons of ungroomed and groomed quark and gluon mass distributions for leading jets in the $p_T = 500 - 650$ GeV bin using the anti- k_T $R=0.8$ algorithm.

discrimination if the origin of the improvement is understood. To quantitatively study this improvement, we build quark/gluon taggers from every pair-wise combination of variables studied in the previous section for comparison with the all-variable combination.

In order to quantitatively study the value of each variable for quark/gluon tagging, we study the gluon rejection, defined as $1/\epsilon_{\text{gluon}}$, at a fixed quark selection efficiency of 50% using jets with $p_T = 1 - 1.2$ TeV for different R parameters. Figure 9 shows the gluon rejection for each pair-wise combination. The pair-wise gluon rejection at 50% quark efficiency can be compared to the single-variable values shown along the diagonal. The gluon rejection for the BDT all-variable combination is also shown on the bottom right of each plot. As already observed in the previous section, n_{constits} is the most powerful single variable and $C_1^{(\beta=0)}$ follows closely. However, the gains are largely correlated; the combined performance of n_{constits} and $C_1^{(\beta=0)}$ is generally poorer than combinations of n_{constits} with other jet substructure observables, such as τ_1 . Interestingly, in spite of the high correlation between n_{constits} and $C_1^{(\beta=0)}$, the two-

variable combinations of n_{constits} generally fare worse than two-variable combinations with $C_1^{(\beta=0)}$. In particular, the combinations of $\tau_1^{\beta=1}$ or $C_1^{(\beta=1)}$ with n_{constits} are capable of getting very close to the rejection achievable through the use of all variables for $R = 0.4$ and $R = 0.8$.

Tagger performance is generally better at small R . The overall loss in performance with increasing R can be seen in most single variables we study; this is expected, since more of the parton radiation is captured in the jet and more contamination from underlying event occurs, suppressing the differences between q/g jets. The principal exceptions are $C_1^{(\beta=0)}$ and the Q-jet mass volatility, which are both quite resilient to increasing R . For $C_1^{(\beta=0)}$, this is due to the fact that the exponent on ΔR is zero, and so soft radiation at the periphery of the jet does not substantially change the distribution; as a result, the performance is largely independent of R . Similarly, the soft radiation distant from the jet centre will be vetoed during pruning regardless of the cluster sequence, and so the R -dependence of I_{Qjet} is not significant. **(BS: Check my logic?)** Their combination,

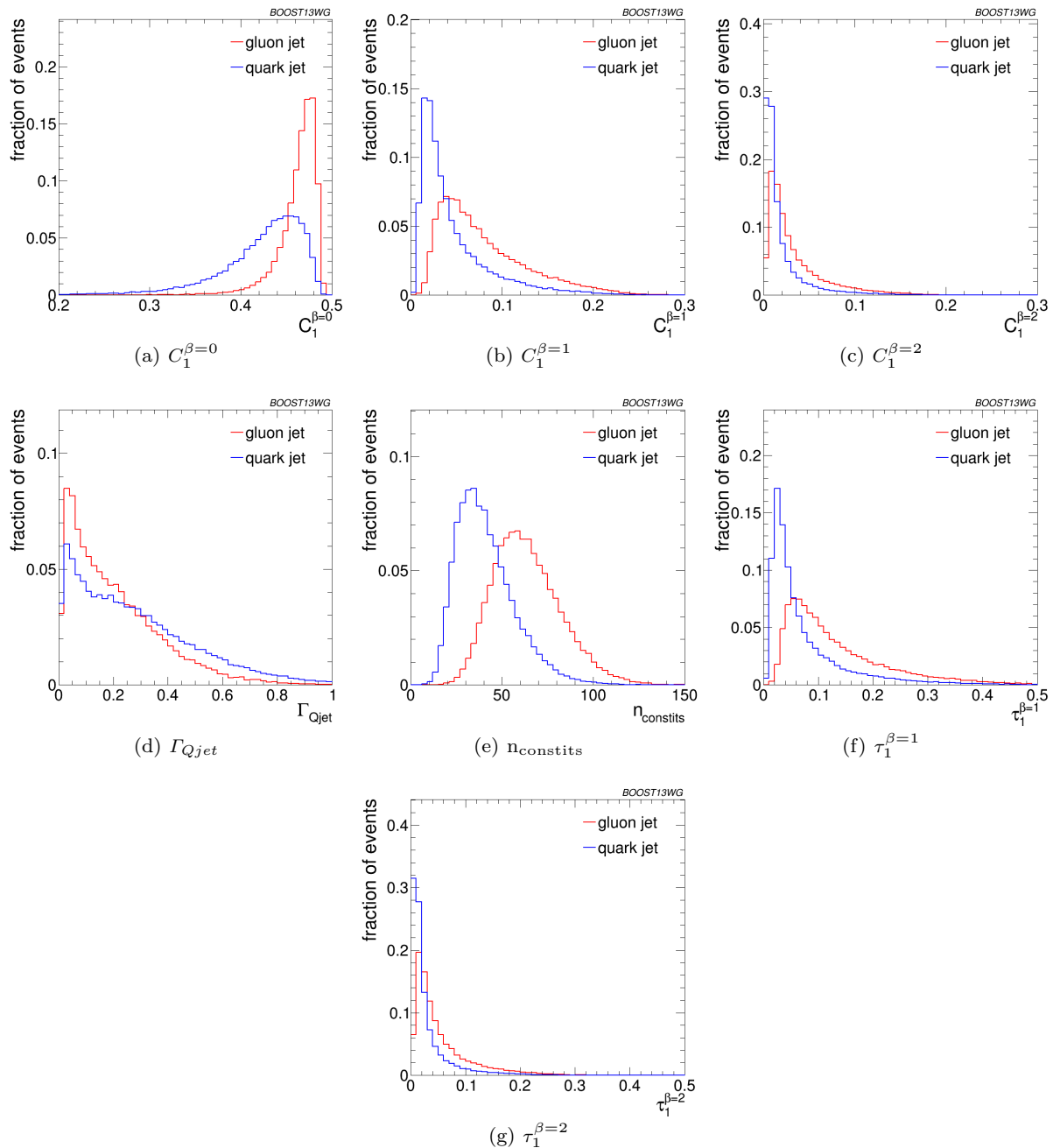


Fig. 6 Comparisons of quark and gluon distributions of different substructure variables for leading jets in the $p_T = 500 - 650$ GeV bin using the anti- k_T $R=0.8$ algorithm.

479 however, does perform slightly worse at larger R . (**BS**₄₈₇
 480 **I don't understand this, but it is a $\sim 10\%$ ef**₄₈₈
 481 **fect, so maybe not too significant?**). By contrast,₄₈₉
 482 $\tau_1^{(\beta=2)}$ and $C_1^{(\beta=2)}$ are particularly sensitive to increas₄₉₀
 483 ing R since, for $\beta = 2$, large-angle emissions are given₄₉₁
 484 a larger weight.

485 These observations are qualitatively similar across₄₉₄
 486 all ranges of p_T . Quantitatively, however, there is a loss₄₉₅

of rejection power for the taggers made of a combi-
 nation of variables as the p_T decreases. This can be
 observed in Fig. 10 for anti- k_T $R=0.4$ jets of different
 p_T s. Clearly, most single variables retain their gluon re-
 jection potential at lower p_T . However, when combined
 with other variables, the highest performing pairwise
 combinations lose ground with respect to other pair-
 wise combinations. This is also reflected in the rejection
 of the tagger that uses a combination of all variables,

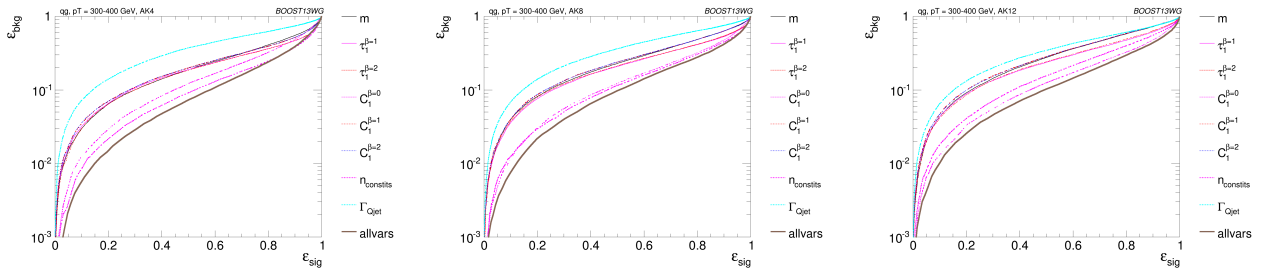


Fig. 7 The ROC curve for all single variables considered for quark-gluon discrimination in the p_T 500 GeV bin using the anti- k_T $R=0.8$ algorithm.

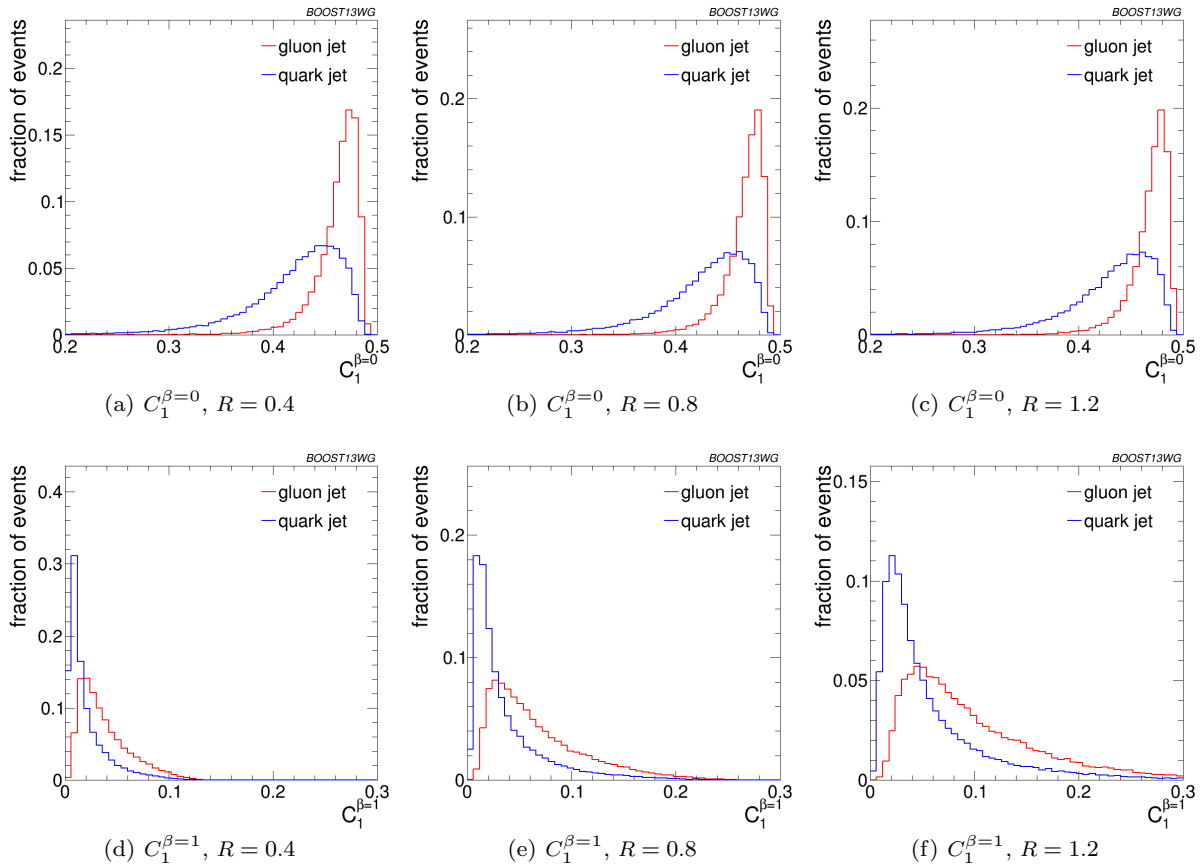


Fig. 8 Comparisons of quark and gluon distributions of $C_1^{\beta=0}$ (top) and $C_1^{\beta=1}$ (bottom) for leading jets in the $p_T = 1 - 1.2$ TeV bin using the anti- k_T algorithm with $R = 0.4, 0.8$ and 1.2 .

496 which is lower at lower p_T s. [do we understand this?]
 497 (BS: This is a bit of a guess, but could it be that
 498 there is typically less radiation for low p_T , and so
 499 you're more sensitive to fluctuations; since you
 500 have less access to information, combinations of
 501 observables perform less well than at high p_T .)

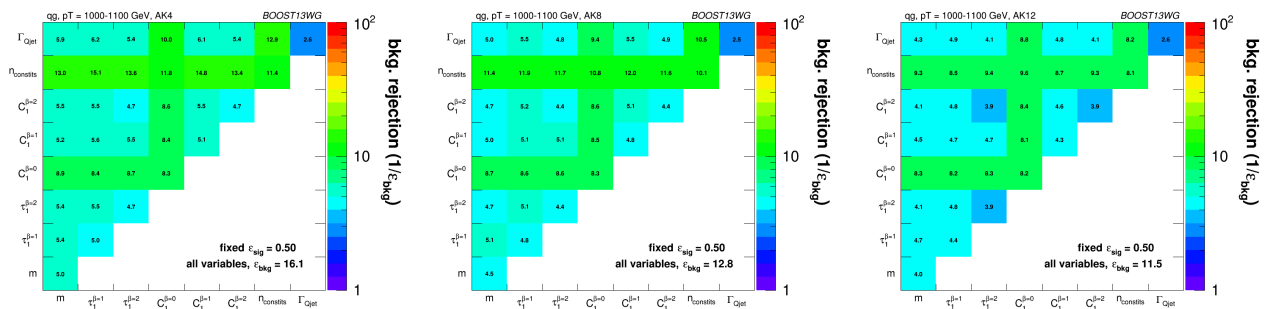


Fig. 9 Gluon rejection defined as $1/\epsilon_{\text{gluon}}$ when using each 2-variable combination as a tagger with 50% acceptance for quark jets. Results are shown for jets with $p_T = 1 - 1.2$ TeV and for (left) $R = 0.4$; (centre) $R = 0.8$; (right) $R = 1.2$. The rejection obtained with a tagger that uses all variables is also shown in the plots.

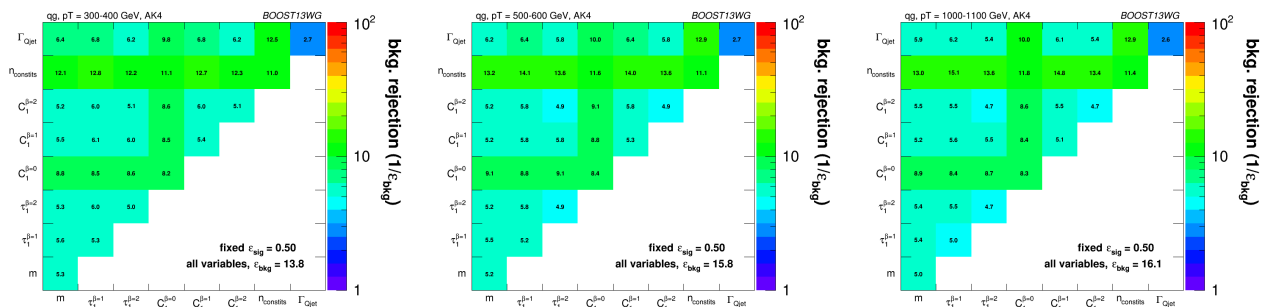


Fig. 10 Gluon rejection defined as $1/\epsilon_{\text{gluon}}$ when using each 2-variable combination as a tagger with 50% acceptance for quark jets. Results are shown for $R=0.4$ jets with $p_T = 300 - 400$ GeV, $p_T = 500 - 600$ GeV and $p_T = 1 - 1.2$ TeV. The rejection obtained with a tagger that uses all variables is also shown in the plots.

6 Boosted W -Tagging

In this section, we study the discrimination of a boosted hadronically decaying W signal against a gluon background, comparing the performance of various groomed jet masses, substructure variables, and BDT combinations of groomed mass and substructure. We produce ROC curves that elucidate the performance of the various groomed mass and substructure variables. A range of different distance parameters R for the anti- k_T jet algorithm are explored, as well as a variety of kinematic regimes (lead jet p_T 300-400 GeV, 500-600 GeV, 1.0-1.1 TeV). This allows us to determine the performance of observables as a function of jet radius and jet boost, and to see where different approaches may break down. The groomed mass and substructure variables are then combined in a BDT as described in Section 4, and the performance of the resulting BDT discriminant explored through ROC curves to understand the degrees to which variables are correlated, and how this changes with jet boost and jet radius.

6.1 Methodology

These studies use the WW samples as signal and the dijet gg samples to model the QCD background, as described previously in Section 2. Whilst only gluonic backgrounds are explored here, the conclusions as to the dependence of the performance and correlations on the jet boost and radius have been verified to hold also for qq backgrounds. **ED: To be checked!**

In each of the three p_T slices considered jets are reconstructed using the anti- k_T algorithm with distance parameter $R=0.4, 0.8$ and 1.2 , as described in Section 2. They then have various grooming approaches applied as described in Section 3.5. **(ED: Probably better if some of the information from Sections 2 and 3.5 is brought into this section to avoid this back-referencing.)**

6.2 Single Variable Performance

In this section we will explore the performance of the various groomed jet mass and substructure variables in terms of discriminating signal and background, and how

542 this performance changes depending on the kinematic595
543 bin and jet radius considered. 596

544 Figure 11 compares the signal and background597
545 in terms of the different groomed masses explored for598
546 the anti- k_T $R=0.8$ algorithm in the p_T 500-600 bin. One599
547 can clearly see that in terms of separating signal and600
548 background the groomed masses will be significantly601
549 more performant than the ungroomed anti- k_T $R=0.8$ 602
550 mass. Figure 12 compares signal and background in the603
551 different substructure variables explored for the same604
552 jet radius and kinematic bin. 605

553 Figures 13, 14 and 15 show the single variable ROC606
554 curves compared to the ROC curve for a BDT combi-607
555 nation of all the variables (labelled “allvars”), for each608
556 of the anti- k_T distance parameters considered in each609
557 of the kinematic bins. One can see that, in all cases,610
558 the “allvars” option is considerably better performant611
559 than any of the individual single variables considered,612
560 indicating that there is considerable complementarity613
561 between the variables, and this will be explored further614
562 in the next section. 615

563 Although the ROC curves give all the relevant in-616
564 formation, it is hard to compare performance quanti-617
565 tatively. In Figures 16, 17 and 18 are shown matrices618
566 which give the background rejection for a signal effi-619
567 ciency of 70% when two variables (that on the x-axis620
568 and that on the y-axis) are combined in a BDT. These621
569 are shown separately for each p_T bin and jet radius
570 considered. The diagonal of these plots correspond to
571 the background rejections for a single variable BDT,622
572 and can thus be examined to get a quantitative mea-
573 sure of the individual single variable performance, and623
574 to study how this changes with jet radius and momenta.624

575 One can see that in general the most performant625
576 single variables are the groomed masses. However, in626
577 certain kinematic bins and for certain jet radii, $C_2^{\beta=1}$ 627
578 has a background rejection that is comparable to or628
579 better than the groomed masses. 629

580 By comparing Figures 16(a), 17(a) and 18(b), we530
581 can see how the background rejection performance evolves531
582 as we increase momenta whilst keeping the jet radius532
583 fixed to $R=0.8$. Similarly, by comparing Figures 16(b), 17(b)
584 and 18(c) we can see how performance evolves with p_T 534
585 for $R=1.2$. For both $R=0.8$ and $R=1.2$ the background535
586 rejection power of the groomed masses increases with536
587 increasing p_T , with a factor 1.5-2.5 increase in rejec-537
588 tion in going from the 300-400 GeV to 1.0-1.1 TeV bins.538
589 **ED: Add some of the 1-D plots comparing sig-539**
590 **nal and bkgd in the different masses and pT bins540**
591 **here?** However, the $C_2^{\beta=1}$, Γ_{Qjet} and $\tau_{21}^{\beta=1}$ substructure541
592 variables behave somewhat differently. The background542
593 rejection power of the Γ_{Qjet} and $\tau_{21}^{\beta=1}$ variables both543
594 decrease with increasing p_T , by up to a factor two544

in going from the 300-400 GeV to 1.0-1.1 TeV bins.
Conversely the rejection power of $C_2^{\beta=1}$ dramatically
increases with increasing p_T for $R=0.8$, but does not
improve with p_T for the larger jet radius $R=1.2$. **ED:**
Can we explain this? Again, should we add some
of the 1-D plots?

By comparing the individual sub-figures of Figures 16, 17
and 18 we can see how the background rejection perfor-
mance depends on jet radius within the same p_T bin.
To within $\sim 25\%$, the background rejection power of
the groomed masses remains constant with respect to
the jet radius. However, we again see rather different
behaviour for the substructure variables. In all p_T bins
considered the most performant substructure variable,
 $C_2^{\beta=1}$, performs best for an anti- k_T distance parame-
ter of $R=0.8$. The performance of this variable is dra-
matically worse for the larger jet radius of $R=1.2$ (a
factor seven worse background rejection in the 1.0-1.1
TeV bin), and substantially worse for $R=0.4$. For the
other jet substructure variables considered, Γ_{Qjet} and
 $\tau_{21}^{\beta=1}$, their background rejection power also reduces for
larger jet radius, but not to the same extent. **ED: In-**
sert some nice discussion/explanation of why jet
substructure power generally gets worse as we
go to large jet radius, but groomed mass perfor-
mance does not. Probably need the 1-D figures
for this.

6.3 Combined Performance

The off-diagonal entries in Figures 16, 17 and 18 can
be used to compare the performance of different BDT
two-variable combinations, and see how this varies as
a function of p_T and R . By comparing the background
rejection achieved for the two-variable combinations to
the background rejection of the “all variables” BDT,
one can understand how much more discrimination is
possible by adding further variables to the two-variable
BDTs.

One can see that in general the most powerful two-
variable combinations involve a groomed mass and a
non-mass substructure variable ($C_2^{\beta=1}$, Γ_{Qjet} or $\tau_{21}^{\beta=1}$).
Two-variable combinations of the substructure variables
are not powerful in comparison. Which particular mass
+ substructure variable combination is the most pow-
erful depends strongly on the p_T and R of the jet, as
discussed in the sections that follow.

There is also modest improvement in the background
rejection when different groomed masses are combined,
compared to the single variable groomed mass perfor-
mance, indicating that there is complementary informa-
tion between the different groomed masses. In addition,

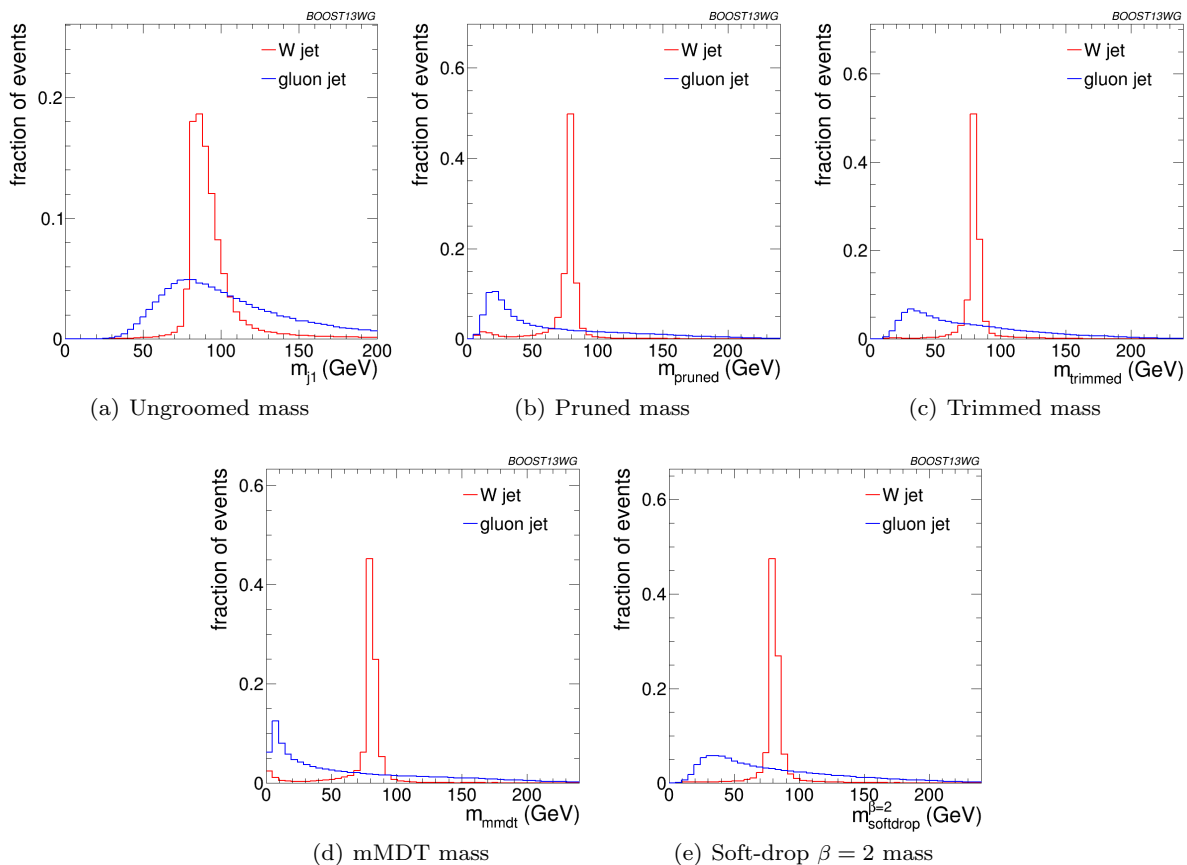


Fig. 11 Comparisons of the QCD background to the WW signal in the p_T 500-600 GeV bin using the anti- k_T $R=0.8$ algorithm: leading jet mass distributions.

there is an improvement in the background rejection when the groomed masses are combined with the ungroomed mass, indicating that grooming removes some useful discriminatory information from the jet. These observations are explored further in the section below.

Generally one can see that the $R=0.8$ jets offer the best two-variable combined performance in all p_T bins explored here. This is despite the fact that in the highest 1.0-1.1 GeV p_T bin the average separation of the quarks from the W decay is much smaller than 0.8 and well within 0.4. This conclusion could of course be susceptible to pile-up, which is not considered in this study.

6.3.1 Mass + Substructure Performance

As already noted, the largest background rejection at 70% signal efficiency are in general achieved using those two variable BDT combinations which involve a groomed mass and a non-mass substructure variable. For both $R=0.8$ and $R=1.2$ jets, the rejection power of these two variable combinations increases substantially with in-

creasing p_T , at least within the p_T range considered here.

For a jet radius of $R=0.8$, across the full p_T range considered, the groomed mass + substructure variable combinations with the largest background rejection are those which involve $C_2^{\beta=1}$. For example, in combination with $m_{sd}^{\beta=2}$, this produces a five-, eight- and fifteen-fold increase in background rejection compared to using the groomed mass alone. In Figure 19 the low degree of correlation between $m_{sd}^{\beta=2}$ versus $C_2^{\beta=1}$ that leads to these large improvements in background rejection can be seen. One can also see that what little correlation exists is rather non-linear in nature, changing from a negative to a positive correlation as a function of the groomed mass, something which helps to improve the background rejection in the region of the W mass peak.

However, when we switch to a jet radius of $R=1.2$ the picture for $C_2^{\beta=1}$ combinations changes dramatically. These become significantly less powerful, and the most powerful variable in groomed mass combinations becomes $\tau_{21}^{\beta=1}$ for all jet p_T considered. Figure 20 shows the correlation between $m_{sd}^{\beta=2}$ and $C_2^{\beta=1}$ in the p_T 1.0

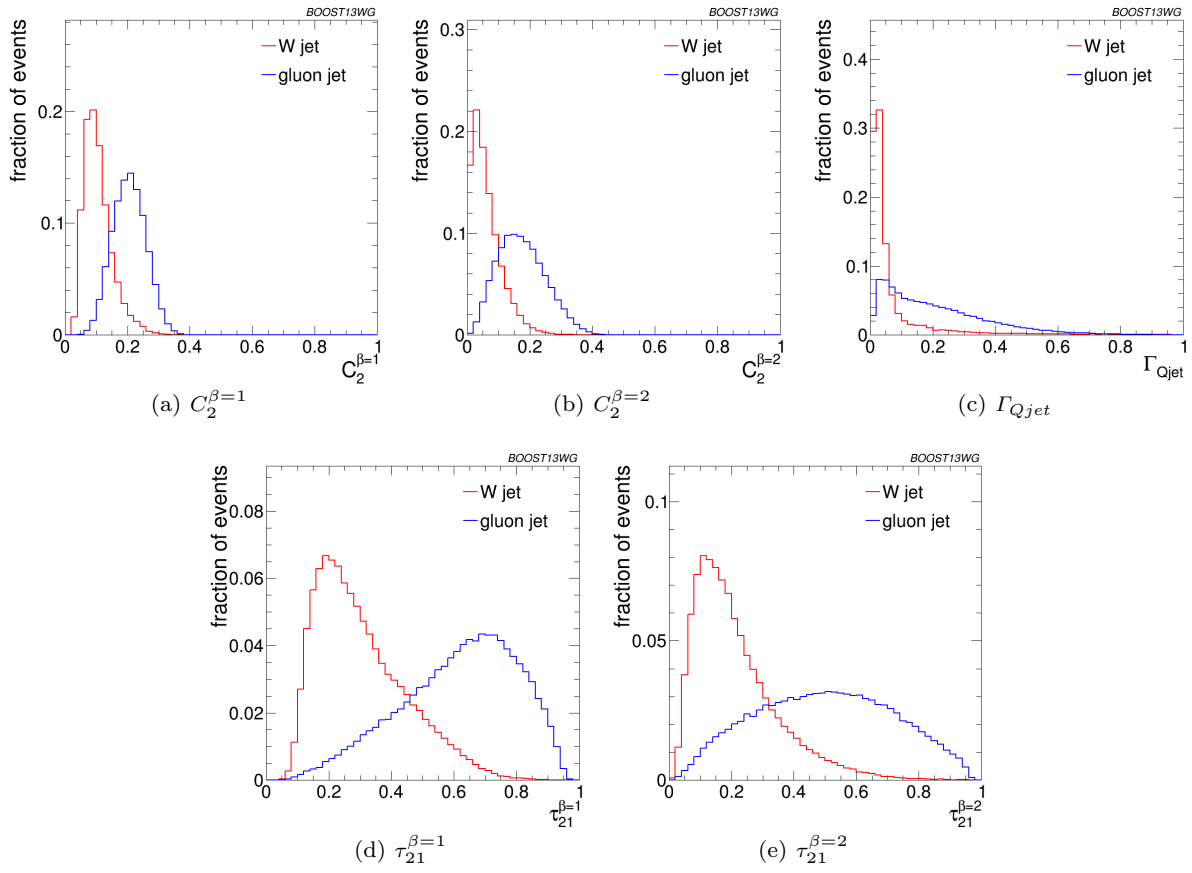


Fig. 12 Comparisons of the QCD background to the WW signal in the p_T 500-600 GeV bin using the anti- k_T $R=0.8$ algorithm: substructure variables.

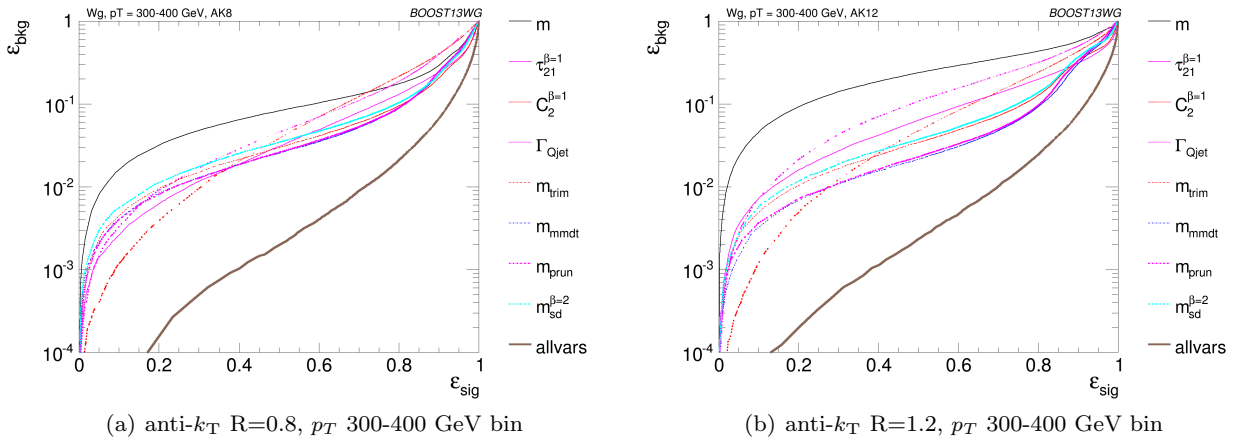


Fig. 13 The ROC curve for all single variables considered for W tagging in the p_T 300-400 GeV bin using the anti- k_T $R=0.8$ algorithm and $R=1.2$ algorithm.

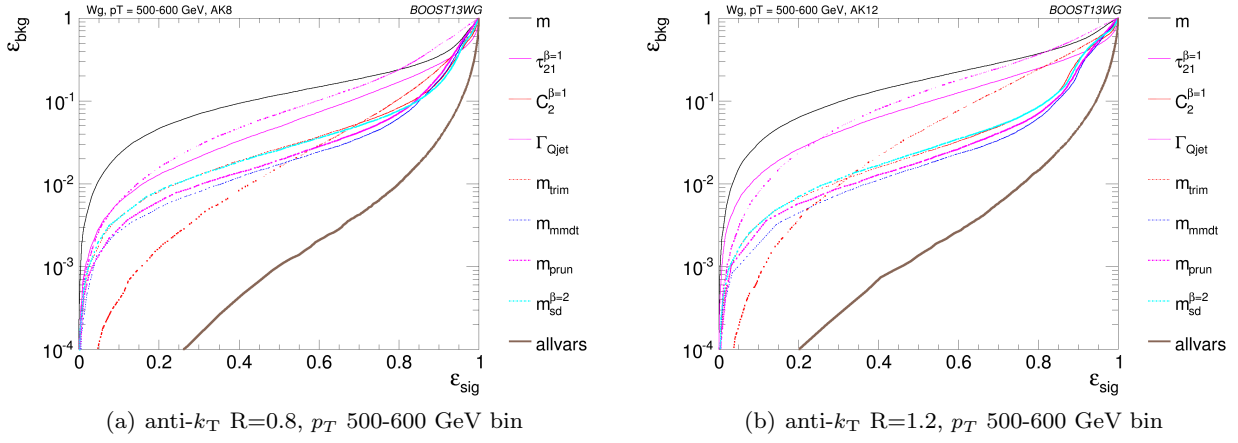


Fig. 14 The ROC curve for all single variables considered for W tagging in the p_T 500-600 GeV bin using the anti- k_T $R=0.8$ algorithm and $R=1.2$ algorithm.

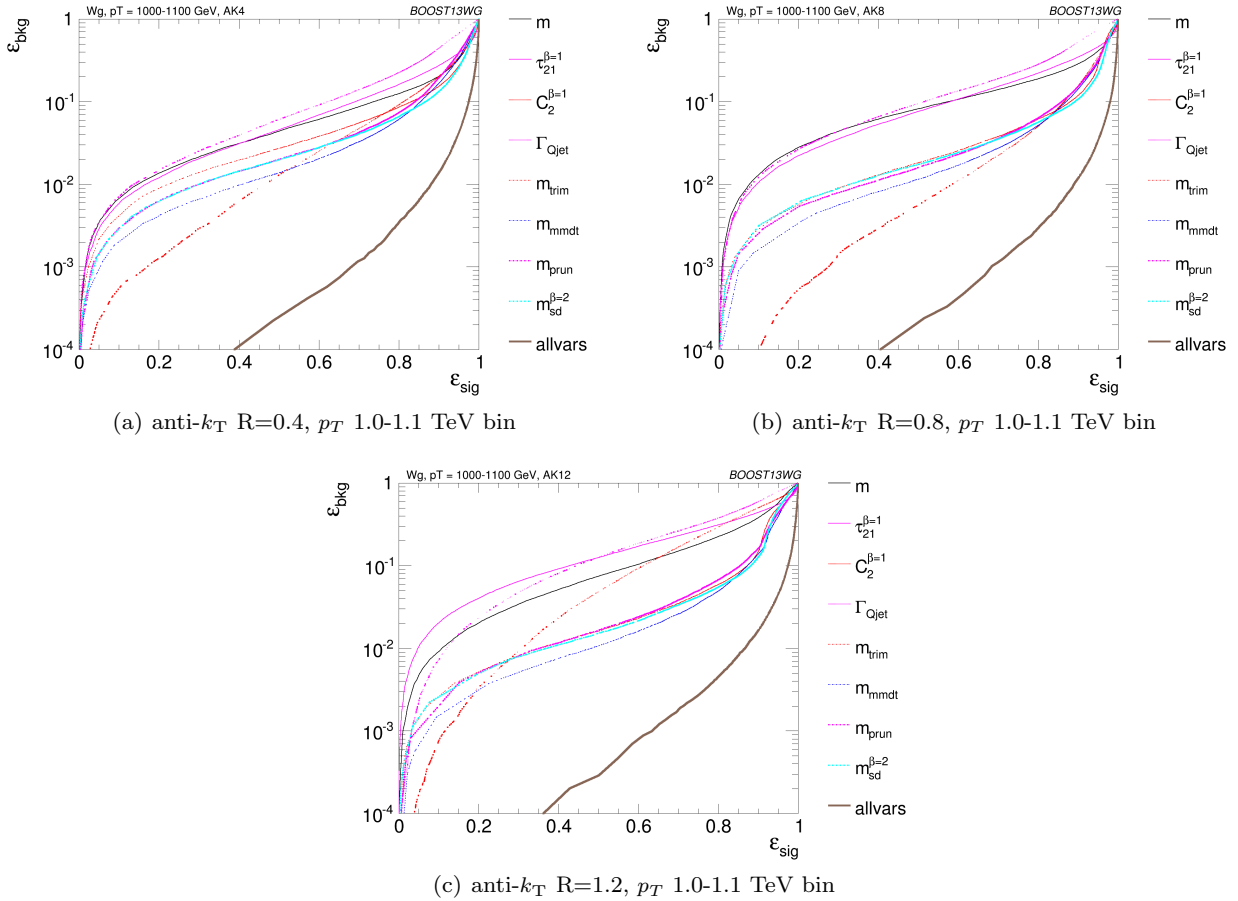


Fig. 15 The ROC curve for all single variables considered for W tagging in the p_T 1.0-1.1 TeV bin using the anti- k_T $R=0.4$ algorithm, anti- k_T $R=0.8$ algorithm and $R=1.2$ algorithm.

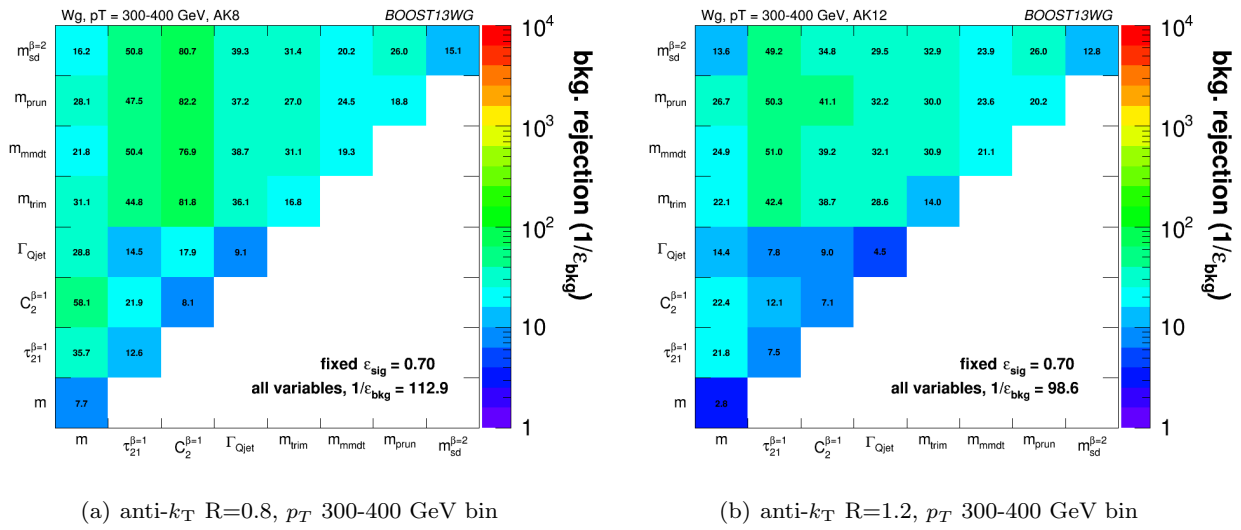


Fig. 16 The background rejection for a fixed signal efficiency (70%) of each BDT combination of each pair of variables considered, in the p_T 300-400 GeV bin using the anti- k_T $R=0.8$ algorithm and $R=1.2$ algorithm. Also shown is the background rejection for a BDT combination of all of the variables considered.

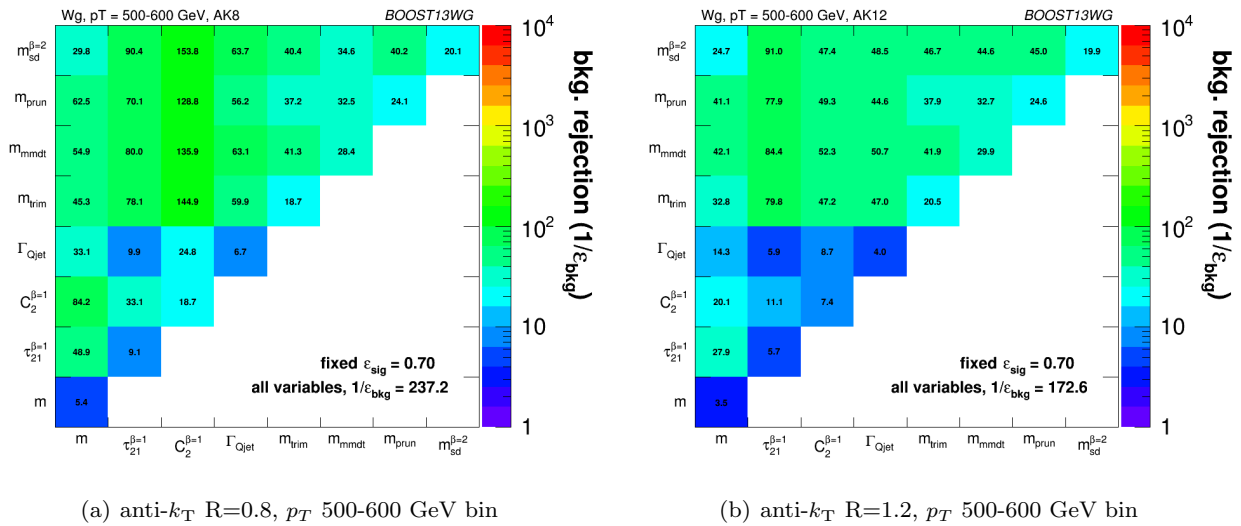


Fig. 17 The background rejection for a fixed signal efficiency (70%) of each BDT combination of each pair of variables considered, in the p_T 500-600 GeV bin using the anti- k_T $R=0.8$ algorithm and $R=1.2$ algorithm. Also shown is the background rejection for a BDT combination of all of the variables considered.

687 - 1.2 TeV bin for the various jet radii considered. Fig-697
 688 ure 21 is the equivalent set of distributions for $m_{sd}^{\beta=2}$ 698
 689 and $\tau_{21}^{\beta=1}$. One can see from Figure 20 that, due to the 699
 690 sensitivity of the observable to soft, wide-angle ra-700
 691 diation, as the jet radius increases $C_2^{\beta=1}$ increases and
 692 becomes more and more smeared out for both signal 701
 693 and background, leading to worse discrimination power.
 694 This does not happen to the same extent for $\tau_{21}^{\beta=1}$. We 702
 695 can see from Figure 21 that the negative correlation be-703
 696 tween $m_{sd}^{\beta=2}$ and $\tau_{21}^{\beta=1}$ that is clearly visible for $R=0.4$ 704
 705

decreases for larger jet radius, such that the groomed
 mass and substructure variable are far less correlated
 and $\tau_{21}^{\beta=1}$ offers improved discrimination within a $m_{sd}^{\beta=2}$
 mass window.

6.3.2 Mass + Mass Performance

The different groomed masses and the ungroomed mass
 are of course not fully correlated, and thus one can al-
 ways see some kind of improvement in the background
 rejection (relative to the single mass performance) when

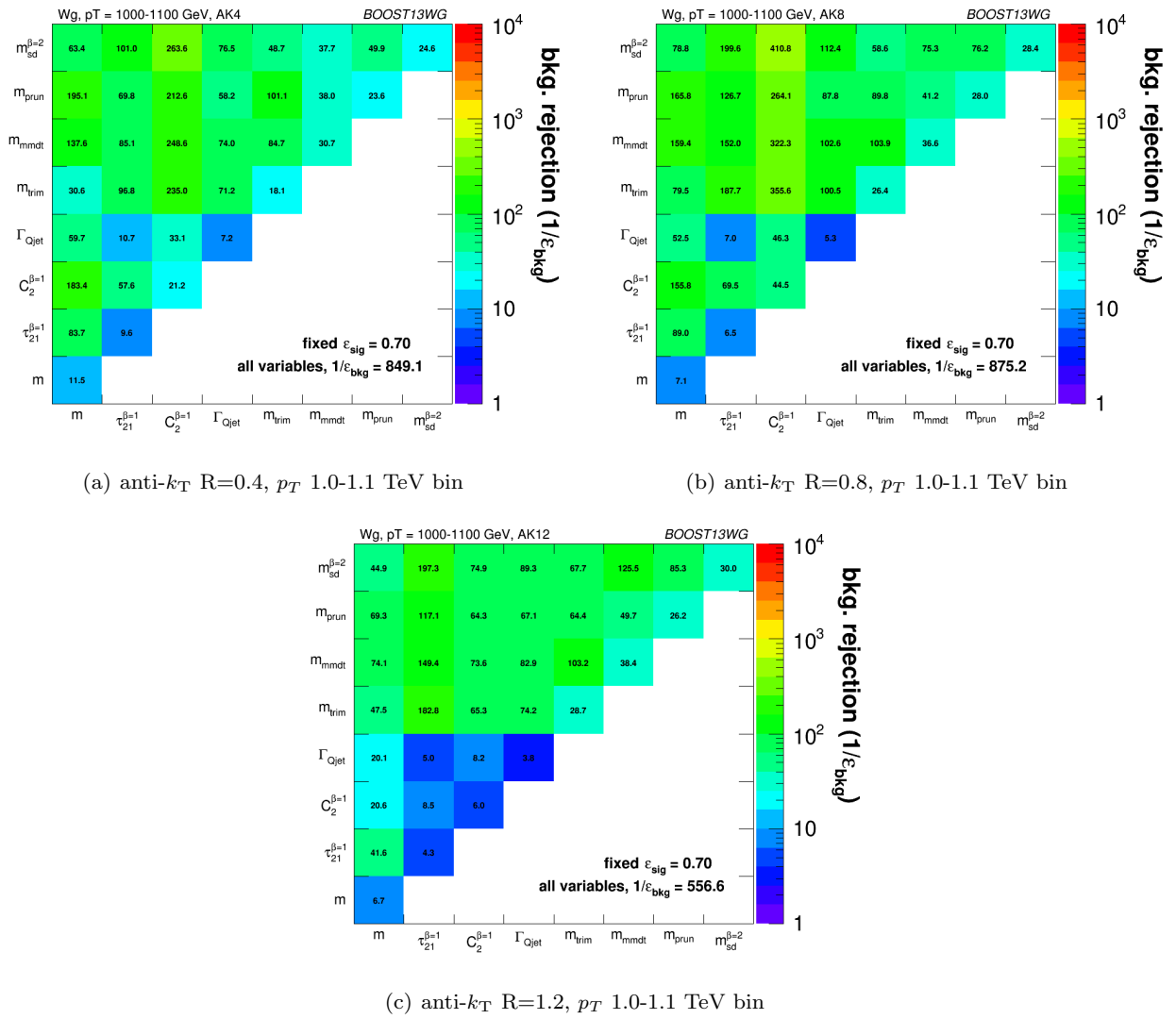


Fig. 18 The background rejection for a fixed signal efficiency (70%) of each BDT combination of each pair of variables considered, in the p_T 1.0-1.1 TeV bin using the anti- k_T $R=0.4$, $R=0.8$ and $R=1.2$ algorithm. Also shown is the background rejection for a BDT combination of all of the variables considered.

706 two different mass variables are combined in the BDT.⁷²¹
 707 However, in some cases the improvement can be dra-⁷²²
 708 matic, particularly at higher p_T , and particularly for⁷²³
 709 combinations with the ungroomed mass. For example,⁷²⁴
 710 in Figure 18 we can see that in the p_T 1.0-1.1 TeV⁷²⁵
 711 the combination of pruned mass with ungroomed mass⁷²⁶
 712 produces a greater than eight-fold improvement in the⁷²⁷
 713 background rejection for $R=0.4$ jets, a greater than five-⁷²⁸
 714 fold improvement for $R=0.8$ jets, and a factor \sim two im-⁷²⁹
 715 provement for $R=1.2$ jets. A similar behaviour can be⁷³⁰
 716 seen for mMDT mass. In Figures 22, 23 and 24 is shown⁷³¹
 717 the 2-D correlation plots of the pruned mass versus the⁷³²
 718 ungroomed mass separately for the WW signal and gg ⁷³³
 719 background samples in the p_T 1.0-1.1 TeV bin, for the⁷³⁴
 720 various jet radii considered. For comparison, the corre-⁷³⁵

lation of the trimmed mass with the ungroomed mass, a combination that does not improve on the single mass as dramatically, is shown. In all cases one can see that there is a much smaller degree of correlation between the pruned mass and the ungroomed mass in the backgrounds sample than for the trimmed mass and the ungroomed mass. This is most obvious in Figure 22, where the high degree of correlation between the trimmed and ungroomed mass is expected, since with the parameters used (in particular $R_{trim} = 0.2$) we cannot expect trimming to have a significant impact on an $R=0.4$ jet. The reduced correlation with ungroomed mass for pruning in the background means that, once we have made the requirement that the pruned mass is consistent with a W (i.e. ~ 80 GeV), a relatively large difference be-

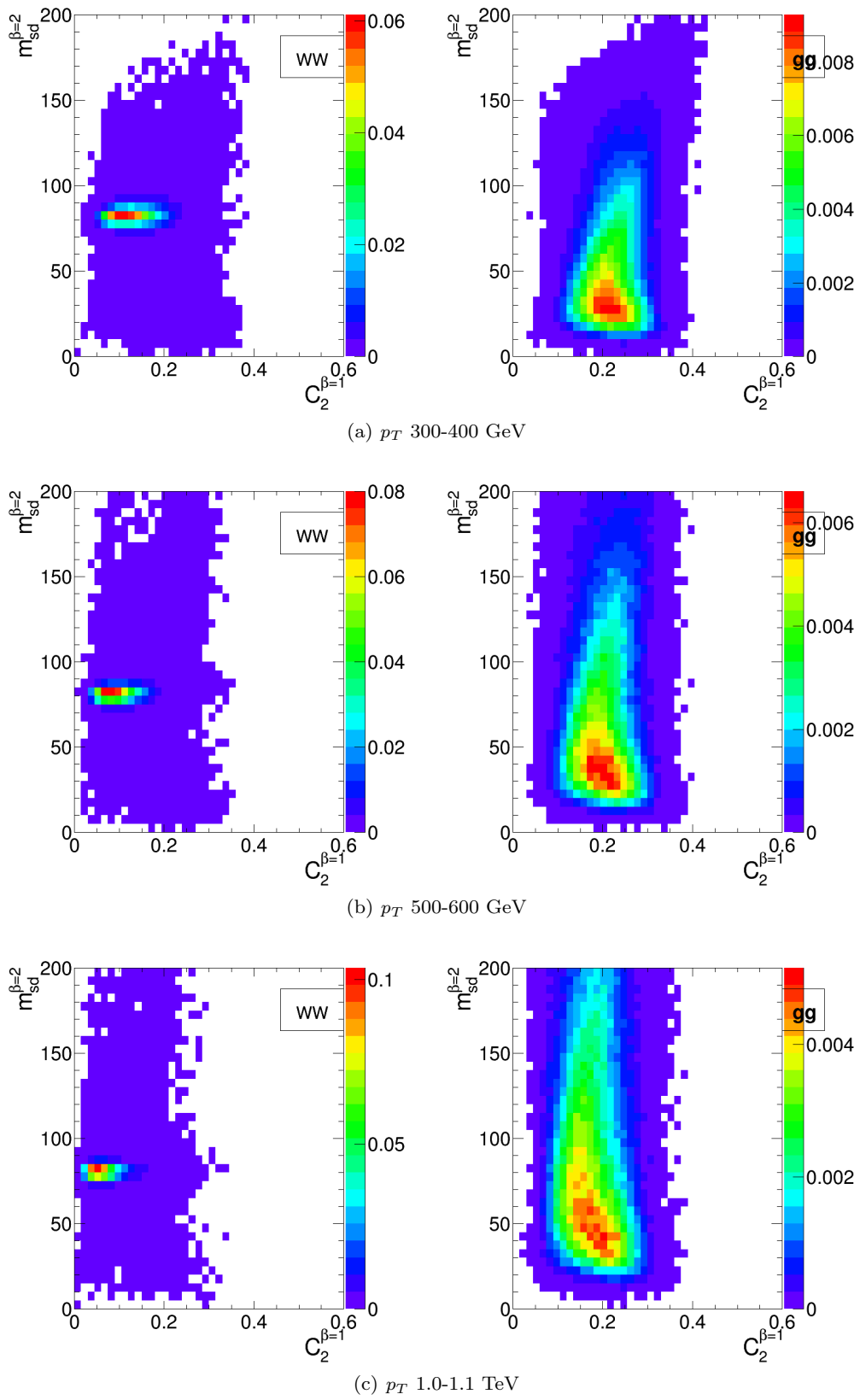


Fig. 19 2-D plots showing $m_{sd}^{\beta=2}$ versus $C_2^{\beta=1}$ for $R=0.8$ jets in the various p_T bins considered.

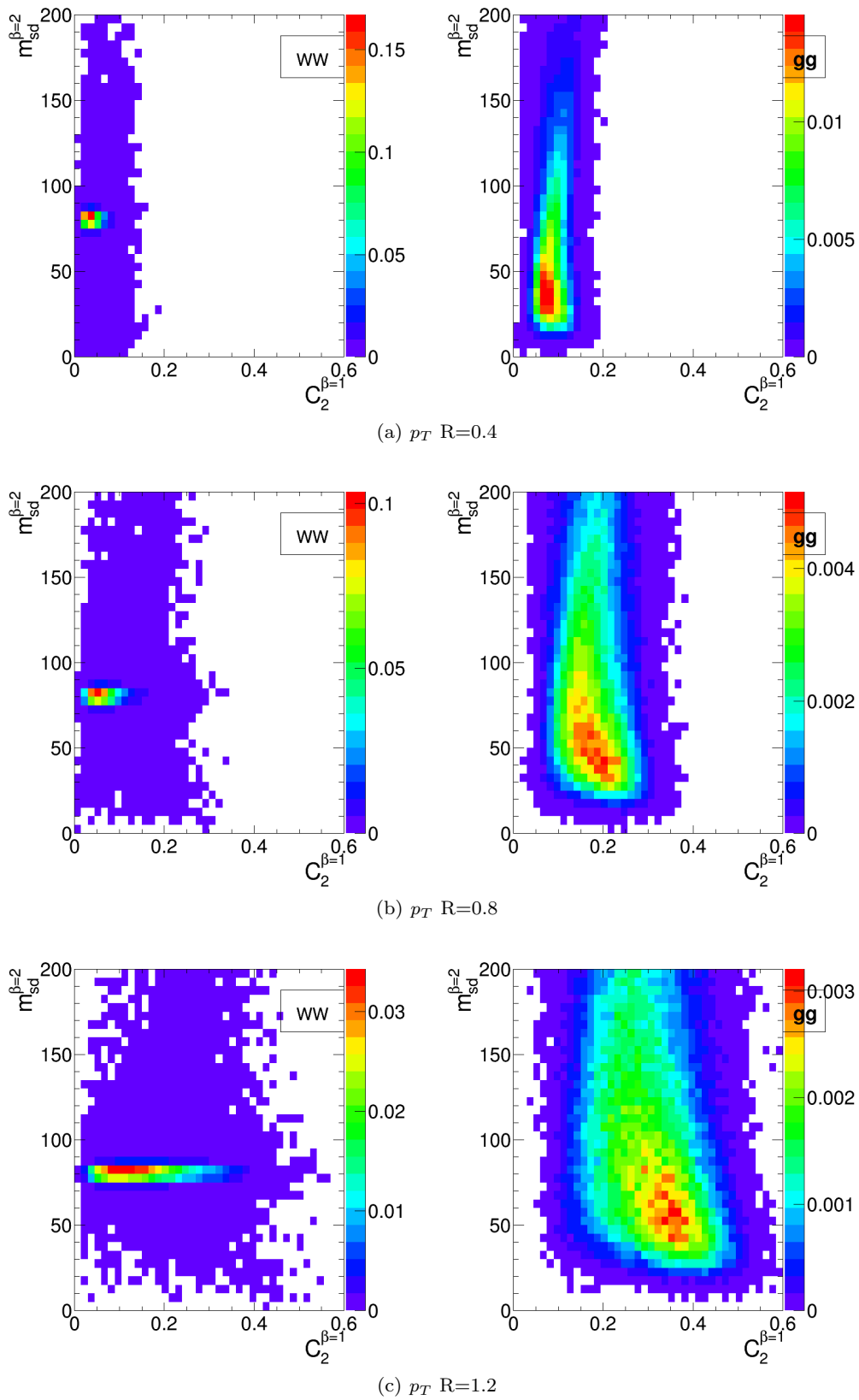


Fig. 20 2-D plots showing $m_{sd}^{\beta=2}$ versus $C_2^{\beta=1}$ for $R=0.4, 0.8$ and 1.2 jets in the p_T 1.0-1.1 TeV bin.

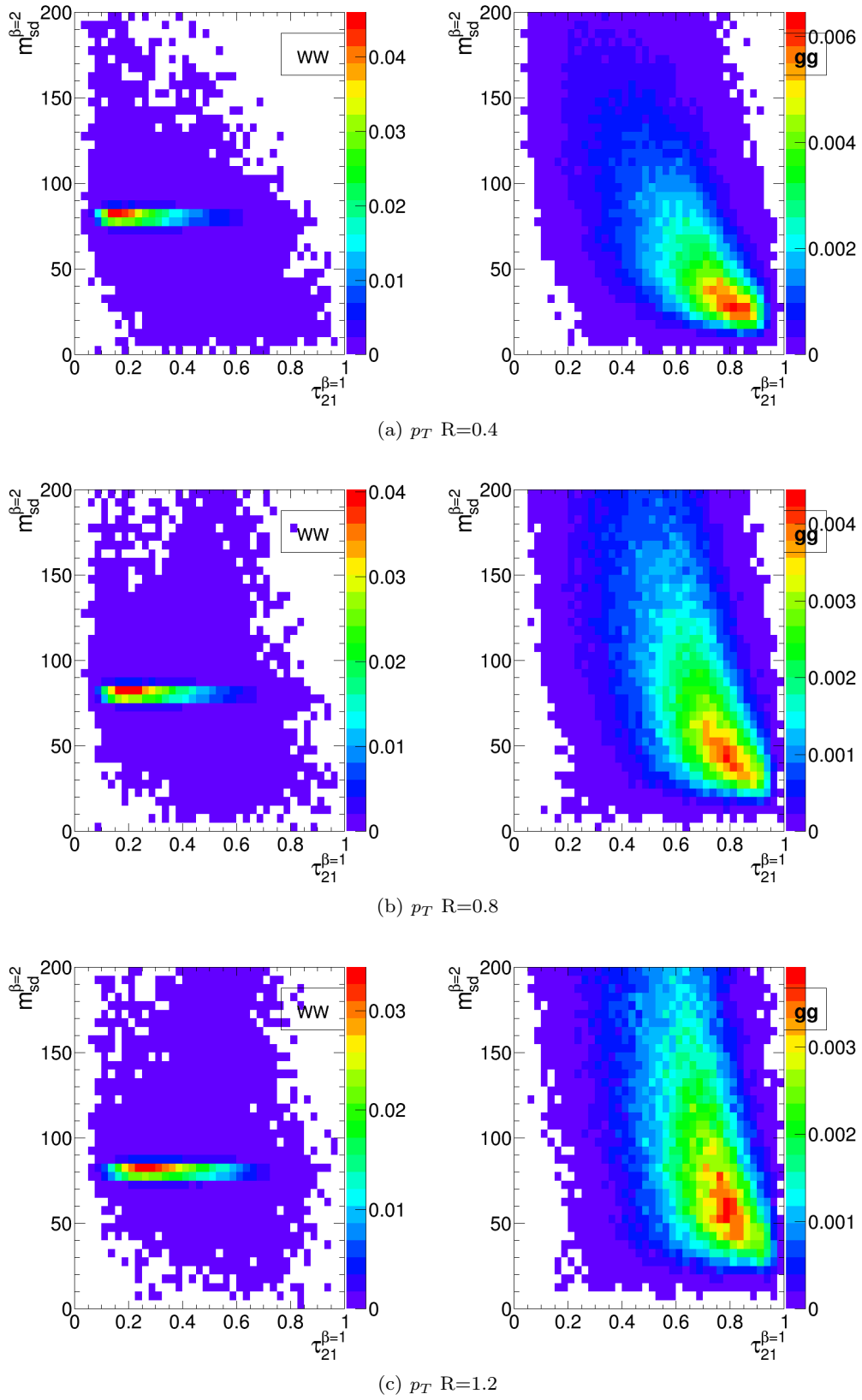


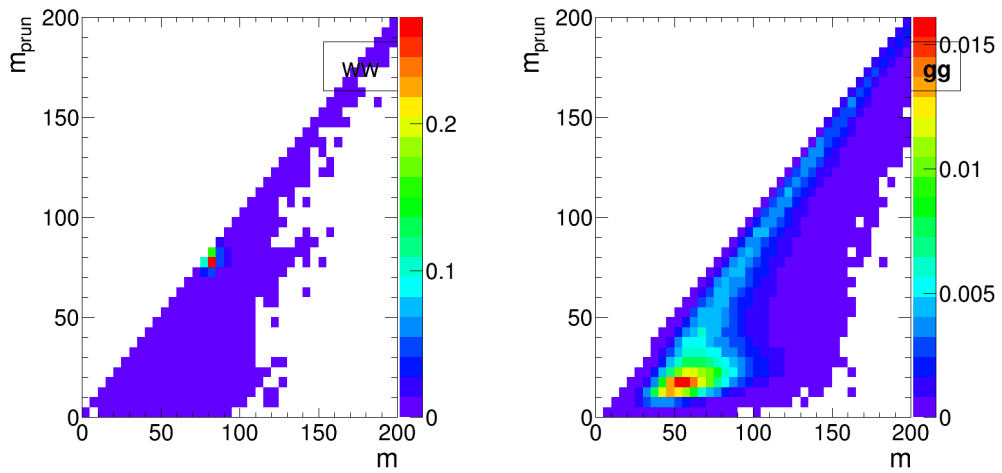
Fig. 21 2-D plots showing $m_{sd}^{\beta=2}$ versus $\tau_{21}^{\beta=1}$ for $R=0.4, 0.8$ and 1.2 jets in the p_T 1.0-1.1 TeV bin.

736 tween signal and background in the ungroomed mass
737 still remains, and can be exploited to improve the back-
738 ground rejection further. In other words, many of the
739 background events which pass the pruned mass require-
740 ment do so because they are shifted to lower mass (to
741 be within a signal mass window) by the grooming, but
742 these events still have the property that they look very
743 much like background events before the grooming. A
744 single requirement on the groomed mass only does not
745 exploit this. Of course, the impact of pile-up, not con-
746 sidered in this study, could significantly limit the degree
747 to which the ungroomed mass could be used to improve
748 discrimination in this way.

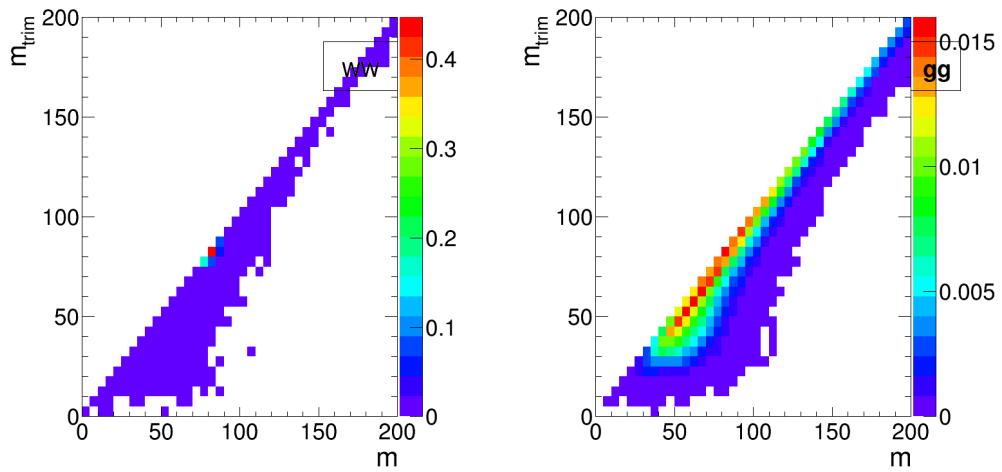
749 6.3.3 “All Variables” Performance

750 As well as the background rejection at a fixed 70% sig-
751 nal efficiency for two-variable combinations, Figures 16, 17
752 and 18 also report the background rejection achieved
753 by a combination of all the variables considered into a
754 single BDT discriminant. One can see that, in all cases,
755 the rejection power of this “all variables” BDT is signif-
756 icantly larger than the best two-variable combination,
757 by between a factor 2-3. This indicates that beyond the
758 best two-variable combination there is still significant
759 complementary information available in the remaining
760 variables in order to improve the discrimination of sig-
761 nal and background.

762 **ED: This section will be filled in when we**
763 **have got the 3-variable combination studies, so**
764 **we have a better idea where the dramatic in-**
765 **crease in rejection power with “all variables” is**
766 **coming from. Would also be good to show per-**
767 **haps some of the “all variables” BDT discrimi-**
768 **nants in 1-D plots.**

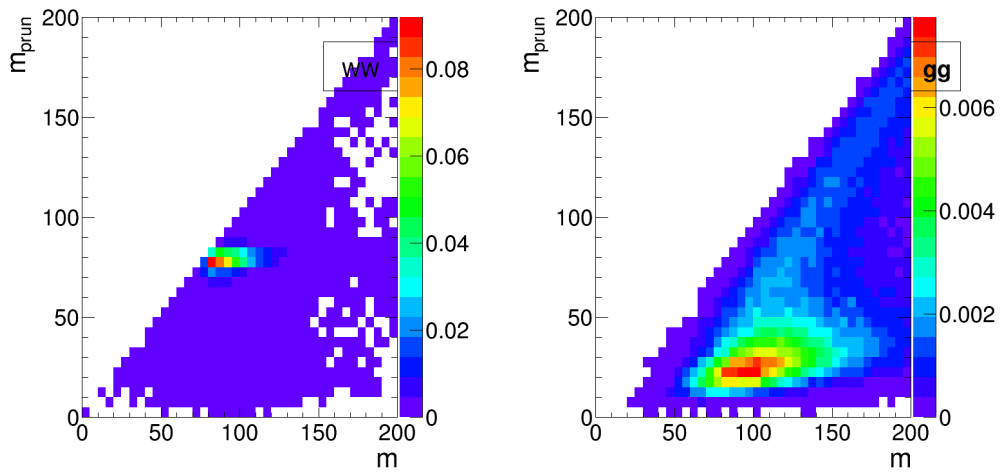


(a) Pruned mass vs ungroomed mass

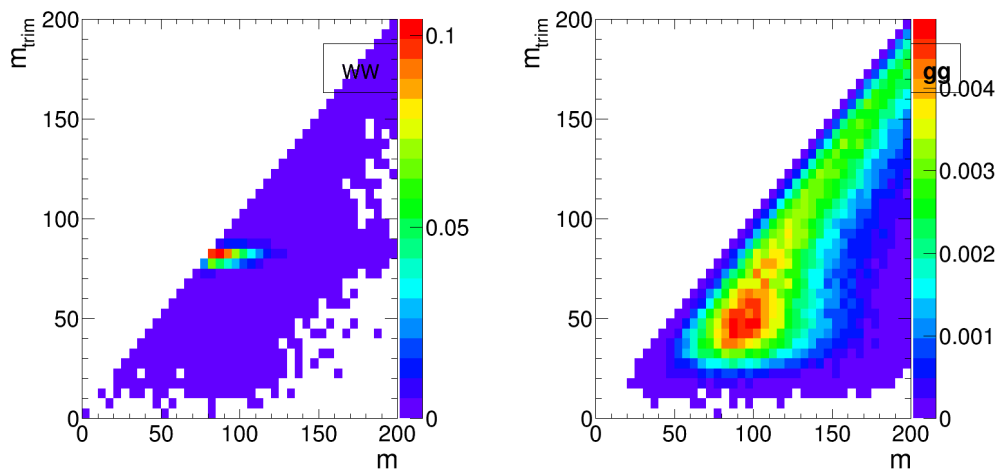


(b) Trimmed mass vs ungroomed mass

Fig. 22 2-D plots showing the correlation between groomed and ungroomed mass for WW and gg events in the p_T 1.0-1.1 TeV bin using the anti- k_T $R=0.4$ algorithm.

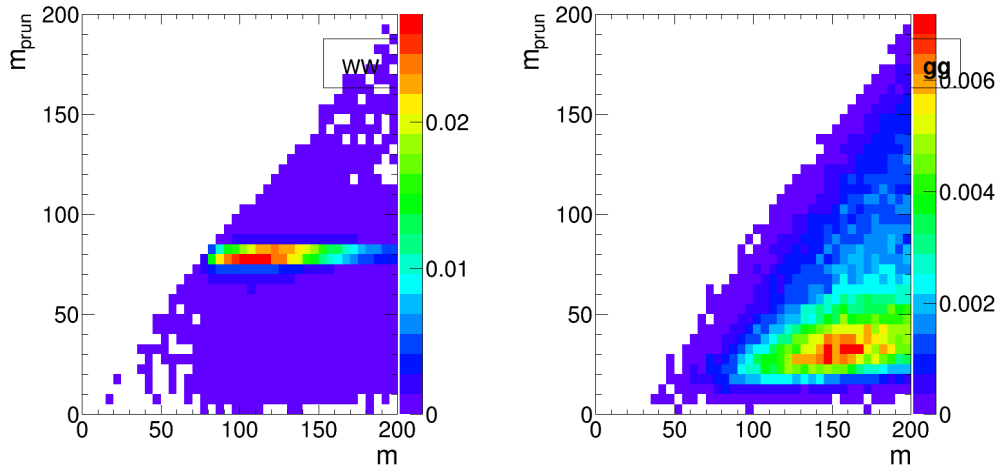


(a) Pruned mass vs ungroomed mass

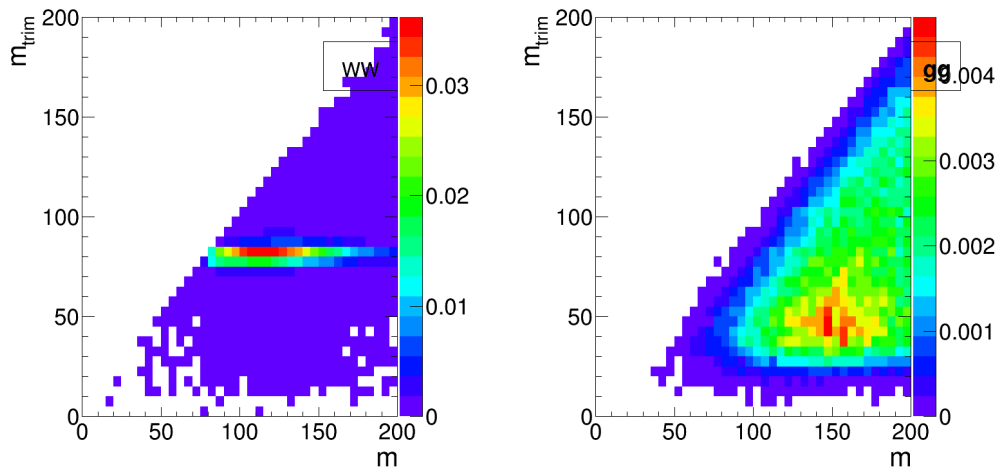


(b) Trimmed mass vs ungroomed mass

Fig. 23 2-D plots showing the correlation between groomed and ungroomed mass for WW and gg events in the p_T 1.0-1.1 TeV bin using the anti- k_T $R=0.8$ algorithm.



(a) Pruned mass vs ungroomed mass



(b) Trimmed mass vs ungroomed mass

Fig. 24 2-D plots showing the correlation between groomed and ungroomed mass for WW and gg events in the p_T 1.0-1.1 TeV bin using the anti- k_T $R=1.2$ algorithm.

7 Top Tagging

In this section, we study the identification of boosted top quarks at Run II of the LHC. Boosted top quarks result in large-radius jets with complex substructure containing a b -subjett and a boosted W . The additional kinematic handles coming from the reconstruction of the W mass and b -tagging allows a very high degree of discrimination of top quark jets from QCD backgrounds.

We consider top quarks with moderate boost (600–1000 GeV), and perhaps most interestingly, at high boost ($\gtrsim 1500$ GeV). Top tagging faces several challenges in the high- p_T regime. For such high- p_T jets, the b -tagging efficiencies are no longer reliably known. Also, the top jet can also be accompanied by additional

radiation with $p_T \sim m_t$, leading to combinatoric ambiguities of reconstructing the top and W , and the possibility that existing taggers or observables shape the background by looking for subjet combinations that reconstruct m_t/m_W . To study this, we examine the performance of both mass-reconstruction variables, as well as shape observables that probe the three-pronged nature of the top jet and the accompanying radiation pattern.

7.1 Methodology

We study a number of top-tagging strategies, in particular:

1. HEPTopTagger
2. Johns Hopkins Tagger (JH)
3. Trimming
4. Pruning

The top taggers have criteria for reconstructing a top and W candidate, and a corresponding top and W mass, as described in Section 3.3, while the grooming algorithms (trimming and pruning) do not incorporate a W -identification step. For a level playing field, where grooming is used we construct a W candidate mass, m_W , from the three leading subjets by taking the mass of the pair of subjets with the smallest invariant mass; in the case that only two subjets are reconstructed, we take the mass of the leading subjet. The top mass, m_t , is the mass of the groomed jet. All of the above taggers and groomers incorporate a step to remove pile-up and other soft radiation.

We also consider the performance of jet shape observables. In particular, we consider the N -subjettiness ratios $\tau_{32}^{\beta=1}$ and $\tau_{21}^{\beta=1}$, energy correlation function ratios $C_3^{\beta=1}$ and $C_2^{\beta=1}$, and the Qjet mass volatility Γ . In addition to the jet shape performance, we combine the jet shapes with the mass-reconstruction methods described above to determine the optimal combined performance.

For determining the performance of multiple variables, we combine the relevant tagger output observables and/or jet shapes into a boosted decision tree (BDT), which determines the optimal cut. Additionally, because each tagger has two input parameters, as described in Section 3.3, we scan over reasonable values of the parameters to determine the optimal value for each top tagging signal efficiency **ED: Optimal value is that which gives largest bkgd rejection?**. This allows a direct comparison of the optimized version of each tagger. The input values scanned for the various algorithms are:

- **HEPTopTagger:** $m \in [30, 100]$ GeV, $\mu \in [0.5, 1]$

- 833 – **JH Tagger:** $\delta_p \in [0.02, 0.15]$, $\delta_R \in [0.07, 0.2]$
- 834 – **Trimming:** $f_{\text{cut}} \in [0.02, 0.14]$, $R_{\text{trim}} \in [0.1, 0.5]$
- 835 – **Pruning:** $z_{\text{cut}} \in [0.02, 0.14]$, $R_{\text{cut}} \in [0.1, 0.6]$

836 7.2 Single-observable performance

837 We start by investigating the behaviour of individual
 838 jet substructure observables. Because of the rich, three-
 839 pronged structure of the top decay, it is expected that
 840 combinations of masses and jet shapes will far out-
 841 perform single observables in identifying boosted tops.
 842 However, a study of the top-tagging performance of sin-
 843 gle variables facilitates a direct comparison with the W
 844 tagging results in Section 6, and also allows a straight-
 845 forward examination of the performance of each observ-
 846 able for different p_T and jet radius.

847 **ED: I think the conclusions in this paragraph,**
 848 **that for W-tagging the shape variables perform**
 849 **as well as the mass, are not generally true, only**
 850 **holds for one variable $C_2^{\beta=1}$ at small-R, and not**
 851 **for τ_{21} .** Fig. 25 shows the ROC curves for each of the
 852 top-tagging observables, with the bare (ungroomed) jet
 853 mass also plotted for comparison. Unlike W tagging,
 854 the jet shape observables perform more poorly than jet
 855 mass. As an example illustrating why this is the case,
 856 consider N -subjettiness. The W is two-pronged and the
 857 top is three-pronged; therefore, we expect τ_{21} and τ_{32}
 858 to be the best-performant N -subjettiness ratio, respec-
 859 tively. However, τ_{21} also contains an implicit cut on the
 860 denominator, τ_1 , which is strongly correlated with jet
 861 mass. Therefore, τ_{21} combines both mass and shape in-
 862 formation to some extent. By contrast, and as is clear
 863 in Fig.25(a), the best shape for top tagging is τ_{32} , which
 864 contains no information on the mass. Therefore, it is un-
 865 surprising that the shapes most useful for top tagging
 866 are less sensitive to the jet mass, and under-perform rel-
 867 ative to the corresponding observables for W tagging.

868 Of the two top tagging algorithms, we can see from
 869 Figure 25 that the Johns Hopkins (JH) tagger out-
 870 performs the HEPTopTagger in terms of its signal-to-
 871 background separation power in both the top and W
 872 candidate masses. This discrepancy is larger at higher
 873 p_T and larger jet radius. **ED: We do not show in**
 874 **ROC curves that the discrepancy is larger at**
 875 **high p_T and jet radius, should we?** In Figure 26
 876 we show the histograms for the top mass output from
 877 the JH and HEPTopTagger for different R in the p_T
 878 1.5-1.6 TeV bin, and in Figure 27 for different p_T
 879 at $R = 0.8$, optimized at a signal efficiency of 30%.
 880 One can see from these figures that the likely reason
 881 for the better performance of the JH tagger is that, in
 882 the HEPTopTagger algorithm, the jet is filtered to se-
 883 lect the five hardest subjects, and then three subjects are

884 chosen which reconstruct the top mass. This require-
 885 ment tends to shape a peak in the QCD background
 886 around m_t for the HEPTopTagger, while the JH tagger
 887 has no such requirement. It has been suggested by An-
 888 ders *et al.* [?] that performance in the HEPTopTagger
 889 may be improved by selecting the three subjects recon-
 890 structing the top only among those that pass the W
 891 mass constraints, which somewhat reduces the shap-
 892 ing of the background. Note that both the JH tagger
 893 and the HEPTopTagger are superior to the grooming
 894 algorithms at using the W candidate inside of the top
 895 for signal discrimination; this is because the the prun-
 896 ing and trimming algorithms do not have inherent W -
 897 identification steps and are not optimized for this pur-
 898 pose.

In Figures 28 and 31 we directly compare ROC
 curves for jet shape observable performance and top
 mass performance respectively in the three different p_T
 bins considered whilst keeping the jet radius fixed at
 $R=0.8$. The input parameters of the taggers, groomers
 and shape variables are separately optimized in each
 p_T bin. One can see from Figure 28 that the tagging
 performance of jet shapes do not change substantially
 with p_T . The observables $\tau_{32}^{(\beta=1)}$ and Qjet volatility Γ
 have the most variation and tend to degrade with higher
 p_T , as can be seen in Figures 29 and 30). This makes
 sense, as higher- p_T QCD jets have more, harder emis-
 sions within the jet, giving rise to substructure that
 fakes the signal. By contrast, from Figure 31 we can
 see that most of the top mass observables have superior
 performance at higher p_T due to the radiation from the
 top quark becoming more collimated. The notable ex-
 ception is the HEPTopTagger, which degrades at higher
 p_T , likely in part due to the background-shaping effects
 discussed earlier.

In Figures 32 and 36 we directly compare ROC
 curves for jet shape observable performance and top
 mass performance respectively for the three different jet
 radii considered within the p_T 1.5-1.6 TeV bin. Again,
 the input parameters of the taggers, groomers and shape
 variables are separately optimized for each jet radius.
 We can see from these figures that most of the top
 tagging variables, both shape and reconstructed top
 mass, perform best for smaller radius. This is likely
 because, at such high p_T , most of the radiation from
 the top quark is confined within $R = 0.4$, and having
 a larger jet radius makes the observable more suscep-
 tible to contamination from the underlying event and
 other uncorrelated radiation. In Figures 33, 34 and 35,
 we compare the individual top signal and QCD back-
 ground distributions for each shape variable considered
 in the p_T 1.5-1.6 TeV bin for the various jet radii. One
 can see that the distributions for both signal broaden

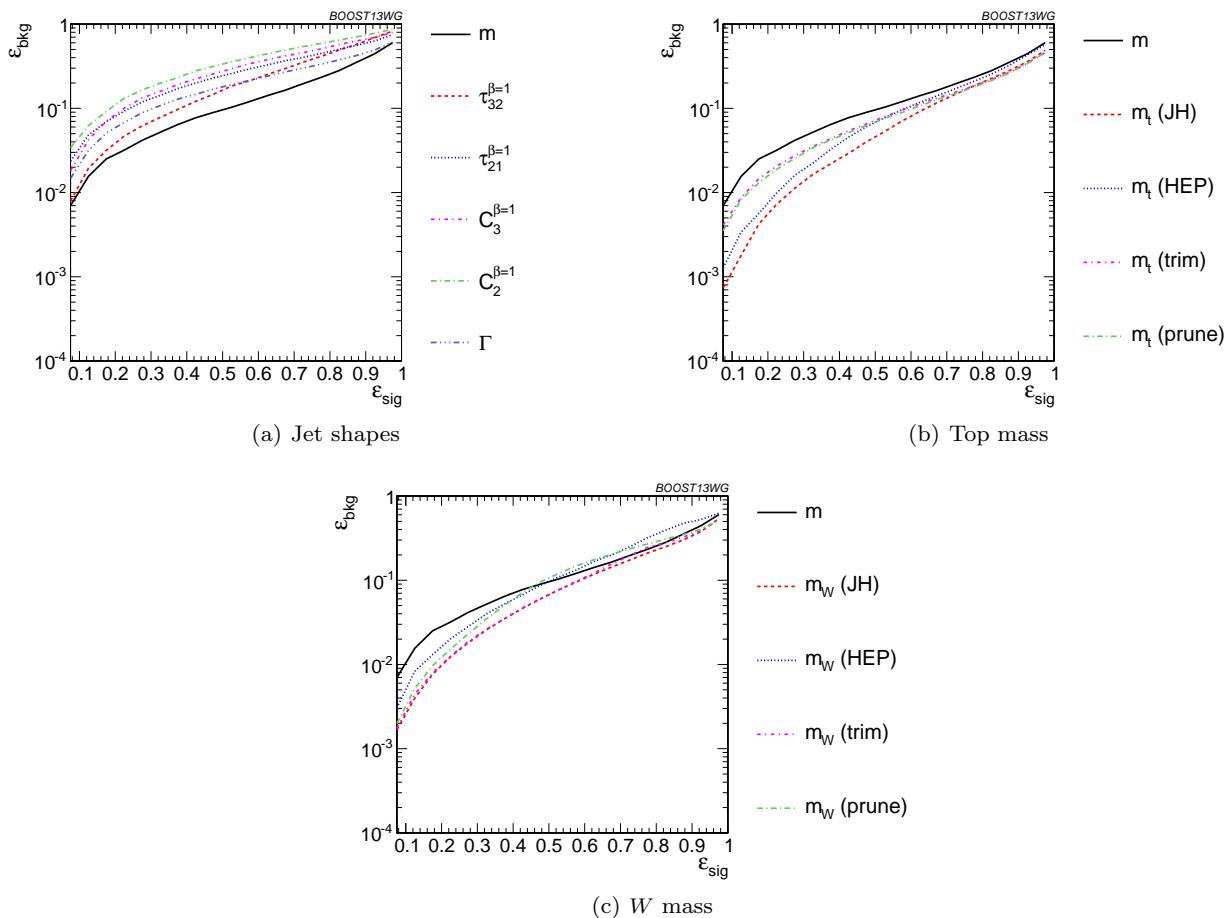


Fig. 25 Comparison of single-variable top-tagging performance in the $p_T = 1 - 1.1$ GeV bin using the anti- k_T , $R=0.8$ algorithm.

937 with increasing R , degrading the discriminating power.⁹⁵⁶
 938 For $C_2^{(\beta=1)}$ and $C_3^{(\beta=1)}$, the background distributions⁹⁵⁷
 939 are shifted upward as well. Therefore, the discriminat-⁹⁵⁸
 940 ing power generally gets worse with increasing R . The⁹⁵⁹
 941 main exception is for $C_3^{(\beta=1)}$, which performs optimally⁹⁶⁰
 942 at $R = 0.8$; in this case, the signal and background coin-⁹⁶¹
 943 cidentally happen to have the same distribution around⁹⁶²
 944 $R = 0.4$, and so $R = 0.8$ gives better discrimination.⁹⁶³
 945 **ED: Should we also include 1-D plots compar-**⁹⁶⁴
 946 **ing signal vs bkgd in the top mass, and how this**⁹⁶⁵
 947 **varies with radius? Having said that, there a**⁹⁶⁶
 948 **lot of 1-D plots here already, might want to try**
 949 **and cut down.**

950 7.3 Performance of multivariable combinations

951 We now consider various BDT combinations of the ob-⁹⁷²
 952 servables from Section 7.2, using the techniques de-⁹⁷³
 953 scribed in Section 4. In particular, we consider the per-⁹⁷⁴
 954 formance of individual taggers such as the JH tagger⁹⁷⁵
 955 and HEPTopTagger, which output information about⁹⁷⁶

the top and W candidate masses and the helicity angle; groomers, such as trimming and pruning, which remove soft, uncorrelated radiation from the top candidate to improve mass reconstruction, and to which we have added a W reconstruction step; and the combination of the outputs of the above taggers/groomers, both with each other, and with shape variables such as N -subjettiness ratios and energy correlation ratios. For all observables with tuneable input parameters, we scan and optimize over realistic values of such parameters, as described in Section 7.1.

In Figure 37, we directly compare the performance of the HEPTopTagger, the JH tagger, trimming, and pruning, in the $p_T = 1 - 1.1$ TeV bin using jet radius $R=0.8$, where both m_t and m_W are used in the groomers. Generally, we find that pruning, which does not naturally incorporate subjects into the algorithm, does not perform as well as the others. Interestingly, trimming, which does include a subject-identification step, performs comparably to the HEPTopTagger over much of the range, possibly due to the background-shaping observed

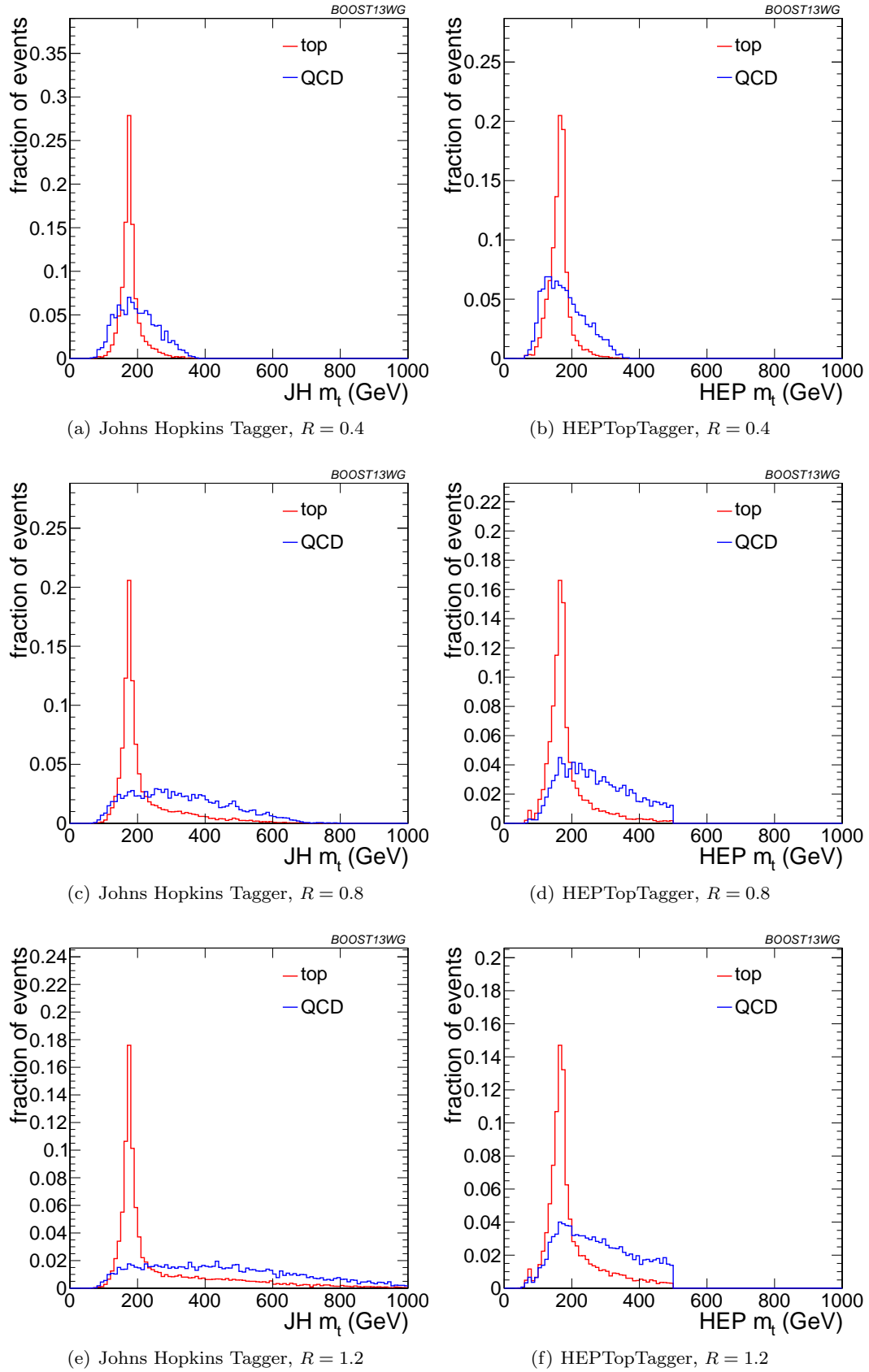


Fig. 26 Comparison of top mass reconstruction with the JH and HEPTopTaggers at different R using the anti- k_T algorithm, $p_T = 1.5 - 1.6$ TeV. Each histogram is shown for the working point optimized for best performance with m_t in the $0.3 - 0.35$ signal efficiency bin, and is normalized to the fraction of events passing the tagger.

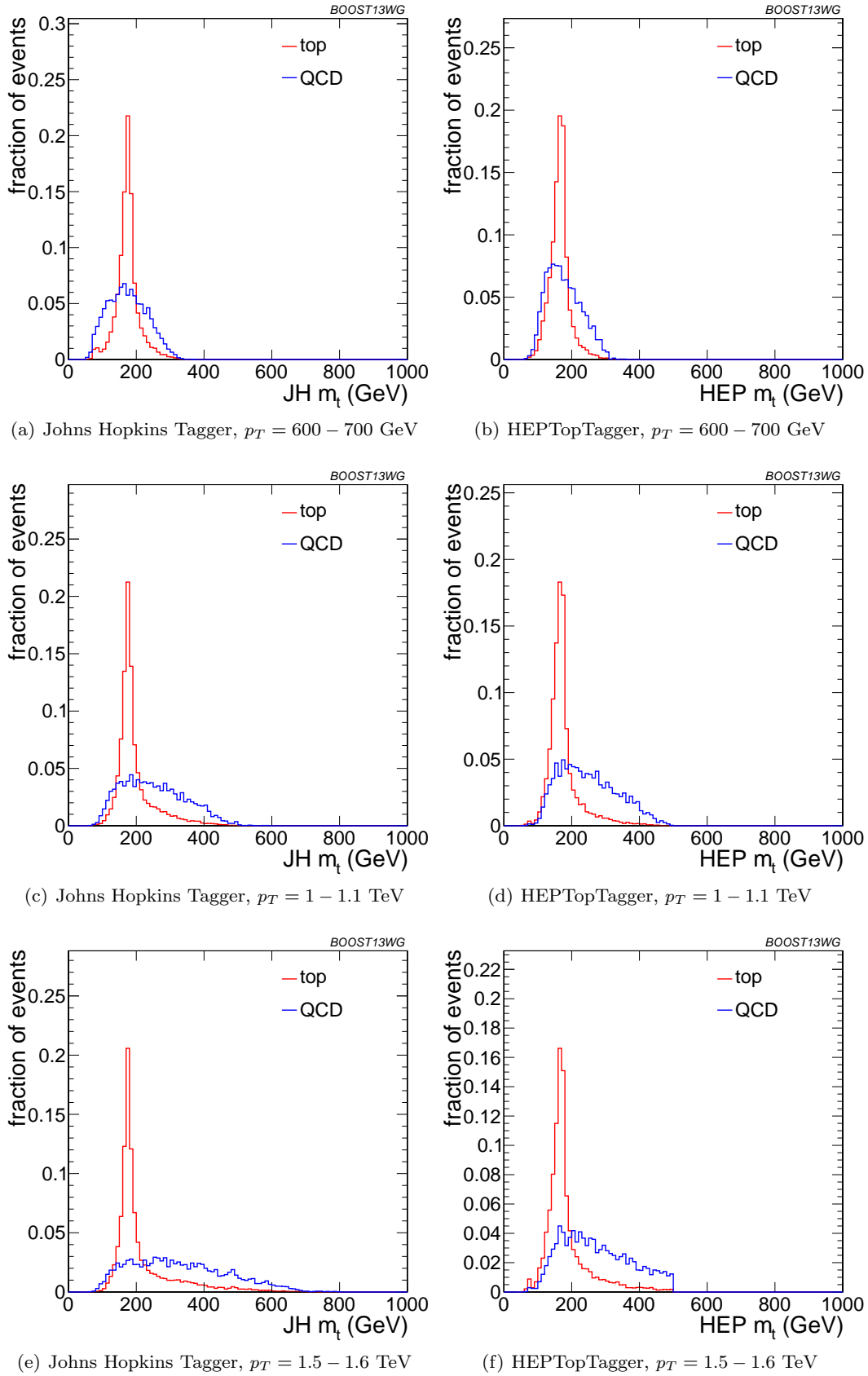


Fig. 27 Comparison of top mass reconstruction with the JH and HEP TopTaggers at different p_T using the anti- k_T algorithm, $R = 0.8$. Each histogram is shown for the working point optimized for best performance with m_t in the 0.3 – 0.35 signal efficiency bin, and is normalized to the fraction of events passing the tagger.

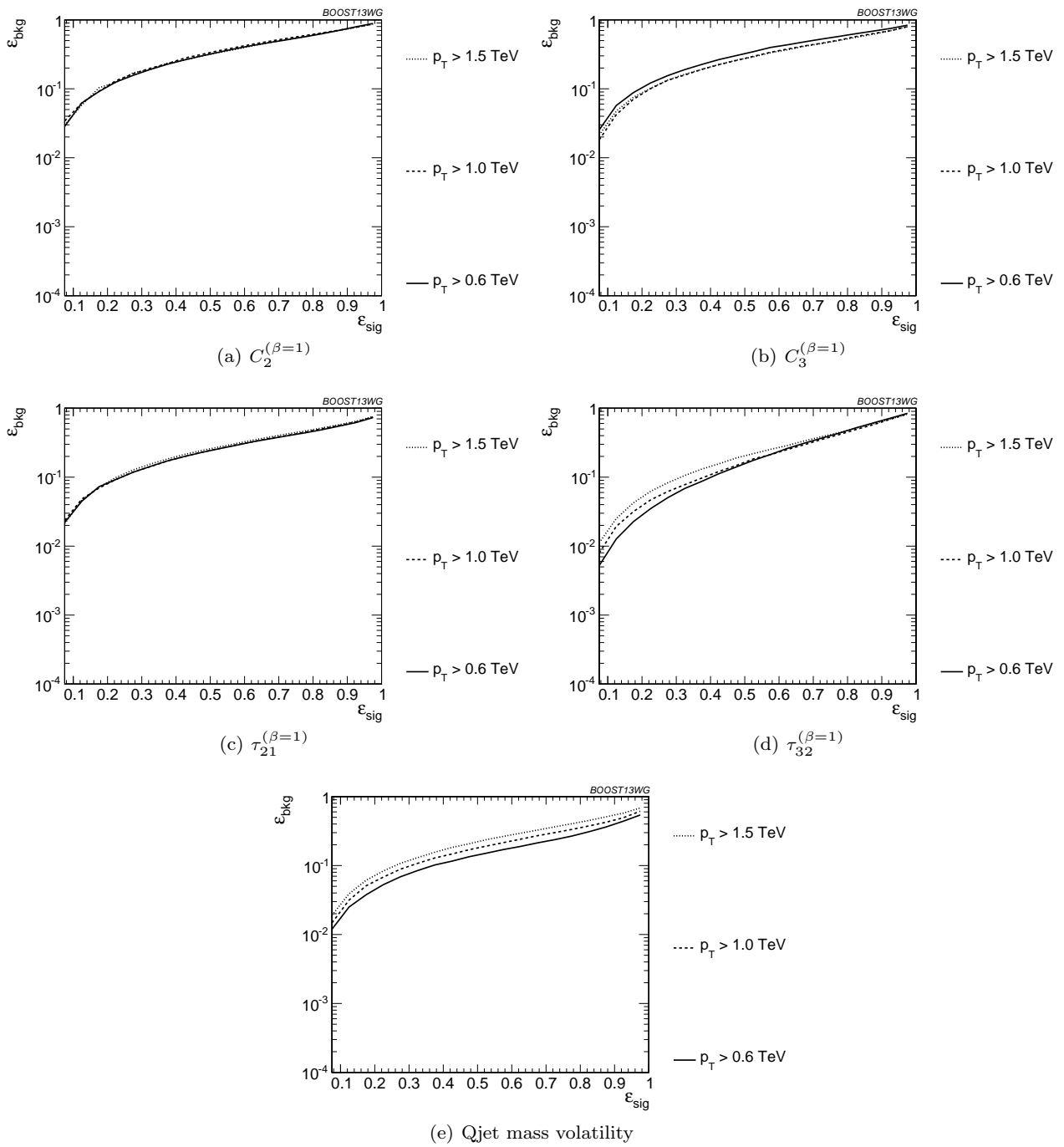


Fig. 28 Comparison of individual jet shape performance at different p_T using the anti- k_T $R=0.8$ algorithm.

977 in Section 7.2. By contrast, the JH tagger outperforms⁹⁸⁵
 978 the other algorithms. To determine whether there is⁹⁸⁶
 979 complementary information in the mass outputs from⁹⁸⁷
 980 different top taggers, we also consider in Figure 37 a⁹⁸⁸
 981 multivariable combination of all of the JH and HEP-⁹⁸⁹
 982 TopTagger outputs. The maximum efficiency of the com-⁹⁹⁰
 983 bined JH and HEPTopTaggers is limited, as some frac-⁹⁹¹
 984 tion of signal events inevitably fails either one or other⁹⁹²

of the taggers. We do see a 20-50% improvement in
 performance when combining all outputs, which sug-
 gests that the different algorithms used to identify the
 top and W for different taggers contains complemen-
 tary information.

In Figure 38 we present the results for multivariable
 combinations of the top tagger outputs with and with-
 out shape variables. We see that, for both the HEP-

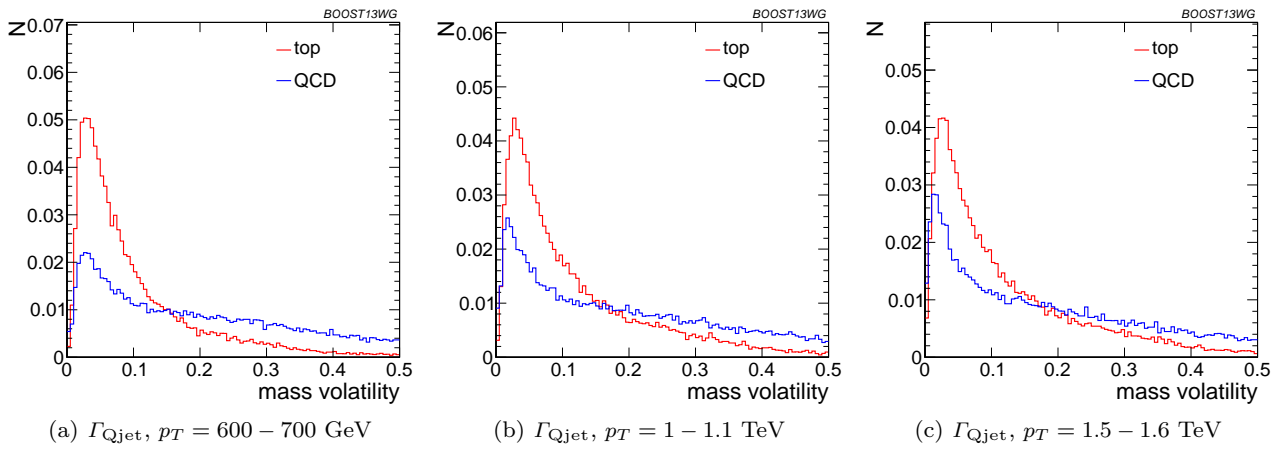


Fig. 29 Comparison of Γ_{Qjet} at $R = 0.8$ and different values of the p_T .

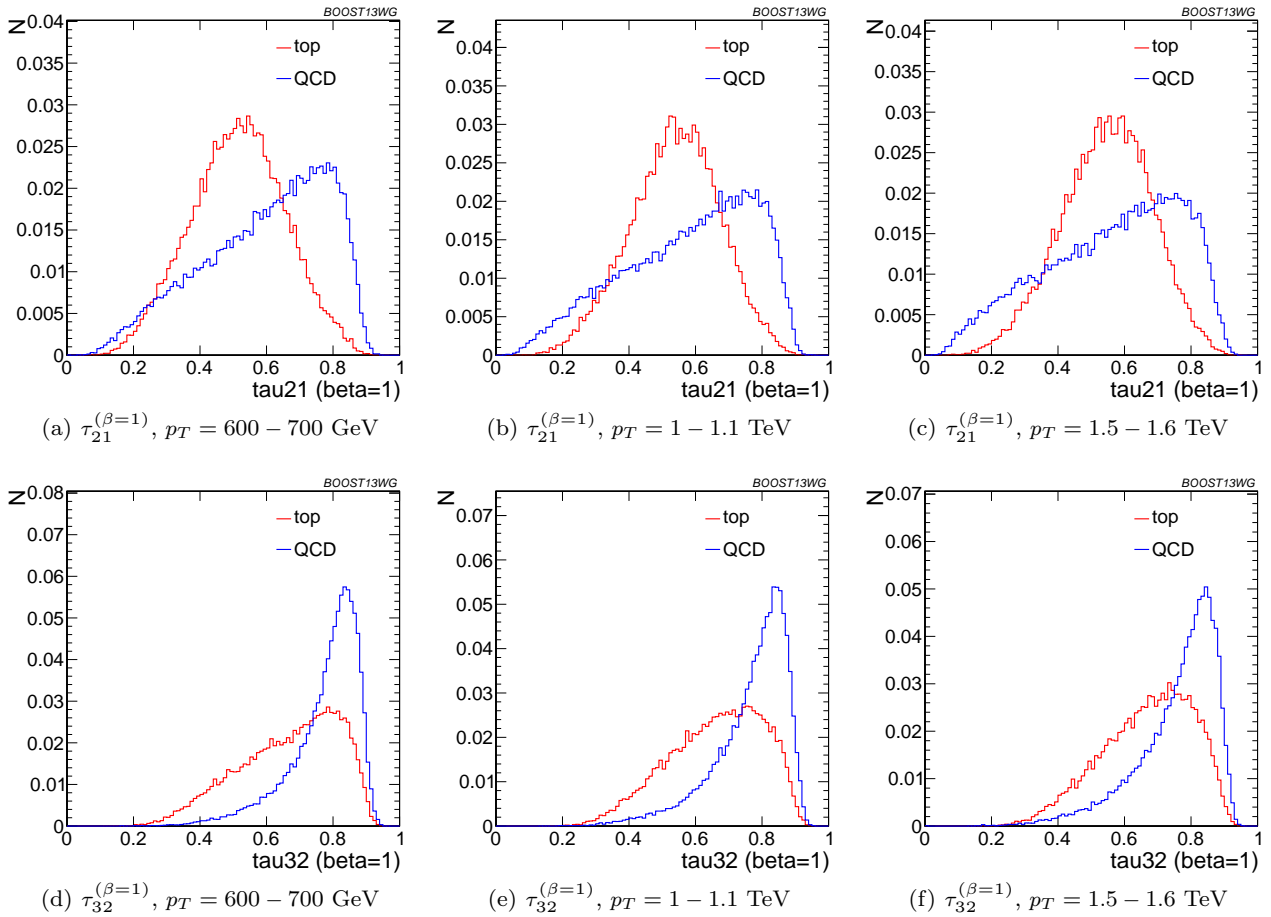


Fig. 30 Comparison of $\tau_{21}^{\beta=1}$ and $\tau_{32}^{\beta=1}$ with $R = 0.8$ and different values of the p_T .

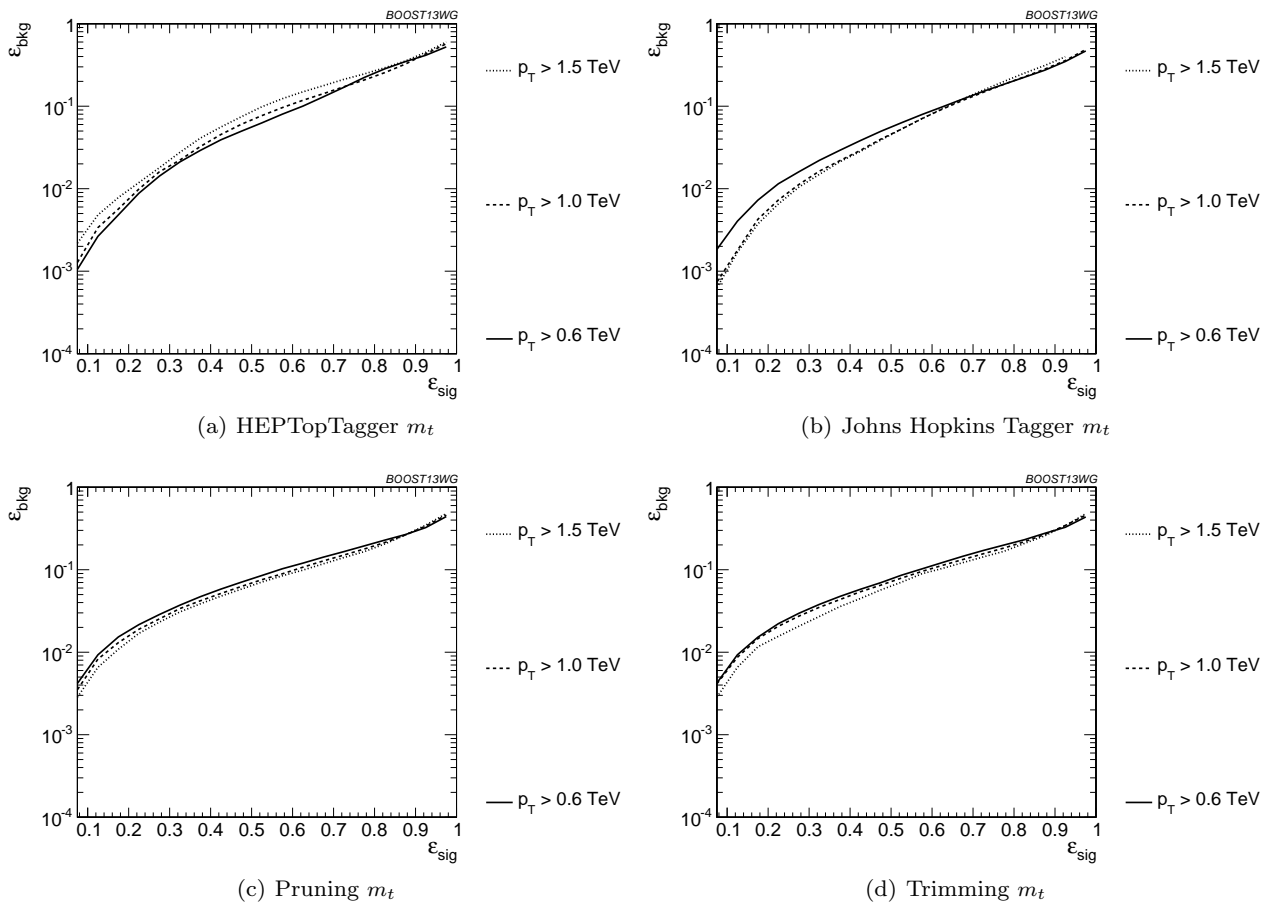


Fig. 31 Comparison of top mass performance of different taggers at different p_T using the anti- k_T $R=0.8$ algorithm.

993 TopTagger and the JH tagger, the shape observables
 994 contain additional information uncorrelated with the
 995 masses and helicity angle, and give on average a fac-
 996 tor 2-3 improvement in signal discrimination. We see
 997 that, when combined with the tagger outputs, both
 998 the energy correlation functions $C_2 + C_3$ and the N
 999 subjettiness ratios $\tau_{21} + \tau_{32}$ give comparable perfor-
 1000 mance, while the Qjet mass volatility is slightly worse
 1001 this is unsurprising, as Qjets accesses shape informa-
 1002 tion in a more indirect way from other shape observ-
 1003 ables. Combining all shape observables with a single top
 1004 tagger provides even greater enhancement in discrimi-
 1005 nation power. We directly compare the performance of
 1006 the JH and HEPTopTaggers in Figure 38(c). Combin-
 1007 ing the taggers with shape information nearly erases
 1008 the difference between the tagging methods observed in
 1009 Figure 37; this indicates that combining the shape in-
 1010 formation with the HEPTopTagger identifies the differ-
 1011 ences between signal and background missed by the tag-
 1012 ger alone. This also suggests that further improvement
 1013 to discriminating power may be minimal, as various

multivariable combinations are converging to within a
 factor of 20% or so.

In Figure 39 we present the results for multivari-
 able combinations of groomer outputs with and without
 shape variables. As with the tagging algorithms, com-
 binations of groomers with shape observables improves
 their discriminating power; combinations with $\tau_{32} + \tau_{21}$
 perform comparably to those with $C_3 + C_2$, and both
 of these are superior to combinations with the mass
 volatility, Γ . Substantial improvement is further possi-
 ble by combining the groomers with all shape observ-
 ables. Not surprisingly, the taggers that lag behind in
 performance enjoy the largest gain in signal-background
 discrimination with the addition of shape observables.
 Once again, in Figure 39(c), we find that the differ-
 ences between pruning and trimming are erased when
 combined with shape information.

Finally, in Figure 40, we compare the performance
 of each of the tagger/groomers when their outputs are
 combined with all of the shape observables considered.
 One can see that the discrepancies between the perfor-
 mance of the different taggers/groomers all but van-

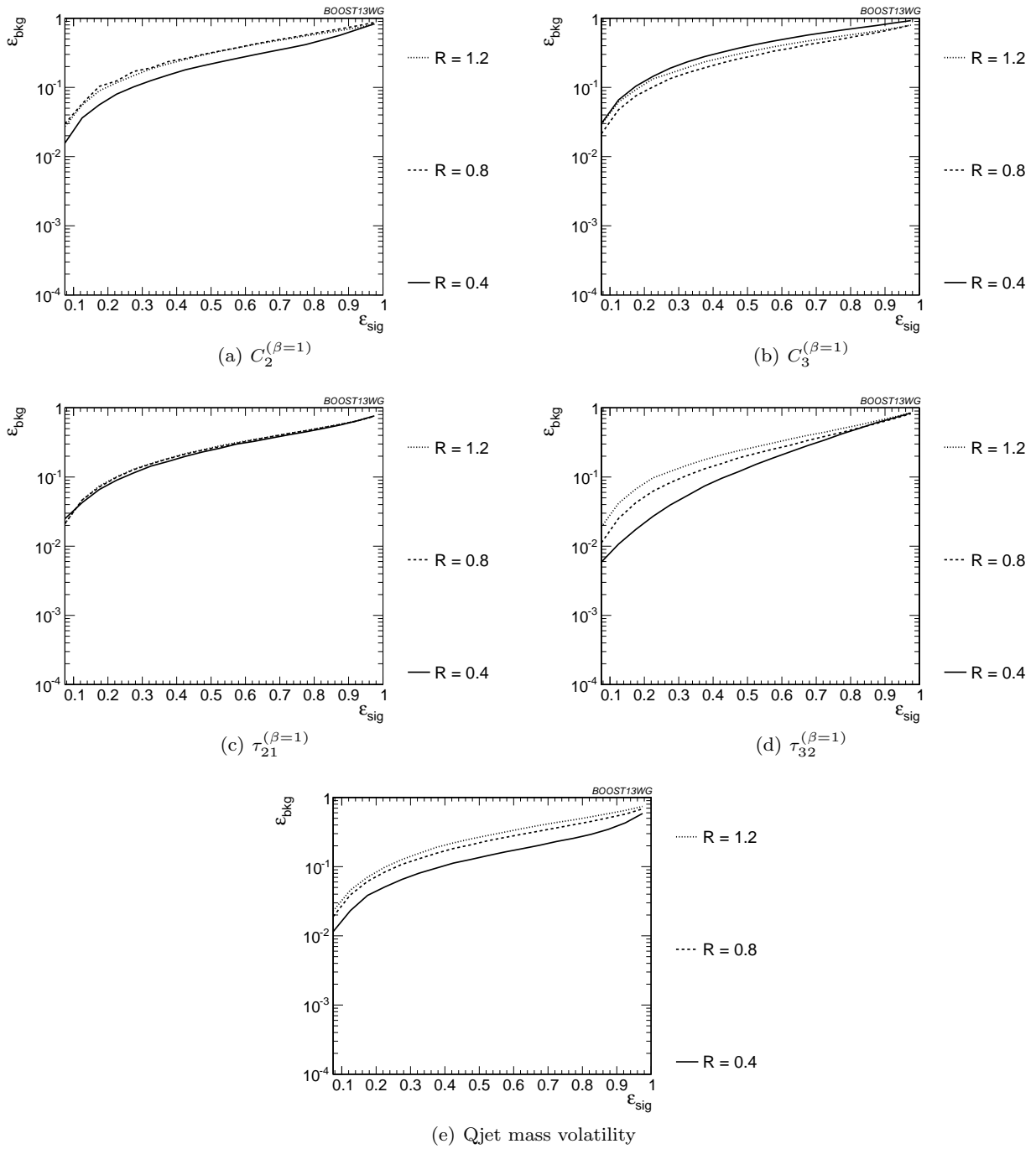


Fig. 32 Comparison of individual jet shape performance at different R in the $p_T = 1.5 - 1.6$ TeV bin.

ishes, suggesting perhaps that we are here utilising all available signal-background discrimination information and that this is the optimal top tagging performance that could be achieved in these conditions.

Up to this point we have just considered the combined binned multivariable performance in the p_T 1.0-1.1 TeV bin with jet radius $R=0.8$. We now compare the BDT combinations of tagger outputs, with and without shape

variables, at different p_T . The taggers are optimized over all input parameters for each choice of p_T and signal efficiency. As with the single-variable study, we consider anti- k_T jets clustered with $R = 0.8$ and compare the outcomes in the $p_T = 500 - 600$ GeV, $p_T = 1 - 1.1$ TeV, and $p_T = 1.5 - 1.6$ TeV bins. The comparison of the taggers/groomers is shown in Figure 41. The behaviour with p_T is qualitatively similar to the behaviour

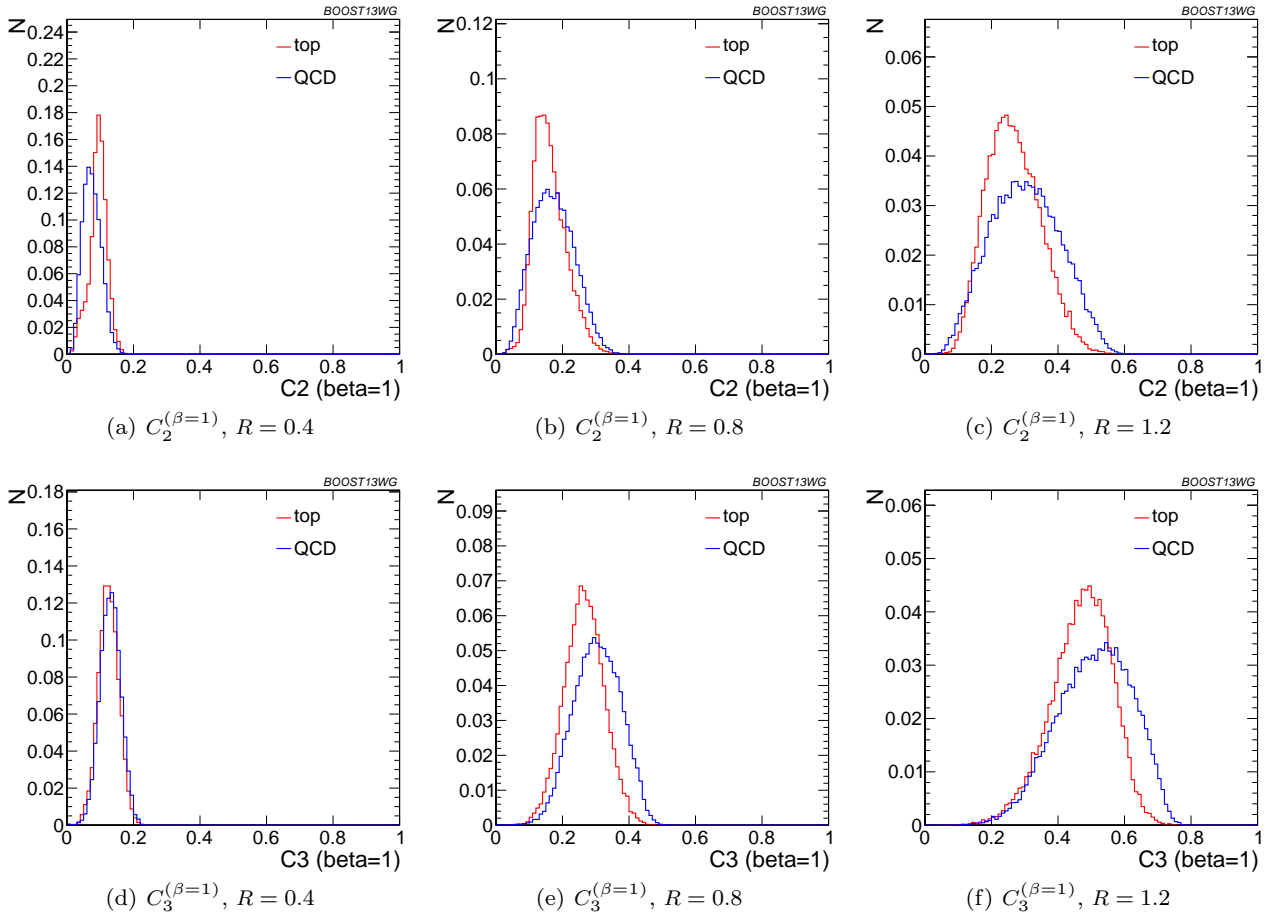


Fig. 33 Comparison of $C_2^{\beta=1}$ and $C_3^{\beta=1}$ in the $p_T = 1.5 - 1.6$ TeV bin and different values of the anti- k_T radius R .

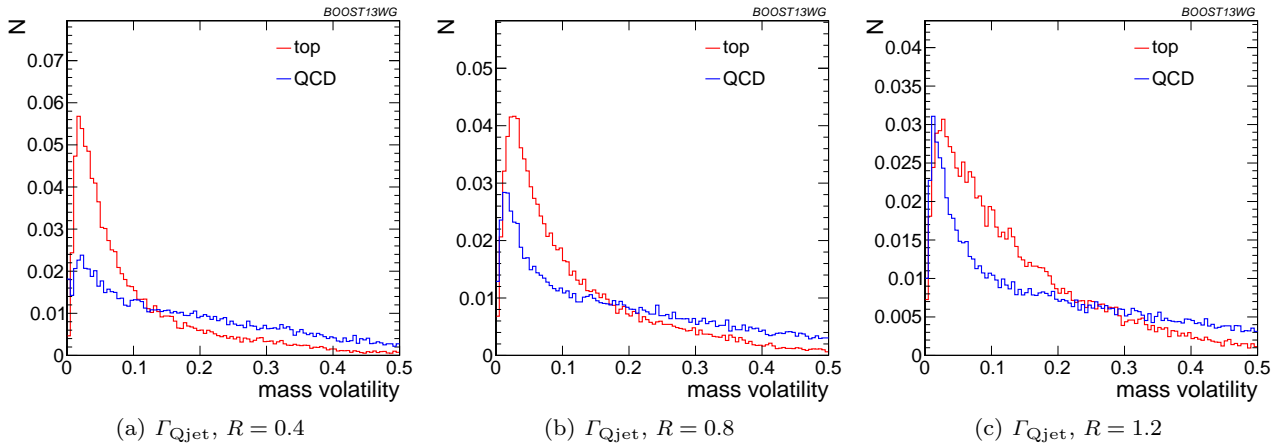


Fig. 34 Comparison of Γ_{Qjet} in the $p_T = 1.5 - 1.6$ TeV bin and different values of the anti- k_T radius R .

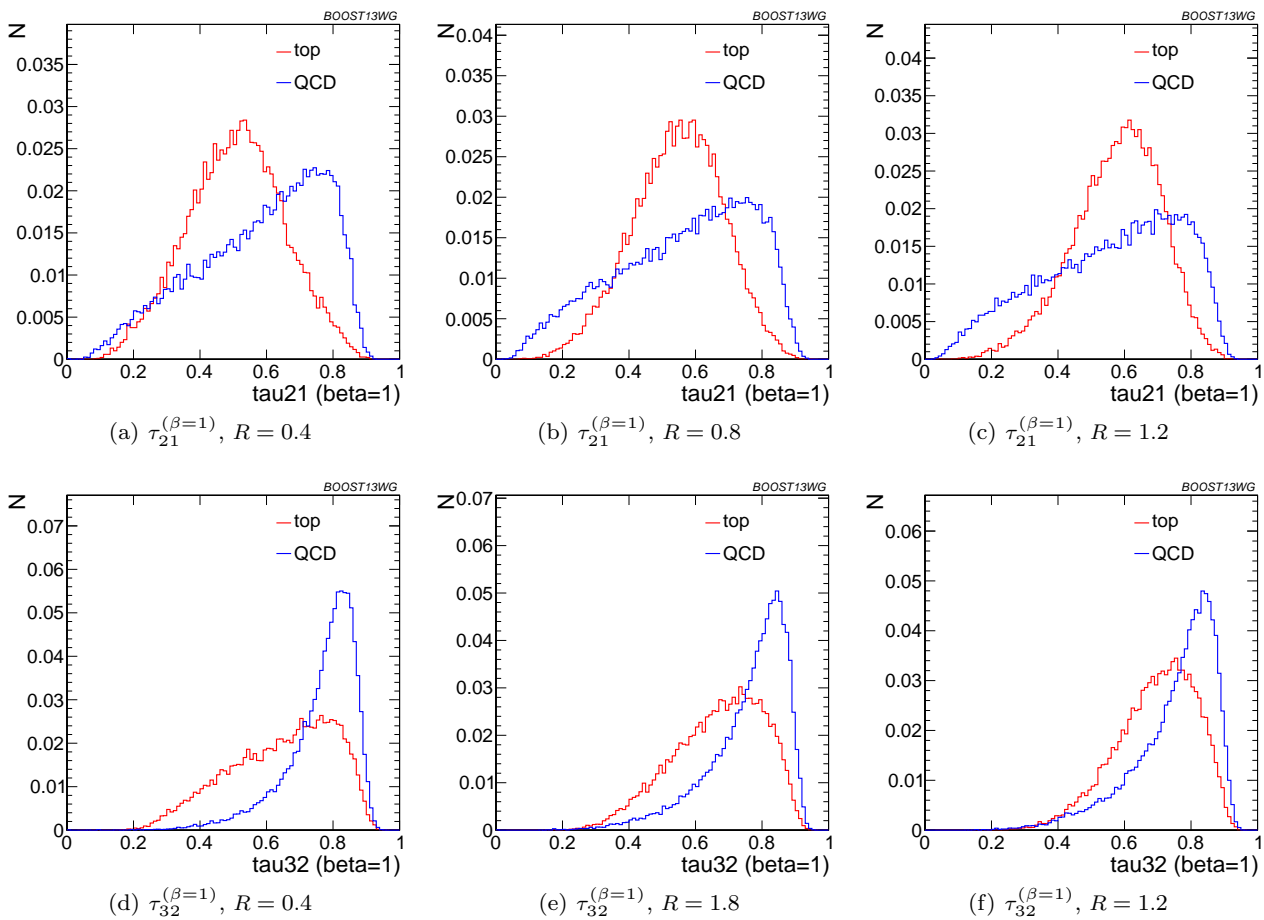


Fig. 35 Comparison of $\tau_{21}^{\beta=1}$ and $\tau_{32}^{\beta=1}$ in the $p_T = 1.5 - 1.6$ TeV bin and different values of the anti- k_T radius R .

1052 of the m_t observable for each tagger/groomer shown in 1073
 1053 Figure 31; this suggests that the p_T behaviour of the 1074
 1054 taggers is dominated by the top mass reconstruction 1075
 1055 As before, the HEPTopTagger performance degrades 1076
 1056 slightly with increased p_T due to the background shap-
 1057 ing effect, while the JH tagger and groomers modestly
 1058 improve in performance. 1077

1059 In Figure 42, we show the p_T dependence of BDT 1078
 1060 combinations of the JH tagger output combined with 1079
 1061 shape observables. We find that the curves look nearly 1080
 1062 identical: the p_T dependence is dominated by the top 1081
 1063 mass reconstruction, and combining the tagger outputs 1082
 1064 with different shape observables does not substantially 1083
 1065 change this behaviour. The same holds true for trim 1084
 1066 and pruning. By contrast, HEPTopTagger ROG 1085
 1067 curves, shown in Figure 43, do change somewhat when 1086
 1068 combined with different shape observables; due to the 1087
 1069 suboptimal performance of the HEPTopTagger at high 1088
 1070 p_T , we find that combining the HEPTopTagger with 1089
 1071 $C_3^{(\beta=1)}$, which in Figure 28(b) is seen to have some mod- 1090
 1072 est improvement at high p_T , can improve its perfor- 1091
 1092

1093 mance. Combining the HEPTopTagger with multiple
 1094 shape observables gives the maximum improvement in
 1095 performance at high p_T relative to at low p_T .

1096 In Figure 44 we compare the BDT combinations
 1097 of tagger outputs, with and without shape variables, at
 1098 different jet radius R in the $p_T = 1.5 - 1.6$ TeV bin.
 1099 The taggers are optimized over all input parameters
 1100 for each choice of R and signal efficiency. We find that,
 1101 for all taggers and groomers, the performance is always
 1102 best at small R ; the choice of R is sufficiently large to
 1103 admit the full top quark decay at such high p_T , but
 1104 is small enough to suppress contamination from addi-
 1105 tional radiation. This is not altered when the taggers
 1106 are combined with shape observable. For example, in
 1107 Figure 45 is shown the dependence on R of the JH tag-
 1108 ger when combined with shape observables, where one
 1109 can see that the R -dependence is identical for all com-
 1110 binations. The same holds true for the HEPTopTagger,
 1111 trimming, and pruning.

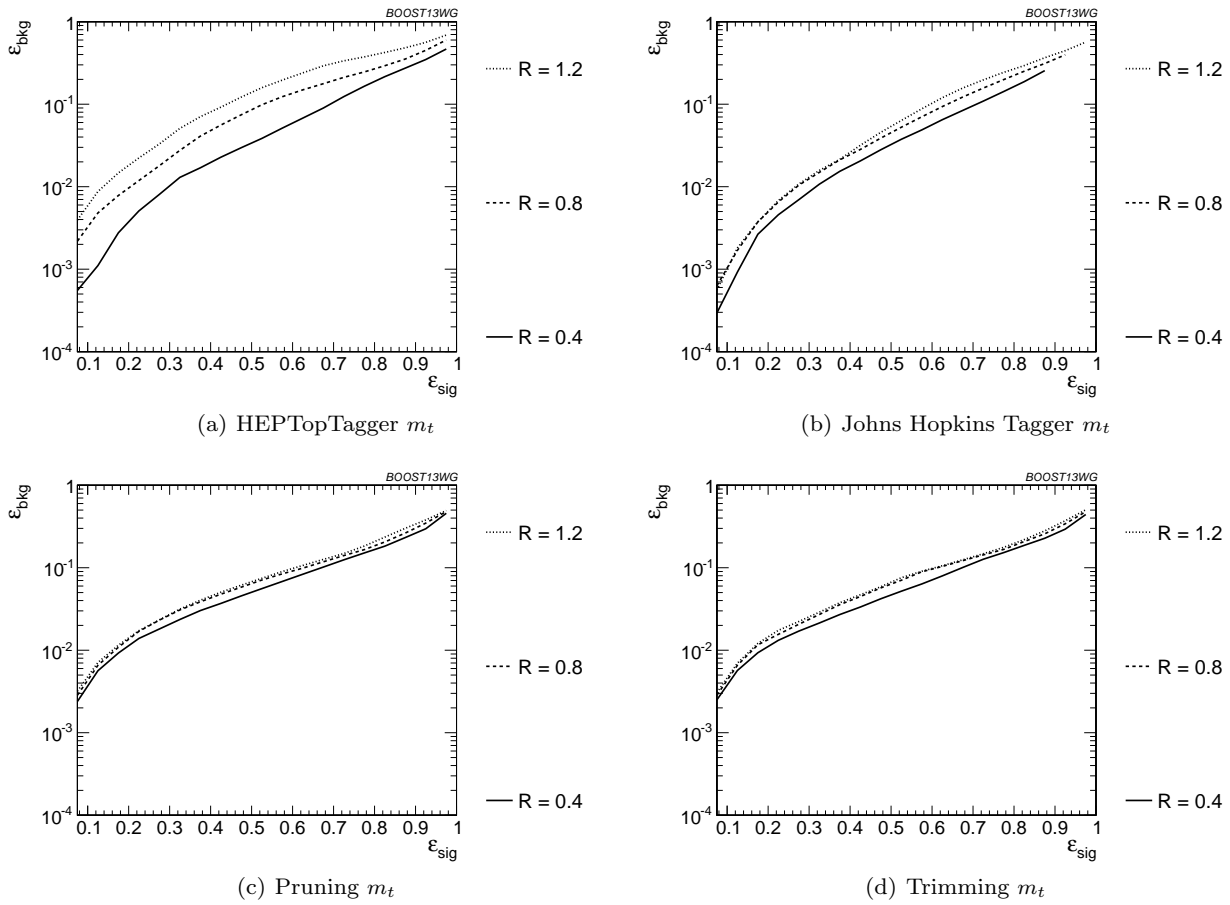


Fig. 36 Comparison of top mass performance of different taggers at different R in the $p_T = 1.5 - 1.6$ TeV bin.

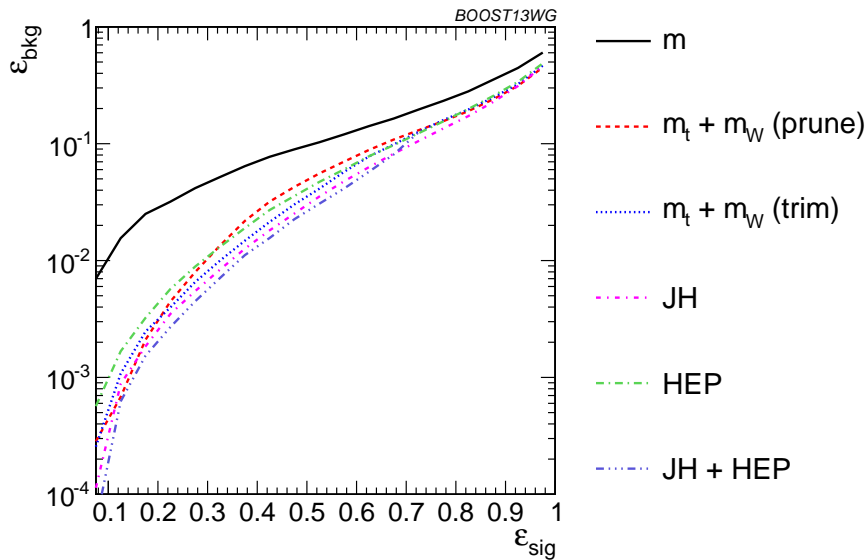


Fig. 37 The performance of the various taggers in the $p_T = 1 - 1.1$ TeV bin using the anti- k_T $R=0.8$ algorithm. For the groomers a BDT combination of the reconstructed m_t and m_W are used. Also shown is a multivariable combination of all of the JH and HEPTopTagger outputs. The ungroomed mass performance is shown for comparison.

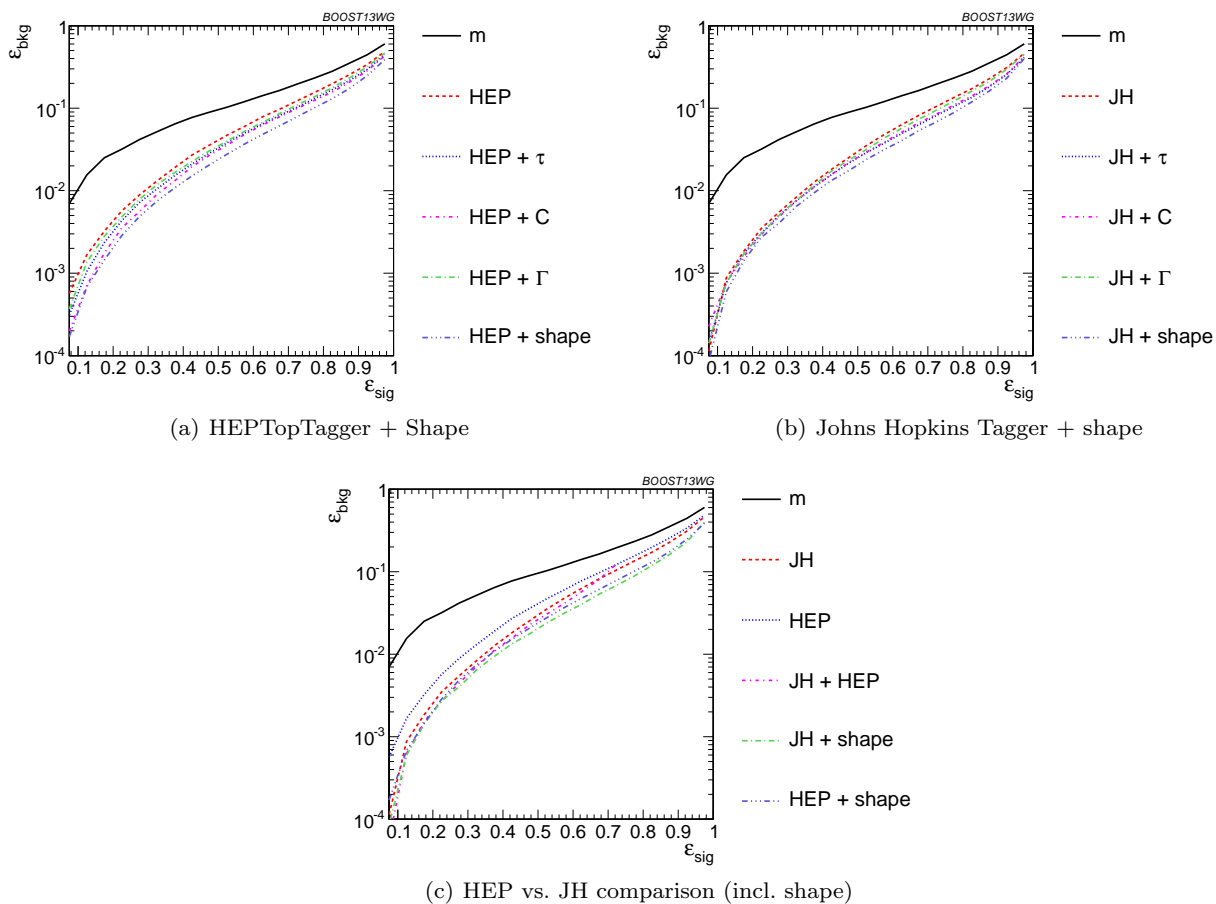


Fig. 38 The performance of BDT combinations of the JH and HepTopTagger outputs with various shape observables in the $p_T = 1 - 1.1$ TeV bin using the anti- k_T $R=0.8$ algorithm. Taggers are combined with the following shape observables: $\tau_{21}^{(\beta=1)} + \tau_{32}^{(\beta=1)}$, $C_2^{(\beta=1)} + C_3^{(\beta=1)}$, Γ_{Qjet} , and all of the above (denoted “shape”).

1093 7.4 Performance at Sub-Optimal Working Points

1094 Up until now, we have re-optimized our tagger and
 1095 groomer parameters for each p_T , R , and signal efficiency
 1096 working point. In reality, experiments will choose a fi
 1097 nite set of working points to use. How do our results
 1098 hold up when this is taken into account? To address this
 1099 concern, we replicate our analyses, but only optimize
 1100 the top taggers for a particular p_T/R /efficiency and ap
 1101 ply the same parameters to other scenarios. This allows
 1102 us to determine the extent to which re-optimization is
 1103 necessary to maintain the high signal-background dis
 1104 crimination power seen in the top tagging algorithms
 1105 we study. The shape observables typically do not have
 1106 any input parameters to optimize. Therefore, we focus
 1107 on the taggers and groomers, and their combination
 1108 with shape observables, in this section.

1109 **Optimizing at a single p_T** : We show in Figure 46
 1110 the performance of the top taggers, using just the recon
 1111 structed top mass as the discriminating variable, with

1112 all input parameters optimized to the $p_T = 1.5 - 1.6$
 1113 TeV bin, relative to the performance optimized at each
 1114 p_T . We see that while the performance degrades by
 1115 about 50% when the high- p_T optimized points are used
 1116 at other momenta, this is only an $O(1)$ adjustment of
 1117 the tagger performance **ED: what does $O(1)$ mean?**,
 1118 with trimming and the Johns Hopkins tagger degrad
 1119 ing the most. The jagged behaviour of the points is due
 1120 to the finite resolution of the scan. We also observe a
 1121 particular effect associated with using suboptimal tag
 1122 gers: since taggers sometimes fail to return a top cand
 1123 idate, parameters optimized for a particular efficiency
 1124 ε_S at $p_T = 1.5 - 1.6$ TeV may not return enough sig
 1125 nal candidates to reach the same efficiency at a different
 1126 p_T . Consequently, no point appears for that p_T value.
 1127 This is not often a practical concern, as the largest gains
 1128 in signal discrimination and significance are for smaller
 1129 values of ε_S , but it is something that must be consid
 1130 ered when selecting benchmark tagger parameters and
 1131 signal efficiencies.

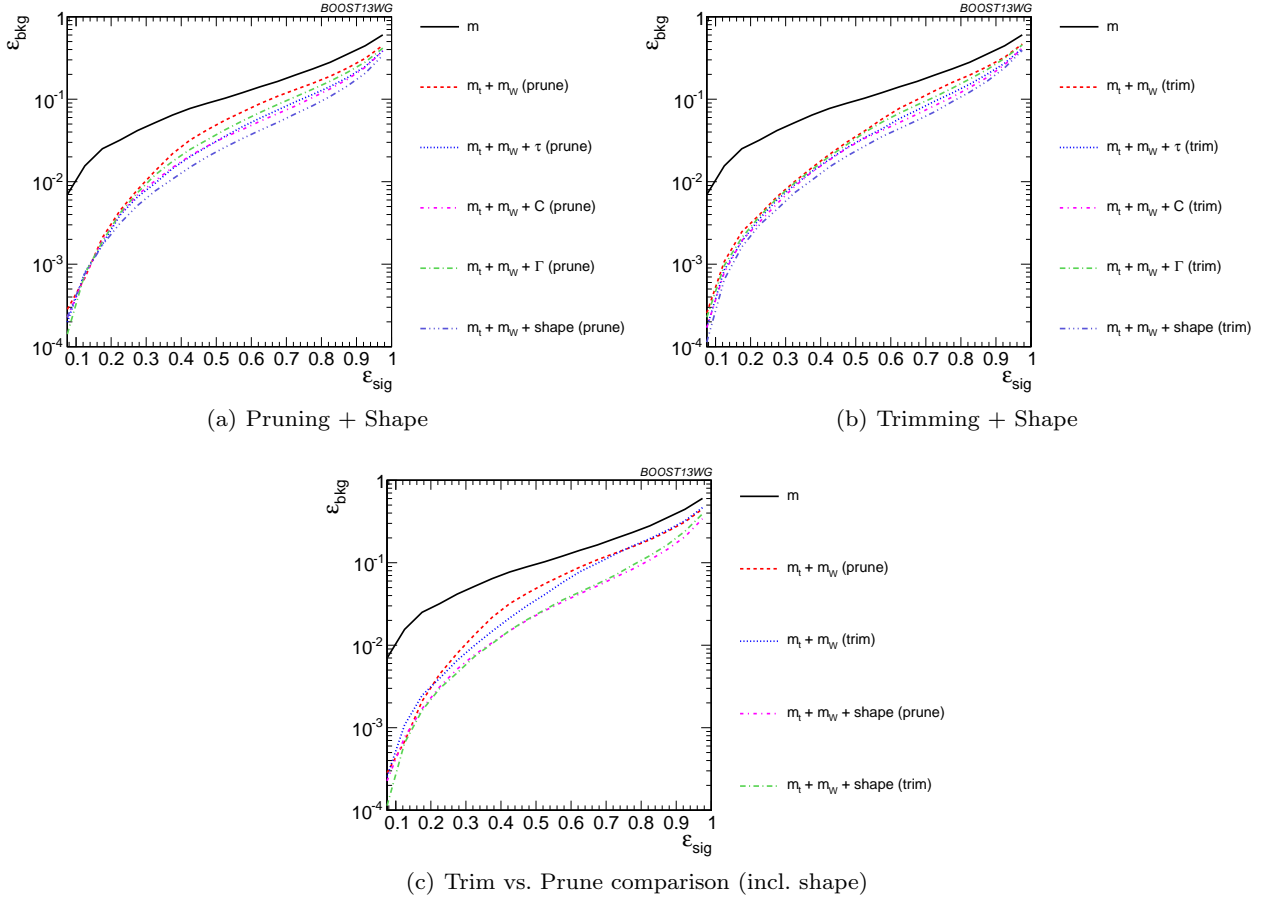


Fig. 39 The performance of the BDT combinations of the trimming and pruning outputs with various shape observables in the $p_T = 1 - 1.1$ TeV bin using the anti- k_T $R=0.8$ algorithm. Groomer mass outputs are combined with the following shape observables: $\tau_{21}^{(\beta=1)} + \tau_{32}^{(\beta=1)}$, $C_2^{(\beta=1)} + C_3^{(\beta=1)}$, Γ_{Qjet} , and all of the above (denoted “shape”).

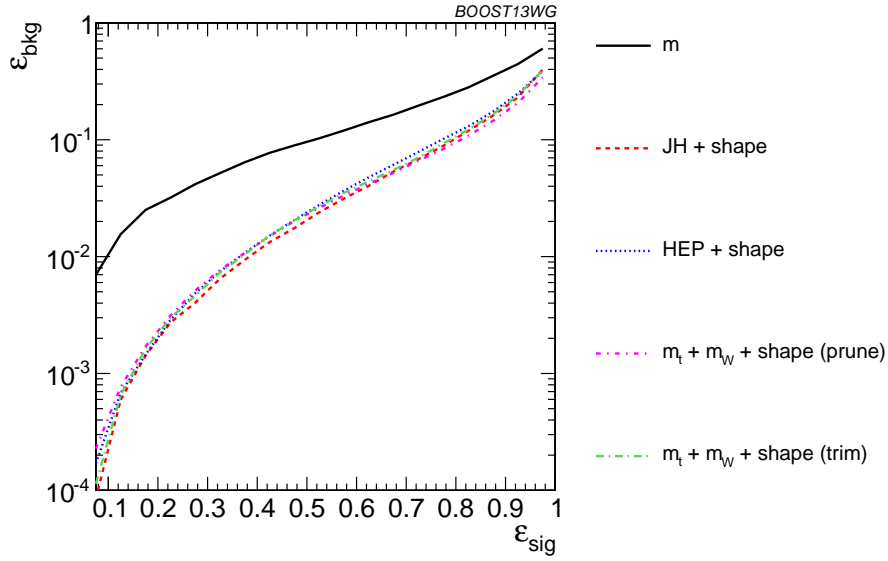


Fig. 40 Comparison of the performance of the BDT combinations of all the groomer/tagger outputs with all the available shape observables in the $p_T = 1 - 1.1$ TeV bin using the anti- k_T $R=0.8$ algorithm. Tagger/groomer outputs are combined with all of the following shape observables: $\tau_{21}^{(\beta=1)} + \tau_{32}^{(\beta=1)}$, $C_2^{(\beta=1)} + C_3^{(\beta=1)}$, Γ_{Qjet} .

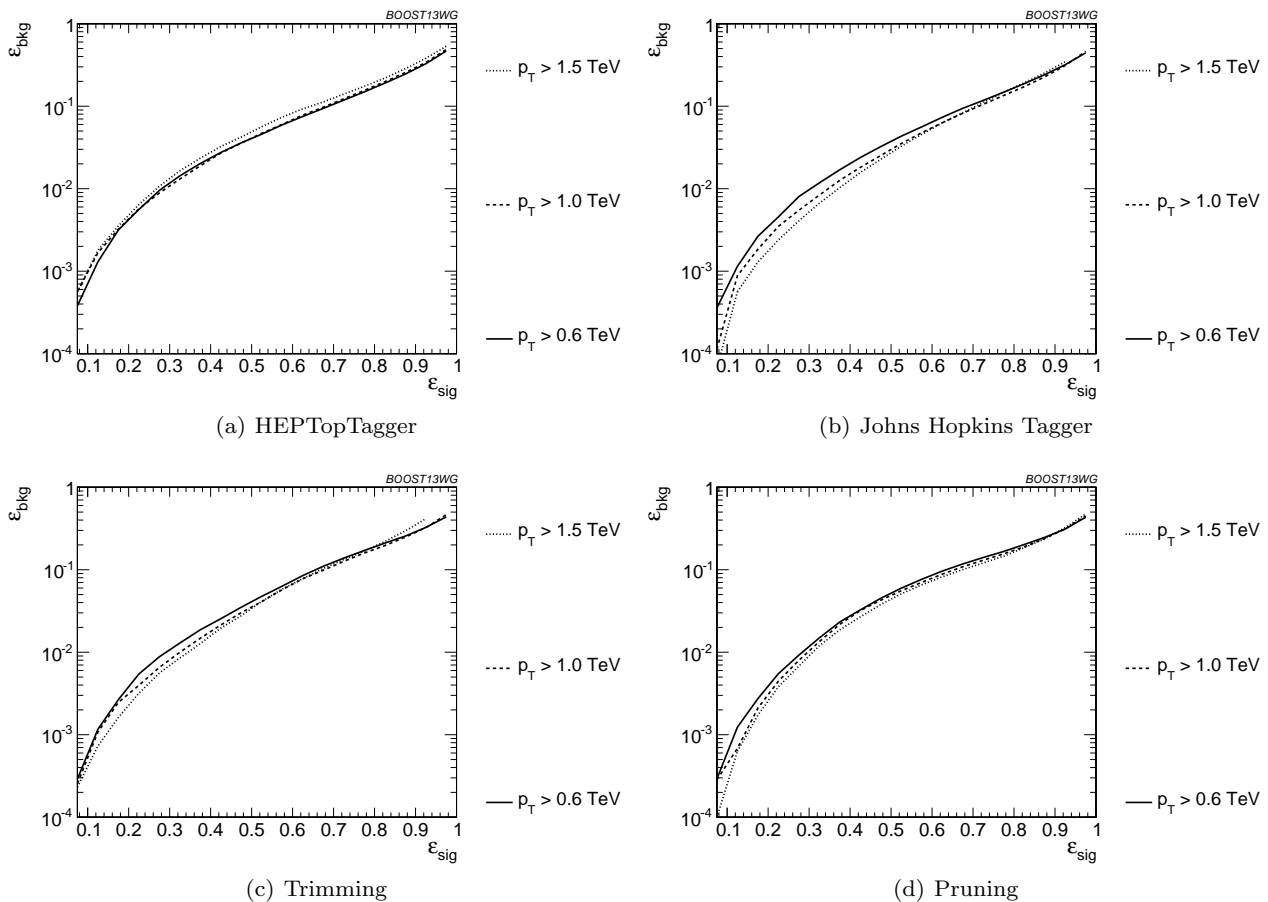


Fig. 41 Comparison of BDT combination of tagger performance at different p_T using the anti- k_T $R=0.8$ algorithm.

1132 The degradation in performance is more pronounced 1154
 1133 for the BDT combinations of the full tagger outputs, 1155
 1134 shown in Figure 47), particularly at very low signal effi- 1156
 1135 ciency where the optimization picks out a cut on the tail 1157
 1136 of some distribution that depends precisely on the p_T/R 1158
 1137 of the jet. Once again, trimming and the Johns Hop- 1159
 1138 kins tagger degrade more markedly. Similar behaviour 1160
 1139 holds for the BDT combinations of tagger outputs plus 1161
 1140 all shape observables. 1162

1141
 1142 **Optimizing at a single R :** We perform a similar anal- 1164
 1143 ysis, optimizing tagger parameters for each signal ef- 1165
 1144 ficiency at $R = 1.2$, and then use the same parame- 1166
 1145 ters for smaller R , in the p_T 1.5-1.6 TeV bin. In Fig- 1167
 1146 ure 48 we show the ratio of the performance of the 1168
 1147 top taggers, using just the reconstructed top mass as 1169
 1148 the discriminating variable, with all input parameters 1170
 1149 optimized to the $R = 1.2$ values compared to input 1171
 1150 parameters optimized separately at each radius. While 1172
 1151 the performance of each observable degrades at small 1173
 1152 ϵ_{sig} compared to the optimized search, the HEP Top- 1174
 1153 Tagger fares the worst as the observed is quite sensitive 1175

to the selected value of R . It is not surprising that a
 tagger whose top mass reconstruction is susceptible to
 background-shaping at large R and p_T would require a
 more careful optimization of parameters to obtain the
 best performance.

The same holds true for the BDT combinations of
 the full tagger outputs, shown in Figure 49). The perfor-
 mance for the sub-optimal taggers is still within an $O(1)$
 factor of the optimized performance, and the HEP Top-
 Tagger performs better with the combination of all of
 its outputs relative to the performance with just m_t .
 The same behaviour holds for the BDT combinations
 of tagger outputs and shape observables.

Optimizing at a single efficiency: The strongest as-
 sumption we have made so far is that the taggers can
 be reoptimized for each signal efficiency point. This is
 useful for making a direct comparison of the power of
 different top tagging algorithms, but is not particularly
 practical for the LHC analyses. We now consider the
 effects when the tagger inputs are optimized once, in
 the $\epsilon_S = 0.3 - 0.35$ bin, and then used to determine the

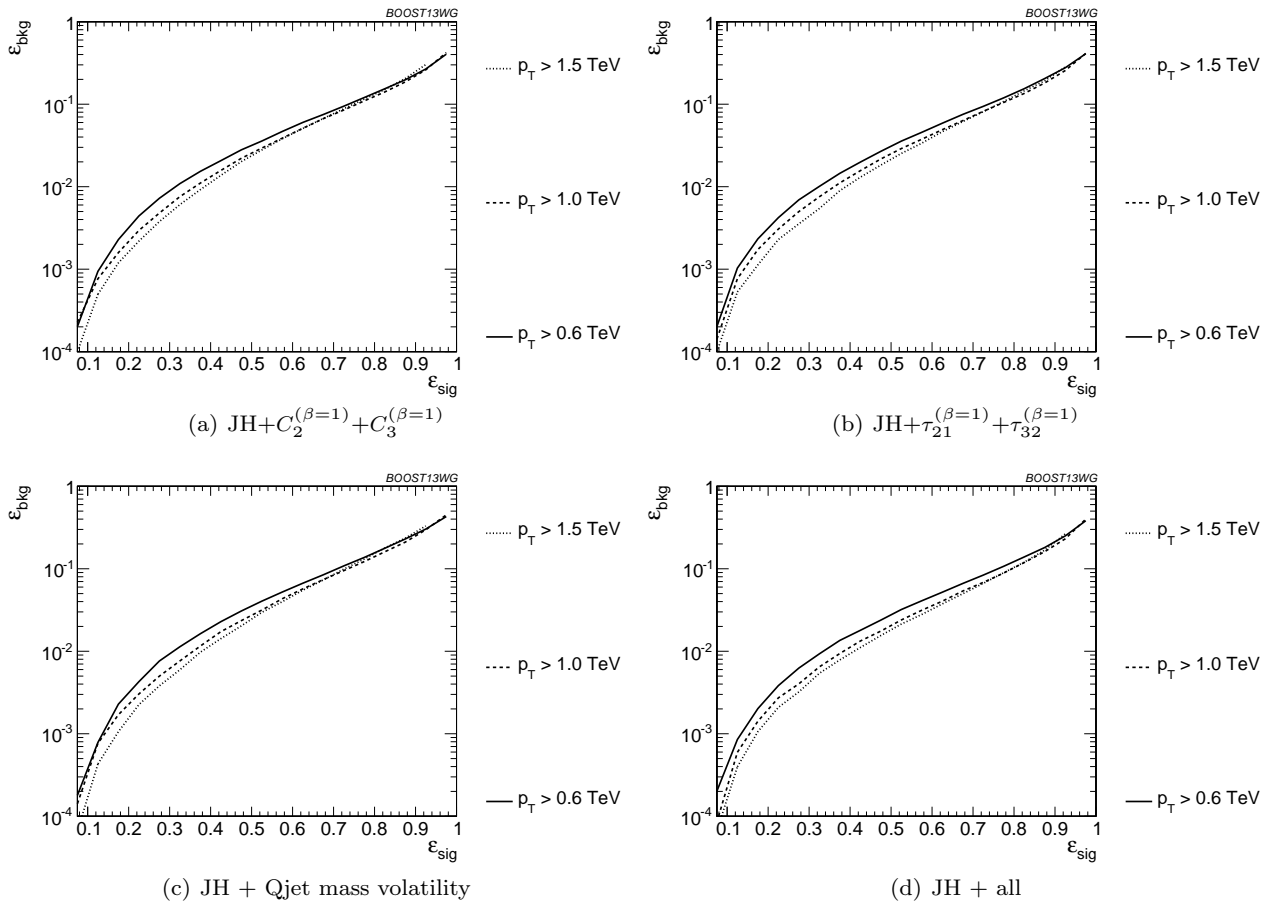


Fig. 42 Comparison of BDT combination of JH tagger + shape at different p_T using the anti- k_T $R=0.8$ algorithm.

1176 full ROC curve. We do this in the p_T 1 – 1.1 TeV bin₁₉₄ 7.5 Conclusions
 1177 and with $R = 0.8$.

1195 **ED: Conclusions to be added**

1178 The performance of each tagger, normalized to its
 1179 performance optimized in each bin, is shown in Figure
 1180 50 for cuts on the top mass and W mass, and in
 1181 Figure 51 for BDT combinations of tagger outputs and
 1182 shape variables. In both plots, it is apparent that opti-
 1183 mizing the taggers in the 0.3-0.35 efficiency bin gives
 1184 comparable performance over efficiencies ranging from
 1185 0.2-0.5, although performance degrades at small and
 1186 large signal efficiencies. Pruning appears to give espe-
 1187 cially robust signal-background discrimination without
 1188 re-optimization, possibly due to the fact that there are
 1189 no absolute distance or p_T scales that appear in the
 1190 algorithm. Figures 50 and 51 suggest that, while opti-
 1191 mization at all signal efficiencies is a useful tool for com-
 1192 paring different algorithms, it is not crucial to achieve
 1193 good top-tagging performance in experiments.

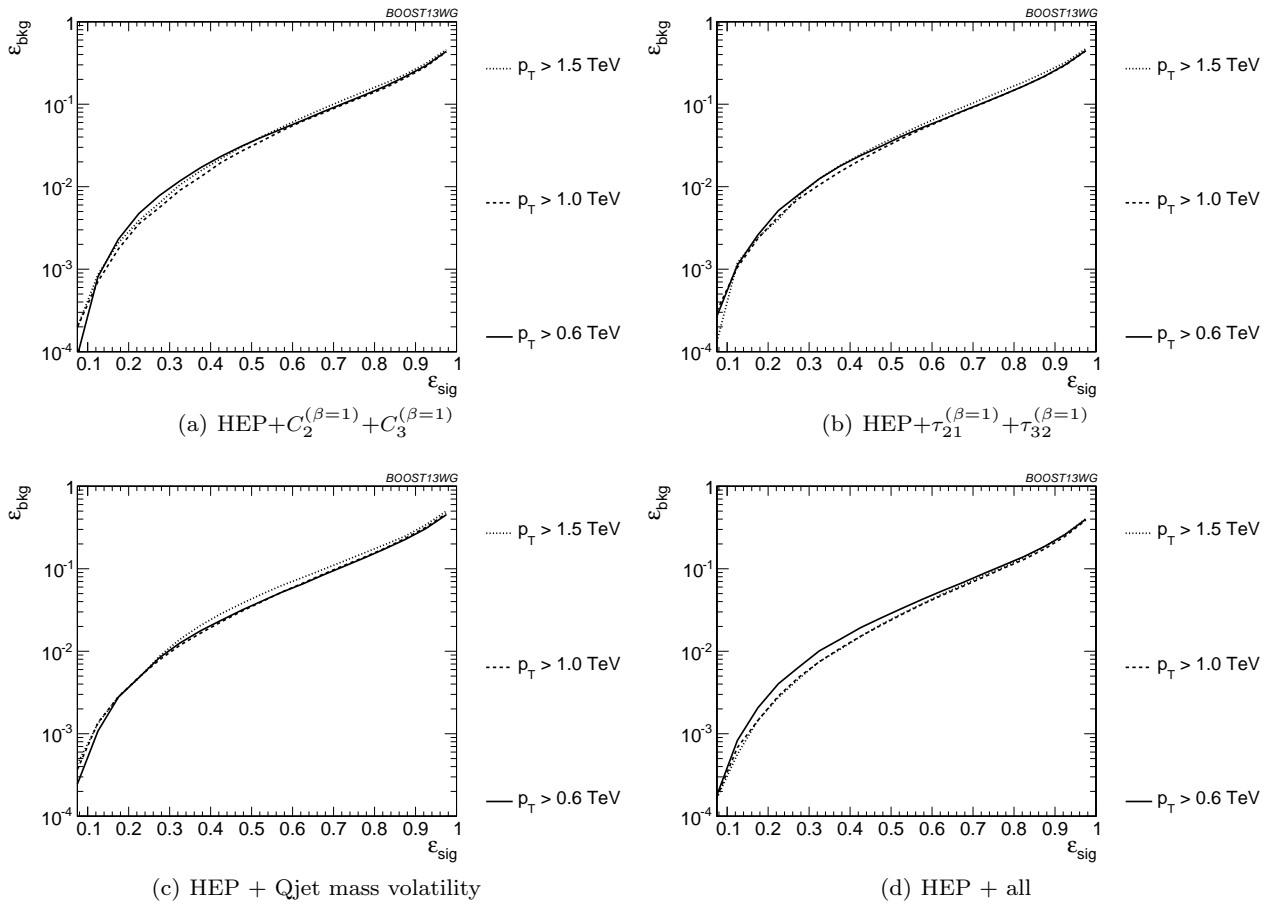


Fig. 43 Comparison of BDT combination of HEP tagger + shape at different p_T using the anti- k_T $R=0.8$ algorithm.

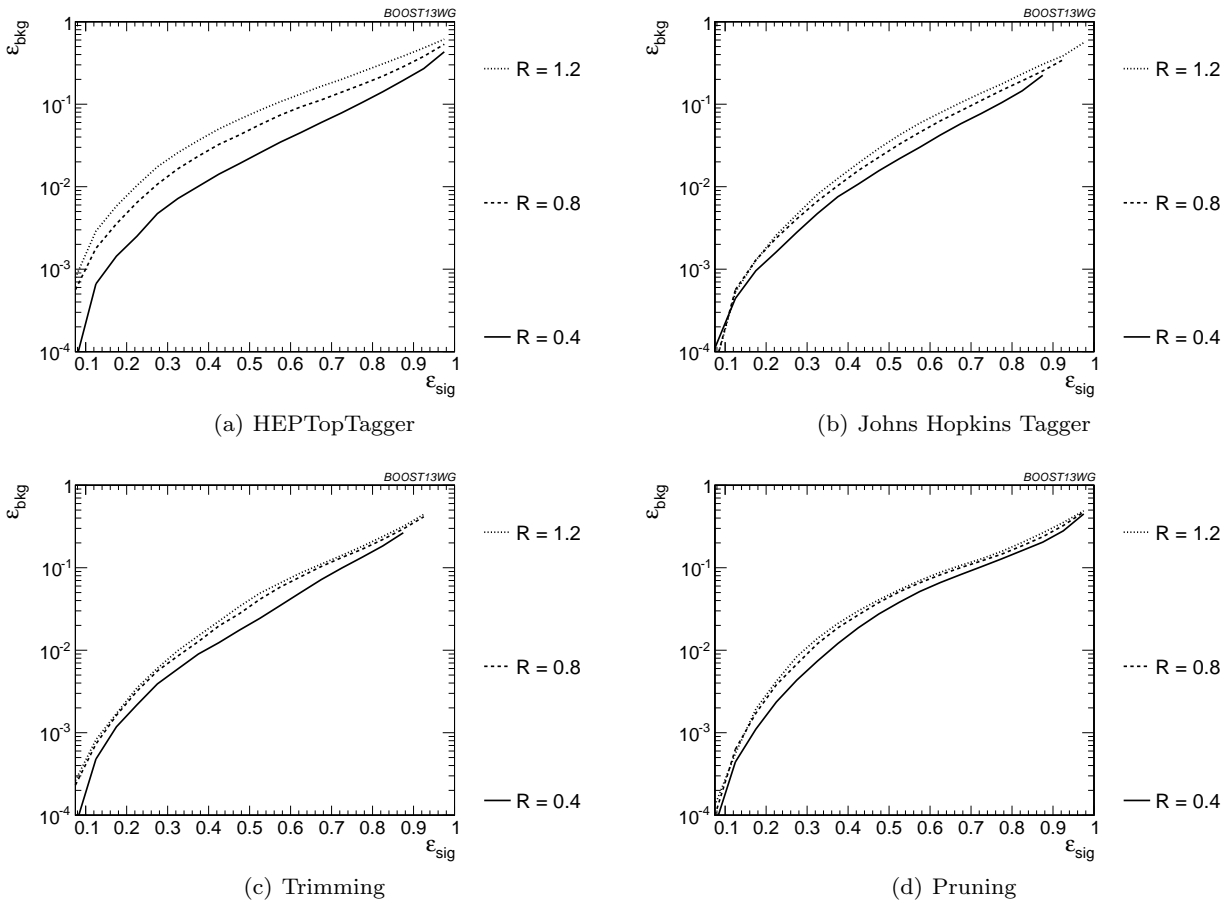


Fig. 44 Comparison of tagger and jet shape performance at different radius at $p_T = 1.5-1.6$ TeV.

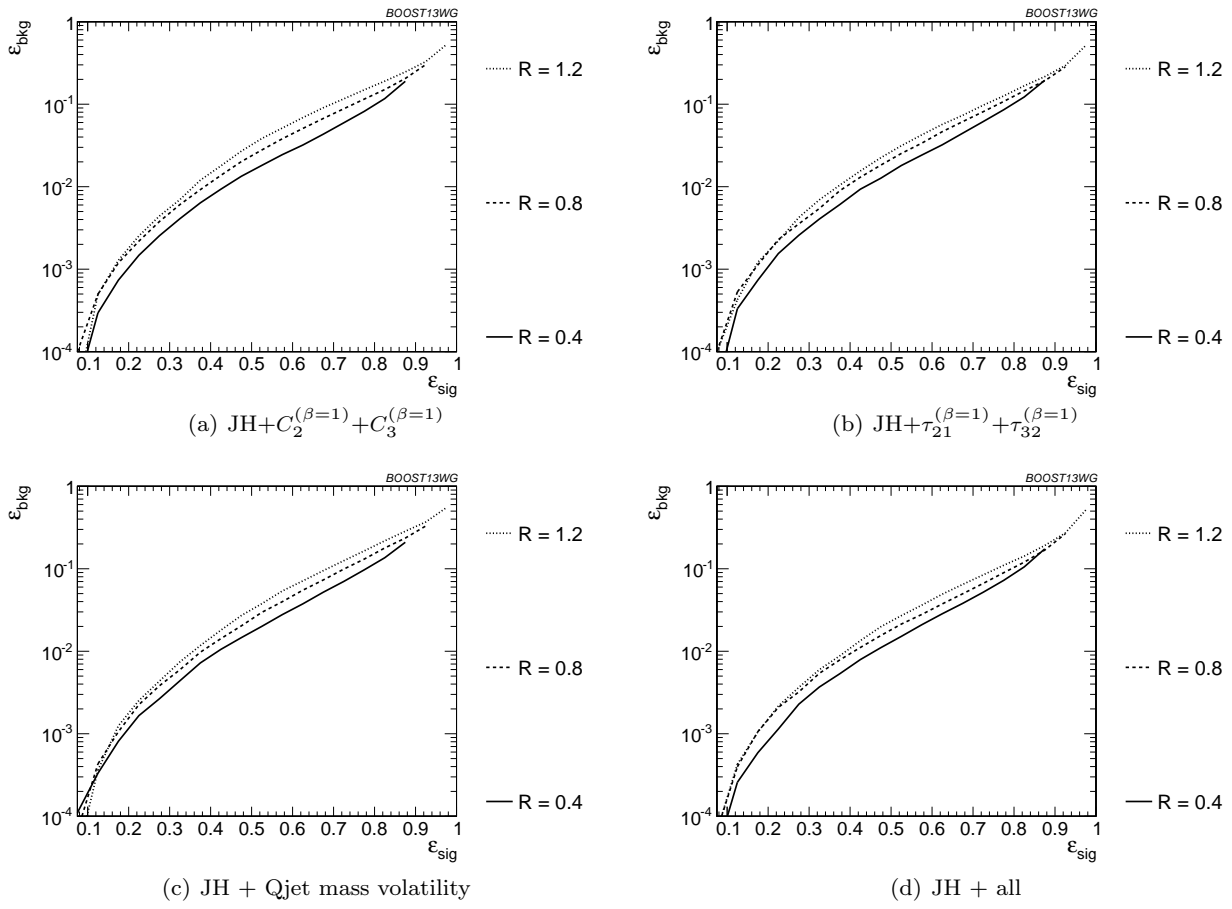


Fig. 45 Comparison of BDT combination of JH tagger + shape at different radius at $p_T = 1.5\text{-}1.6$ TeV.

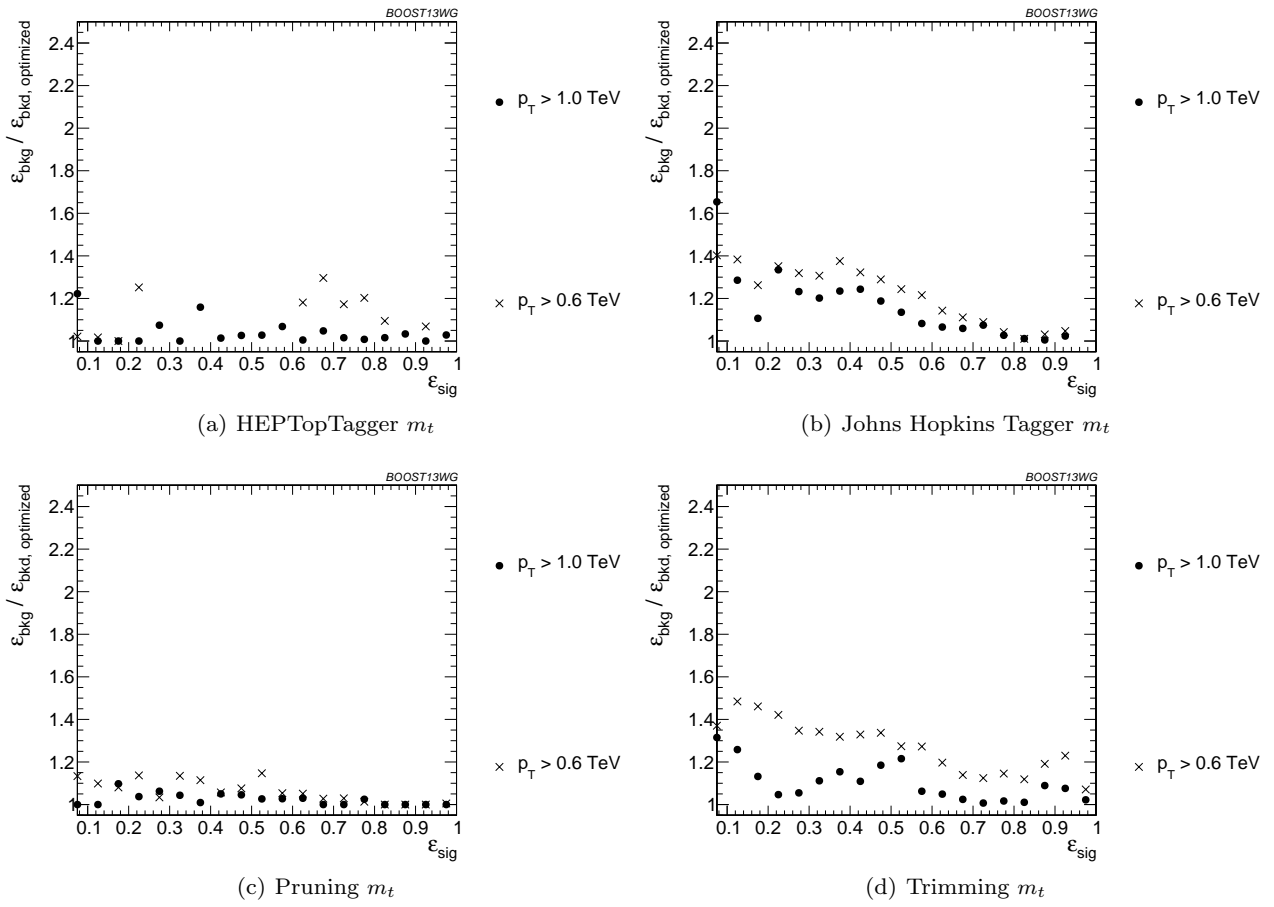


Fig. 46 Comparison of top mass performance of different taggers at different p_T using the anti- k_T $R=0.8$ algorithm; the tagger inputs are set to the optimum value for $p_T = 1.5 - 1.6$ TeV.

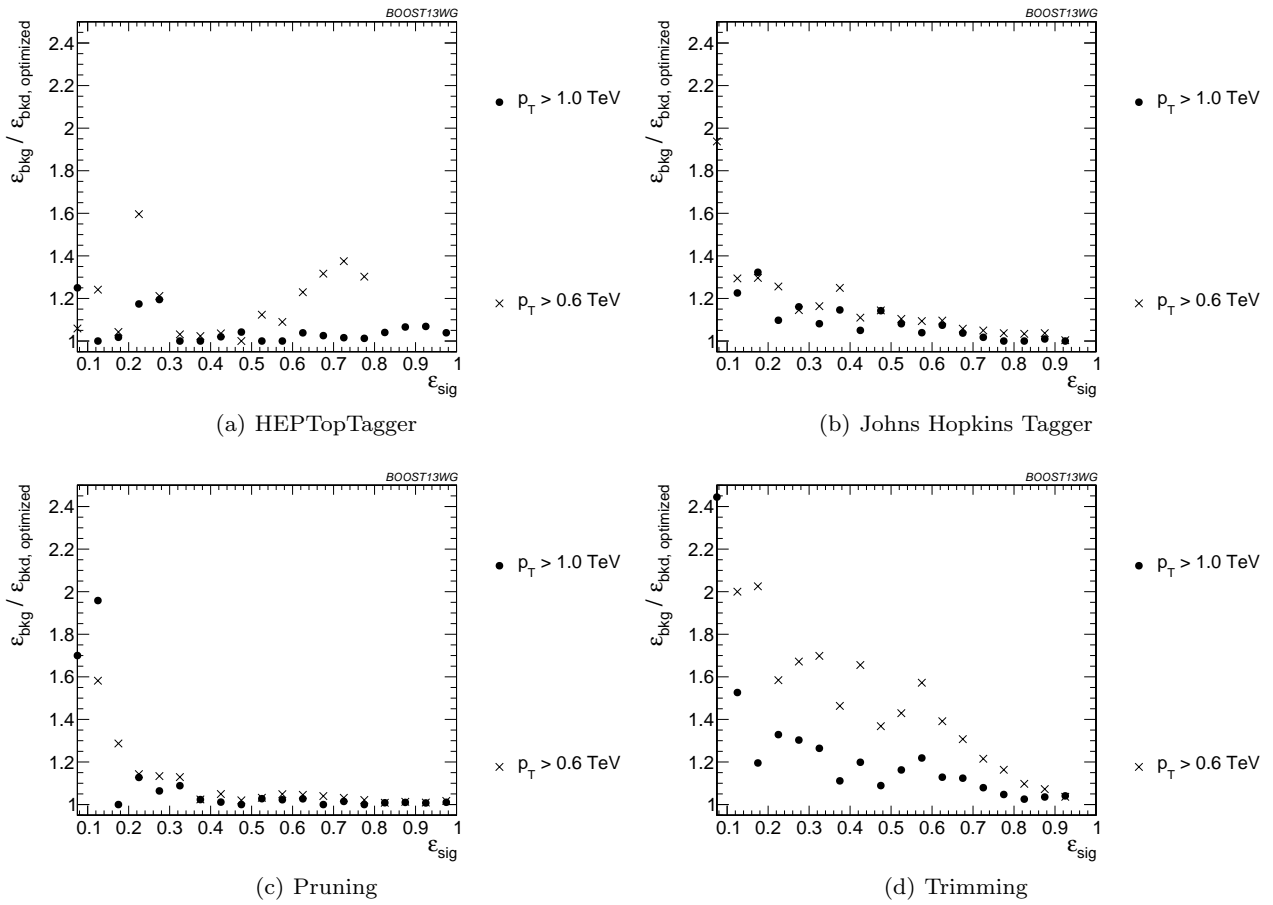


Fig. 47 Comparison of BDT combination of tagger performance at different p_T using the anti- k_T $R=0.8$ algorithm; the tagger inputs are set to the optimum value for $p_T = 1.5 - 1.6$ TeV.

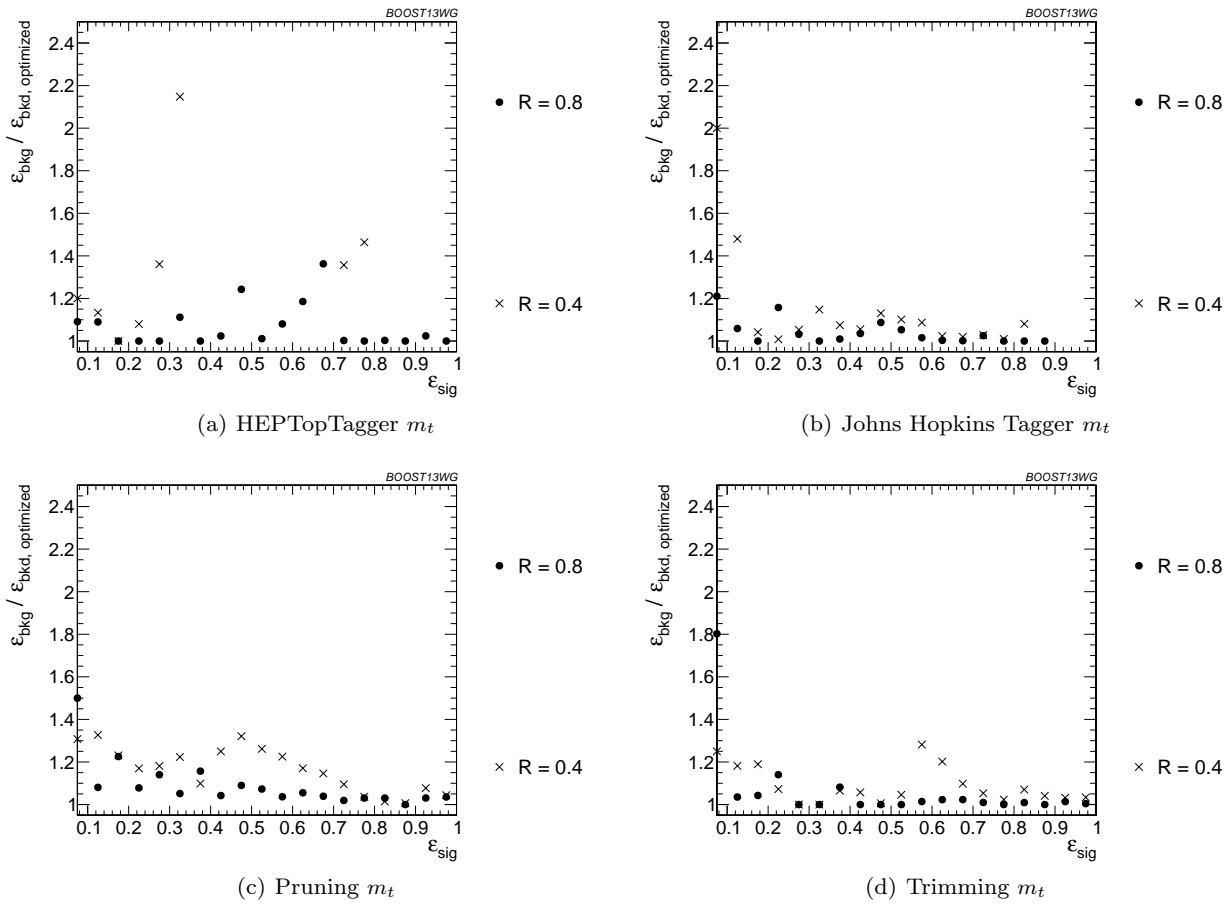


Fig. 48 Comparison of top mass performance of different taggers at different R in the $p_T = 1500 - 1600$ GeV bin; the tagger inputs are set to the optimum value for $R = 1.2$.

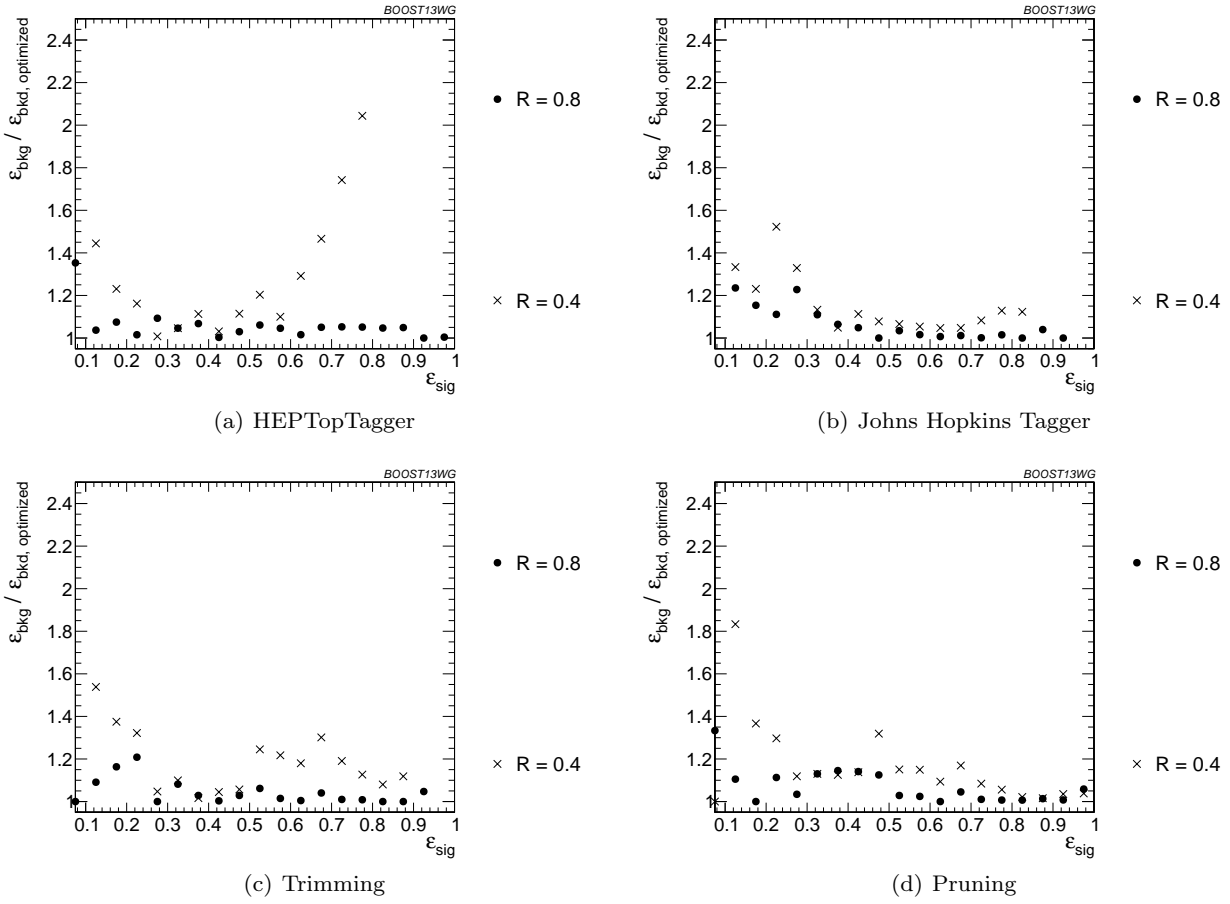


Fig. 49 Comparison of BDT combination of tagger performance at different radius at $p_T = 1.5-1.6$ TeV; the tagger inputs are set to the optimum value for $R = 1.2$.

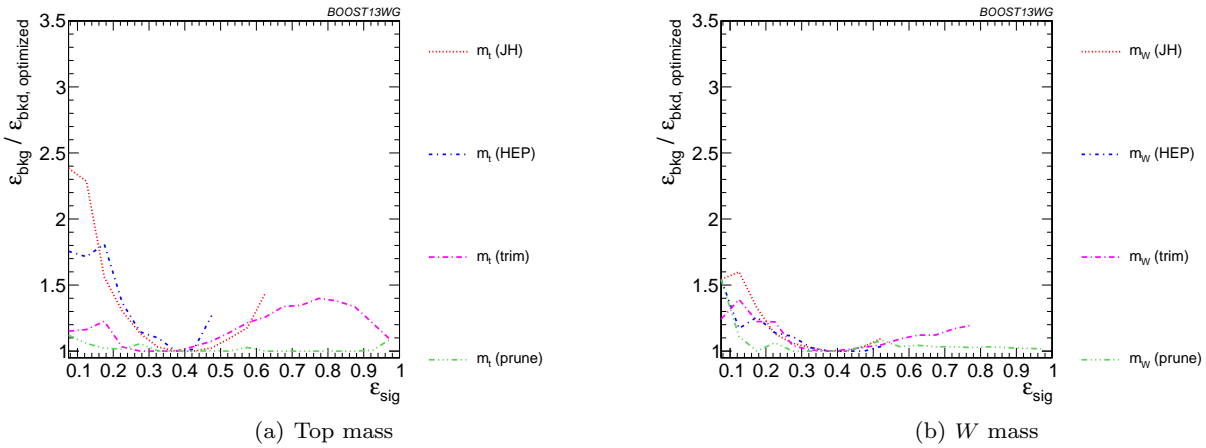


Fig. 50 Comparison of single-variable top-tagging performance in the $p_T = 1-1.1$ GeV bin using the anti- k_T , $R=0.8$ algorithm; the inputs for each tagger are optimized for the $\epsilon_{sig} = 0.3 - 0.35$ bin.

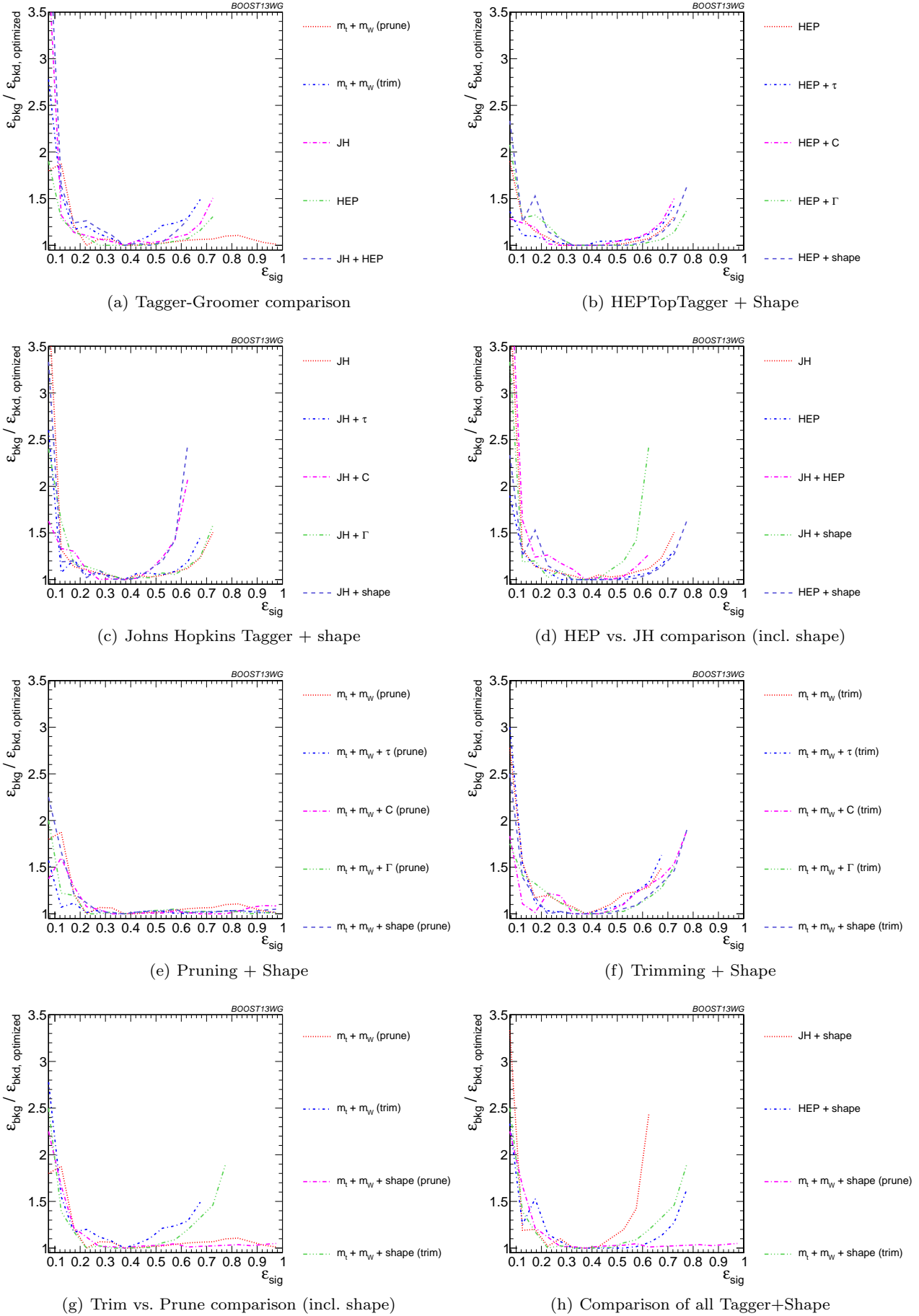


Fig. 51 The BDT combinations in the $p_T = 1 - 1.1$ TeV bin using the anti- k_T $R=0.8$ algorithm. Taggers are combined with the following shape observables: $\tau_{21}^{(\beta=1)} + \tau_{32}^{(\beta=1)}$, $C_2^{(\beta=1)} + C_3^{(\beta=1)}$, Γ_{Qjet} , and all of the above (denoted “shape”). The inputs for each tagger are optimized for the $\epsilon_{\text{sig}} = 0.3 - 0.35$ bin.

1196 8 Summary & Conclusions

1197 This report discussed the correlations between observ-
 1198 ables and looked forward to jet substructure at Run II
 1199 of the LHC at 14 TeV center-of-mass collisions ener-
 1200 gies.

1214 References

- 1215 1. A. Abdesselam, E. B. Kuutmann, U. Bitenc,
 1216 G. Brooijmans, J. Butterworth, et al., *Boosted objects: A*
 1217 *Probe of beyond the Standard Model physics*, *Eur.Phys.J.*
 1218 **C71** (2011) 1661, [[arXiv:1012.5412](#)].
- 1219 2. A. Altheimer, S. Arora, L. Asquith, G. Brooijmans,
 1220 J. Butterworth, et al., *Jet Substructure at the Tevatron and*
 1221 *LHC: New results, new tools, new benchmarks*, *J.Phys.* **G39**
 1222 (2012) 063001, [[arXiv:1201.0008](#)].
- 1223 3. A. Altheimer, A. Arce, L. Asquith, J. Backus Mayes,
 1224 E. Bergeaas Kuutmann, et al., *Boosted objects and jet*
 1225 *substructure at the LHC*, [arXiv:1311.2708](#).
- 1226 4. A. Hoecker, P. Speckmayer, J. Stelzer, J. Therhaag,
 1227 E. von Toerne, and H. Voss, *TMVA: Toolkit for*
 1228 *Multivariate Data Analysis*, *PoS ACAT* (2007) 040,
 1229 [[physics/0703039](#)].
- 1230 5. C. Anders, C. Bernaciak, G. Kasieczka, T. Plehn, and
 1231 T. Schell, *Benchmarking an Even Better HEPTopTagger*,
 1232 *Phys.Rev.* **D89** (2014) 074047, [[arXiv:1312.1504](#)].

1201 Acknowledgements

1202 We thank the Department of Physics at the University
 1203 of Arizona and for hosting the conference at the Little
 1204 America Hotel. We also thank Harvard University for
 1205 hosting the event samples used in this report. This work
 1206 was made possible in part by the facilities of the Shared
 1207 Hierarchical Academic Research Computing Network
 1208 (SHARCNET) and Compute/Calcul Canada. We also
 1209 thank Hallie Bolonkin for the BOOST2013 poster de-
 1210 sign and Jackson Boelts' ART465 class (fall 2012) at
 1211 the University of Arizona School of Arts VisCom pro-
 1212 gram. (NEED TO ASK PETER LOCH FOR MORE
 1213 ACKNOWLEDGEMENTS)